UNIVERSITY OF SOUTHAMPTON

INSTITUTE OF SOUND AND VIBRATION RESEARCH

DYNAMICS GROUP

Design of an adaptive vibration absorbers using shape memory alloy

by

E. Rustighi, M. J. Brennan and B. R. Mace

ISVR Technical Memorandum No. 920

September 2003

Authorized for issue by
Prof. M. J. Brennan
Group Chairman

Abstract

A well-established vibration control device is the tuned vibration absorber (TVA). Even though such a device may be have different shapes it acts like a spring-mass system. For simplicity, in this project a beam-like TVA is used.

One of the drawbacks of such a device, however, is that it can detune during operation because of changes in forcing frequency. To maintain its tuned condition a variable stiffness element is required so that the natural frequency of the absorber can be adjusted in real-time.

In this project a beam-like TVA has been realized using shape memory alloy (SMA). Such a material changes its mechanical properties with temperature. By varying the temperature of the beam the absorber can be tuned in order to maintain the vibration of the host structure to be very small.

During the project some design, modelling and experimental work has been carried out. This work has resulted in one prototype device that have been built and tested. First results of a SMA-TVA are presented. Moreover, a control technique has been designed and some simulated tests have been carried out.

Contents

Nomenclature

a	Attenuation
A	Cross section
A_e	Surface of heat exchange
A_s, A_f	Austenite start and finish temperature of transformation
C_A, C_M	Stress coefficients of transformation hysteresis
c_p	Specific heat
d	Diameter of the wire
D	Elastic matrix and derivative constant of control algorithm
d_n	Derivative of the error at n-th time step
E	Young modulus
e_n	Control error at n-th time step
F_0	Amplitude of the exciting force
F_n	Modal forces
H	Estimate of the FRF
I	Geometric moment of inertia of the cross section and intensity of current
IAE	Absolute value of the error
I_n	Current at n-th time step
i_n	Integral of the error at n-th time step
k_1	Stiffness of the base structure
k_2	Stiffness of the dynamic absorber
K_n	Modal stiffness
k_n	Stiffness at n-th time step
L	Length of the beam
m_1	Mass of the machine (host structure)
m_2	Mass of the dynamic absorber
M_n	Modal masses
M_s, M_f	Martensite start and finish temperature of transformation
m_{tot}	Total mass of the beam
P	Proportional constant of control algorithm
Q	Heat flow
q	Distributed load

R	Electrical resistance
${}_rA_{jk}$, ${}_rD_{jk}$	Modal constant
S	Autospectrum and cross spectrum
t	Time
$T_n(t)$, $z_n(t)$	Modal coordinates
U	Internal energy
u	Motion of the beam
V	Velocity amplitude and volume
X_1	Amplitude of the displacement response of the machine
X_2	Amplitude of the displacement response of the dynamic absorber
Y_R	Modulus of rupture
Y_S	Yield stress
z	Displacement of a beam perpendicular to his axis
z_1	Point impedance of the machine
z_2	Point impedance of the dynamic absorber
$Z_n(z)$	Mode shapes or stationary waves
ΔH	Latent heat of transformation
Θ	Thermo-elastic tensor
Ω	Transformation tensor
α	Convective coefficient
$\alpha(\omega)$	Receptance
β	Current constant
χ, ν	Constants defined in the report
ϕ	Angle between the responses of the machine and of the absorber
ϕ_n	Mass-normalized mode shapes
ϕ_n	Mass normalized mode shapes
η	Loss factor
μ	Mean value
θ	Temperature
θ_a	Ambient temperature
ρ	Density
ρ_e	Electrical resistivity

σ	Stress
τ	Time constant
ω	Frequency of the excitation and of the response
ω_a	Anti-resonance frequency
ω_n	Natural frequencies
ω_r	Resonance frequency
ξ	Martensitic fraction

1. Introduction

A well-established vibration control device is the tuned vibration absorber (TVA), which can be used to suppress a troublesome resonance or to attenuate the vibration of a structure at a particular forcing frequency. Even though such a device may have different forms, it basically acts like a spring-mass system.

One of the drawbacks of such a device, however, is that it can detune during operation because of changes in forcing frequency or the stiffness of the device could change. To maintain its tuned condition a variable stiffness element is required so that the natural frequency of the absorber can be adjusted in real-time [1]. This can be achieved in a number of ways for example by altering the pressure in a set of rubber bellows [2], altering the gap between two beams forming a compound cantilever beam [3], adjusting the number of active coils in a coil spring [4] or changing the temperature of a viscoelastic element [5].

The main advantage of an actively tuned device is that low damping can be used if the tuning is precise and this reduces the need for a large mass [1]. In order to automatically tune the vibration absorber, a control strategy can be used, such as that proposed by Long et al [2] or Kidner and Brennan [6-8].

Semi active control operates by generating a secondary force passively, by actively altering the characteristics of the system, so the passive system is most effective. Semi active devices can attain high reductions in the level of vibration and only require modest amounts of power for the sensors and the controller. By not putting energy into the system (apart from small amounts to tune the system), semi active devices are generally less expensive and inherently more stable than their fully active counterparts. Vibration control systems illustrated in the literature have been tuned using feedforward and feedback controls or various adaptive strategies.

This report is concerned with the design and realization of a beam-like TVA that has been manifactured using shape memory alloy (SMA). Such a material changes its mechanical properties (the Young modulus in particular) with temperature. By varying the temperature of the beam the absorber can be tuned to minimise the vibration of the structure to which is attached [9]. In addition, SMAs are inherently simple, compact, and they could be safely used in spark-free and zero gravity conditions. Their characteristics also contribute to a clean and silent working condition.

The main limitations of SMAs are the slow response time (bandwidth is limited due to heating and cooling restrictions and can only achieve a few Hz at the very best) and the poor energy conversion efficiency when actuated with an electrical signal [9-11].

A brass TVA and a SMA TVA have been built and experimentally characterised. The results show the feasibility of using SMA properties to tune such a device. At the same time the numerical analysis shows the effectiveness and robustness of a simple non linear adaptive system that considers only the phase between two signals measured from the TVA.

As it is planned to implement an automatic adaptive control system a numerical analysis is carried out in parallel with the experimental one. The aim is to make a brief comparison of adaptive systems possible for tuning the stiffness of a dynamic vibration absorber and then to discuss in detail a control system for the SMA TVA.

After the introduction, chapter two describes the TVA characteristics and chapter three introduces SMA. Then chapter four contains the design guidelines of the experimental test rigs. Chapter five shows the experimental results obtained with the SMA TVA. Moreover, chapter six deals with the numerical test and the adaptive control design, first for TVA and then for SMA TVA. Eventually, the conclusion summarises the work carried out.

2. Tunable vibration absorber (TVA)

2.1. Introduction

This section outlines the principle of a TVA and describes a particular configuration in which it could be designed. The first part of the section deals with the theoretical modelling of a TVA and shows the main equations necessary to describe its behaviour. The second part of the section introduces the guidelines to design a beam as a TVA. A 2dof model is introduced to simplify the complex continuous model of the beam.

2.2. Classical and advanced theory

A machine may experience excessive vibrations when excited by a force whose excitation frequency nearly coincides with a natural frequency of the machine. In order to reduce the vibration level a vibration absorber may be used. This is simply an additional spring-mass-damper system that is added to the machine so that the natural frequencies of the resulting system are away from the excitation frequency and, ideally, there is an antiresonance at the excitation frequency.

This absorber is actually designed in two distinct ways: the first is when it is tuned to a problematic resonance of the host structure and the other is where it is tuned to a troublesome excitation frequency. In the first case the purpose of the absorber is to add damping to reduce the motion of the structure at frequencies close to the resonance frequency (broadband effectiveness). In the second case its purpose is to add a large mechanical impedance to the host structure at a single frequency of excitation with the aim of minimizing the motion of the structure at this frequency (discrete frequency effectiveness) [1]. It is the second case that is the subject of this work, and the device is usually called a tuned vibration neutralizer (TVN) or a tuned vibration absorber (TVA).

The analysis of a vibration neutralizer is considered by idealizing the machine to which it is attached as a single degree of freedom system as shown in Figure 1. When a harmonic force $F_0 e^{i\omega t}$ acts on the machine the amplitudes X_1 and X_2 of the masses are given by

$$\begin{aligned} \left(-m_1\omega^2 + k_1 + k_2\right)X_1 - k_2 X_2 &= F_0 \\ -k_2 X_1 + \left(-m_2\omega^2 + k_2\right)X_2 &= 0 \end{aligned} \qquad (1a,b)$$

A list of symbols can be found on page iii.

Rearranging equations 1a and 1b gives the steady state displacement amplitudes of the two masses m_1 and m_2:

$$X_1 = \frac{F_0\left(k_2 - m_2\omega^2\right)}{\left(-m_1\omega^2 + k_1 + k_2\right)\left(-m_2\omega^2 + k_2\right) - {k_2}^2}$$
$$X_2 = \frac{F_0 k_2}{\left(-m_1\omega^2 + k_1 + k_2\right)\left(-m_2\omega^2 + k_2\right) - {k_2}^2} \qquad (2a,b)$$

It is clear from equation 2a that in order to reduce the vibration of the machine the natural frequency of the neutralizer must be the same as the excitation frequency, i.e.

$$\frac{k_2}{m_2} = \omega^2 \qquad (3)$$

Equations 2a and 2b can be simplified by assuming the machine vibrates like a simple mass (i.e. $k_1 = 0$). Such simplification is reasonable because often m_1 is on soft springs for vibration isolation and the excitation frequency is much greater than the machine resonance frequency. Moreover, if we now consider the structural damping of the neutralizer, so that $k_2 \equiv k_2(1 + i\eta)$, we obtain

$$X_1 = \frac{k_2 - m_2\omega^2 + ik_2\eta}{m_1 m_2\omega^4 - (m_1 + m_2)k_2\omega^2 - i(m_1 + m_2)k_2\omega^2\eta} F_0$$
$$X_2 = \frac{-k_2 - ik_2\eta}{m_1 m_2\omega^4 - (m_1 + m_2)k_a\omega^2 - i(m_1 + m_2)k_2\omega^2\eta} F_0 \qquad (4a,b)$$

The amplitudes are given by

$$\left|\frac{X_1}{F_0}\right| = \sqrt{\frac{{m_2}^2\omega^4 - 2m_2k_2\omega^2 + {}^2\,{k_2}^2\left(1+\eta^2\right)}{{m_1}^2{m_2}^2\omega^8 - 2m_1m_2(m_1+m_2)k_2\omega^6 + (m_1+m_2)^2{k_2}^2\left(1+\eta^2\right)}}$$
$$\left|\frac{X_2}{F_0}\right| = \sqrt{\frac{{k_2}^2\left(1+\eta^2\right)}{{m_1}^2{m_2}^2\omega^8 - 2m_1m_2(m_1+m_2)k_2\omega^6 + (m_1+m_2)^2{k_2}^2\left(1+\eta^2\right)}}$$

and the phases are

$$\angle X_1 = \arctan\left(\frac{k_2\eta}{k_2 - m_2\omega^2}\right) - \arctan\left(\frac{-(m_1+m_2)k_2\omega^2\eta}{m_1m_2\omega^4 - (m_1+m_2)k_2\omega^2}\right)$$
$$\angle X_2 = \arctan(\eta) - \arctan\left(\frac{-(m_1+m_2)k_2\omega^2\eta}{m_1m_2\omega^4 - (m_1+m_2)k_2\omega^2}\right)$$

If we consider the difference of phases we obtain

$$\phi = \angle X_1 - \angle X_2 = \arctan\left(\frac{k_2\eta}{k_2 - m_2\omega^2}\right) - \arctan(\eta)$$

Noting that

$$\tan(\alpha-\beta)=\frac{\tan(\alpha)-\tan(\beta)}{1+\tan(\alpha)\tan(\beta)}$$

it follows that

$$\tan(\phi)=\frac{m_2\omega^2\eta}{k_2(1+\eta^2)-m_2\omega^2}$$

The difference of phase ϕ is also physically comprised between 180° and 360°, as can be inferred from equations 4a and 4b, and therefore

$$\cos(\phi)=-\sqrt{\frac{1}{1+\tan^2(\phi)}}\,\mathrm{Sign}[\tan(\phi)]=\pm\sqrt{\frac{1}{1+\left(\frac{m_2\omega^2\eta}{k_2(1+\eta^2)-m_2\omega^2}\right)^2}} \tag{5}$$

This equation is useful because the goal is to tune the TVA so that $\omega=\sqrt{k_2/m_2}$ (equation 3) and the tuning strategy is to use the cosine of the phase difference between the measured responses X_1 and X_2 as an error signal. In order to tune the neutralizer to the excitation we plan to change its stiffness so that $\cos(\phi)=0$. Figures 2-5 show various relations between stiffness, $\cos(\phi)$ and the excitation frequency.

It is convenient to write down the governing equations of motion of the machine and the neutralizer in the frequency domain in terms of their mechanical impedances (see [12]), which are given by [13]

$$z_1=j\omega m_1$$

$$z_2=\frac{-j}{\frac{\omega}{k_2}-\frac{1}{\omega m_2}}$$

Figure 6 depicts an impedance diagram of the system.

Given that the two sub-systems are in parallel, the impedance of the resulting system is

$$z=z_1+z_2=\frac{j\omega\left[m_1m_2\omega^2-k_2(m_1+m_2)\right]}{m_2\omega^2-k_2} \tag{6}$$

Figure 7 shows the impedance as a function of frequency. Referring to the total system, there is a resonance, ω_r, when the numerator is zero (the impedance is zero, that is a null force could move the system) and there is an anti-resonance, ω_a, when the denominator is zero (the impedance tends to infinity that is only an infinite force could move the system). These frequencies are such that

$$\omega_a = \sqrt{\frac{k_2}{m_2}}$$
$$\omega_r = \sqrt{\frac{k_2(m_1 + m_2)}{m_1 m_2}} \qquad (7a,b)$$

The anti-resonance frequency of the system, ω_a, coincides with the resonance of the TVA, in fact the machine doesn't move and behave as if it were grounded.

Note that the anti-resonance coincides with the resonance of the neutralizer (in accordance with equation 3) because the mass of the machine is constrained to have zero motion.

Brennan [1] showed that that the displacement of the machine can only be reduced significantly if the impedance of the neutralizer is much greater than that of the machine. The effectiveness of the neutralizer may be judged by the amount that it attenuates the displacement of the machine to which is attached, so we define the attenuation as the ratio of the free motion of the machine to the motion of the machine with the neutralizer fitted. Assuming that the impedance of the neutralizer is much greater than the impedance of the machine (neutralizer properly tuned), the attenuation has the following form

$$a\big|_{z_2 >> z_1} \cong \frac{z_1}{z_2} \qquad (8)$$

If the neutralizer is tuned to the excitation frequency and assuming that $\eta << 1$ then the impedance of the vibration neutralizer is approximately given by

$$z_2\big|_{\substack{\omega=\omega_a \\ \eta<<1}} \cong \frac{\omega_a m_2}{\eta} \qquad (9)$$

and the attenuation by

$$\frac{z_1}{z_2}\bigg|_{\substack{\omega=\omega_a \\ \eta<<1}} \cong \frac{\omega_a m_1}{\frac{\omega_a m_2}{\eta}} = \frac{m_1 \eta}{m_2} \qquad (10)$$

Equation 9 shows that the impedance of the neutralizer

1. increases with frequency;
2. increases with the mass;
3. decreases with damping.

So in order to maximize the attenuation (see equation 10), the impedance of the neutralizer must be large i.e. the neutralizer should have a small loss factor and a large mass.

The half power bandwidth over which the vibration of the machine is reduced is proportional to damping in the neutralizer and is independent of the mass ratio, so the only way of achieving a large attenuation without sacrificing bandwidth is to increase the mass ratio.

2.3. The free-free beam as a TVA

A very simple neutralizer can be obtained by attaching a beam to the host structure in its centre. For frequencies around the first natural frequency of the beam, it behaves essentially as a sdof system. Using such a configuration it is possible to use shape memory alloy wires in a straightforward way.

First the lateral vibration behaviour of a free-free beam is considered. The equation of motion of the beam is

$$\rho A \frac{\partial^2 u(z,t)}{\partial t^2} = -EI \frac{\partial^4 u(z,t)}{\partial z^2} \tag{11}$$

where ρ and A are the density and the cross section of the beam and u is the lateral displacement of the beam and is a function of the time t and of the axial coordinate z. E and I are the Young modulus and the second moment of area of the cross section.

The solution of the equation can be found using the method of separation of variables writing

$$u(z,t) = Z(z)T(t)$$

equation 11 can now be written as

$$\frac{\ddot{T}}{T} = -\nu^2 \frac{Z^{IIII}}{Z}$$

where

$$\nu = \sqrt{\frac{EI}{\rho A}}$$

$(\cdot)^{IIII}$ is the fourth derivative with respect to the axial coordinate z.

The left hand side depends only on time t and the right hand side only on the displacement z so the two sides must be both equal to the same constant. Thus we obtain the following equations

$$\ddot{T} + \omega^2 T = 0$$
$$\nu^2 Z^{IIII} - \omega^2 Z = 0$$

The solutions of the two differential equations are

$$T = A\cos\omega t + B\sin\omega t$$
$$Z = C\cos\chi z + D\sin\chi z + E\cosh\chi z + F\sinh\chi z$$

where

$$\chi = \sqrt{\frac{\omega}{\nu}}$$

Considering the boundary conditions for a free-free beam we have

$$Z^{II}(0) = Z^{III}(0) = Z^{II}(L) = Z^{III}(L)$$

where $(\cdot)^{II}$ and $(\cdot)^{III}$ are the second and third derivative with respect to the axial coordinate *z*.

Applying these boundary condition leads to the following equation:

$$C = E$$
$$D = F$$
$$C(\cos\chi L - \cosh\chi L) + D(\sin\chi L - \sinh\chi L) = 0$$
$$-C(\sin\chi L + \sinh\chi L) + D(\cos\chi L - \cosh\chi L) = 0$$

In order for these to be a non-trivial solution we obtain

$$\cos\chi L \cdot \cosh\chi L = 1$$

Several solutions of this equation for χ, are given in Table 1. Note that also $\chi=0$ is a solution, and represents the rigid motion of the undeformed beam. Actually there are two solutions for $\chi=0$ that represent the translational and rotational motion. As in this work we are dealing with a beam supported in the centre, the rotational rigid body motion is neglected.

The natural frequencies of the system are given by

$$\omega_n = \nu\chi_n^2$$

and expressing the constant *D* in terms of *C* gives

$$D_n = C_n \frac{\sin\chi_n L + \sinh\chi_n L}{\cos\chi_n L - \cosh\chi_n L}$$

The solution for the displacement can therefore be written as

$$Z_n = C_n\left(\cos\chi_n z + \frac{D_n}{C_n}\sin\chi_n z + \cosh\chi_n z + \frac{D_n}{C_n}\sinh\chi_n z\right)$$

The correct value of the constant *C* is found from boundary conditions.

The free vibration mode shapes of distributed parameter systems satisfy the orthogonality condition in a manner analogous to discrete systems. The mass orthogonality condition for continuous systems can be expressed by

$$\int_0^L \rho A Z_i Z_j \mathrm{d}z = 0 \qquad \forall i \neq j$$

In the same manner we could express the stiffness orthogonality condition as

$$\int_0^L EI \frac{\mathrm{d}^2 Z_i}{\mathrm{d}z^2} \frac{\mathrm{d}^2 Z_j}{\mathrm{d}z^2} \mathrm{d}z = 0 \qquad \forall i \neq j$$

Using the orthogonality properties of mode shapes, it is possible to develop a modal superposition procedure for distributed parameter systems. As is the case for discrete systems, the displacement solution is expressed in terms of a linear combination of mode shapes as:

$$u(z,t) = \sum_{i=0}^{\infty} Z_i(z) \cdot T_i(t) = \sum_{i=0}^{\infty} Z_i(z) \cdot z_i(t) \tag{12}$$

Substituting this in to equation 11, to which the distributed force q has been added, multiplying both sides by the mode shape Z_j, integrating and applying the orthogonality properties we get the following system of uncoupled modal equations:

$$\int_0^L \left(\rho A Z_n^2 \frac{\partial^2 z_n}{\partial t^2} + EIZ_n \frac{\mathrm{d}^4 Z_n}{\mathrm{d}z^4} z_n \right) \mathrm{d}z = \int_0^L Z_n q(z,t) \mathrm{d}z \qquad n = 0, \ldots, \infty$$

These equations can be written in a simpler form by introducing the following definitions:

Modal mass: $$M_n = \int_0^L \rho A Z_n^2 \mathrm{d}z$$

Modal stiffness: $$K_n = \int_0^L EIZ_n \frac{\mathrm{d}^4 Z_n}{\mathrm{d}z^4} \mathrm{d}z \equiv \int_0^L EI \left(\frac{\mathrm{d}^2 Z_n}{\mathrm{d}z^2} \right)^2 \mathrm{d}z$$

Modal force: $$F_n(t) = \int_0^L Z_n q(z,t) \mathrm{d}z$$

The equation for the *n-th* mode thus becomes

$$M_n \ddot{z}_z + K_n z_z = F_n$$

This is the same expression that is obtained with the Rayleigh method applied for continuous systems. Solutions of each modal equation can be now obtained straightforwardly.

The mass-normalized mode shapes are defined by

$$\phi_n = \frac{Z_n(z)}{\sqrt{M_n}}$$

The receptance can be written in terms of the modal properties as

$$[\alpha(\omega)] = [\phi][(\omega_n^2 - \omega^2)]^{-1}[\phi]^T$$

or in the explicit formulation

$$\alpha(\omega)_{j,k} = \frac{X_j}{F_k} = \sum_{n=0}^{N} \frac{\phi_n(z_j)\phi_n(z_k)}{\omega_n^2 - \omega^2} = \sum_{n=0}^{N} \frac{Z_n(z_j)Z_n(z_k)}{(\omega_n^2 - \omega^2)M_n}.$$

Thus the point mobility (see [12]) at the centre (z=L/2) of a free-free beam is given by [6]

$$\frac{V_{L/2}}{F_{L/2}} = i\omega\alpha(\omega)_{L/2,L/2} = \frac{1}{i\omega m_{tot}} + \sum_{n=1}^{\infty} \frac{i\omega\phi_n^2(L/2)}{(\omega_n^2 - \omega^2)}$$

in which the first term is the mobility of the translational rigid motion. The rotational rigid motion is missing because of the symmetry around the excitation point.

Considering only the first mode of vibration besides the rigid body motion

$$\frac{V_{L/2}}{F_{L/2}} \approx \frac{1}{i\omega m_{tot}} + \frac{i\omega\phi_1^2(L/2)}{(\omega_1^2 - \omega^2)} \tag{13}$$

The resonance is clearly at ω=ω_1 and the anti-resonance is at

$$\omega_a = \frac{\omega_1^2}{1 + m_{tot}\phi_1^2(L/2)} \tag{14}$$

A two dof system (equation 7) consisting of two masses connected by a spring that fits this simplified model (equation 12) should have the following mass ratio [6]

$$\frac{m_2}{m_1} = m_{tot}\phi_1^2(L/2) = 1.478$$

In summary, in order to approximate the behaviour of a free-free beam supported in the middle in a frequency range up to the first natural frequency or so, we can use a simplified two dof system with the following characteristics

$$\begin{aligned} m_1 &= \frac{m_{tot}}{2.478} = 0.404 \cdot m_{tot} \\ m_2 &= 0.596 \cdot m_{tot} \\ k &= \frac{0.596}{2.478} \cdot \omega_1^2 m_{tot} \end{aligned} \tag{15a,b,c}$$

2.4. Summary

The idea of using a TVA for the control of vibration has been described. The way in which such a device works has been described. The guidelines to design a beam as a

TVA have been outlined and the way in which such a system can be studied as a 2dof system has been described.

Figures

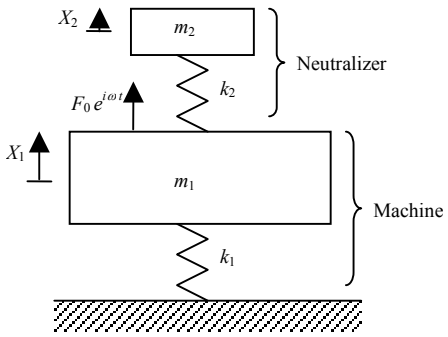

Figure 1 Undamped vibration neutralizer fitted to an undamped single degree-of-freedom system (Machine)

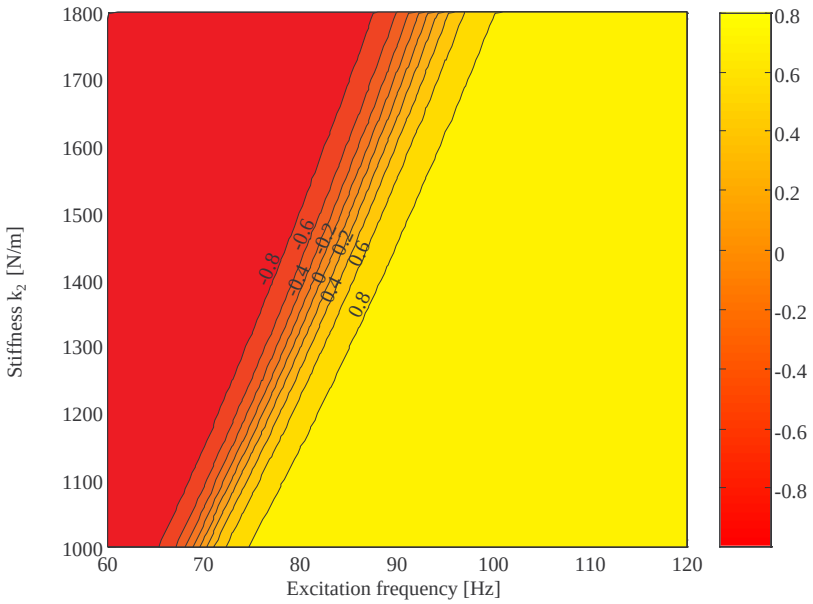

Figure 2 Variation of the cosine of the phase difference vs. excitation frequency and stiffness (m_1=0.0036 kg; m_2=0.0053 kg; η=0.1)

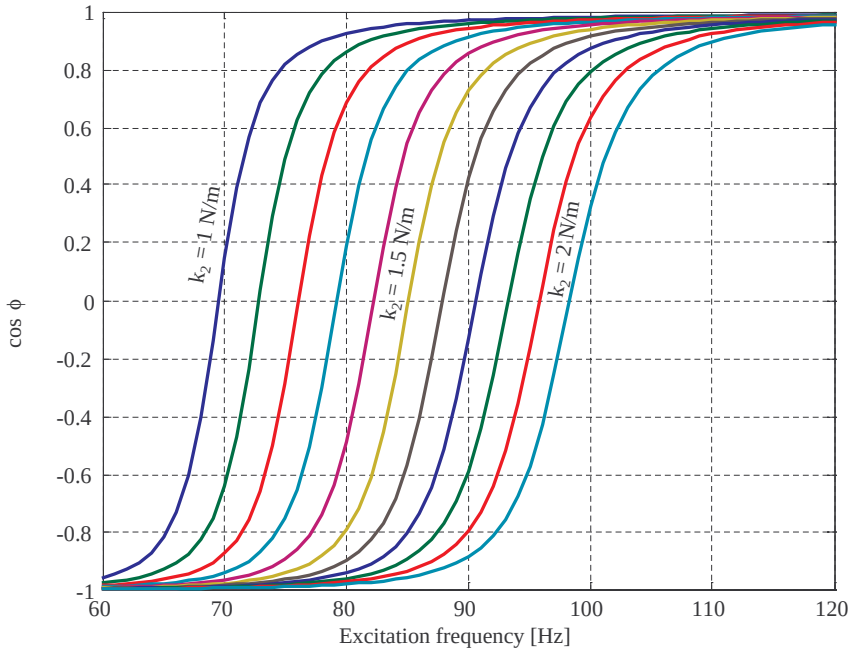

Figure 3 The cosine of the phase difference vs. excitation frequency at different stiffness values (m_1=0.0036 kg; m_2=0.0053 kg; η=0.1)

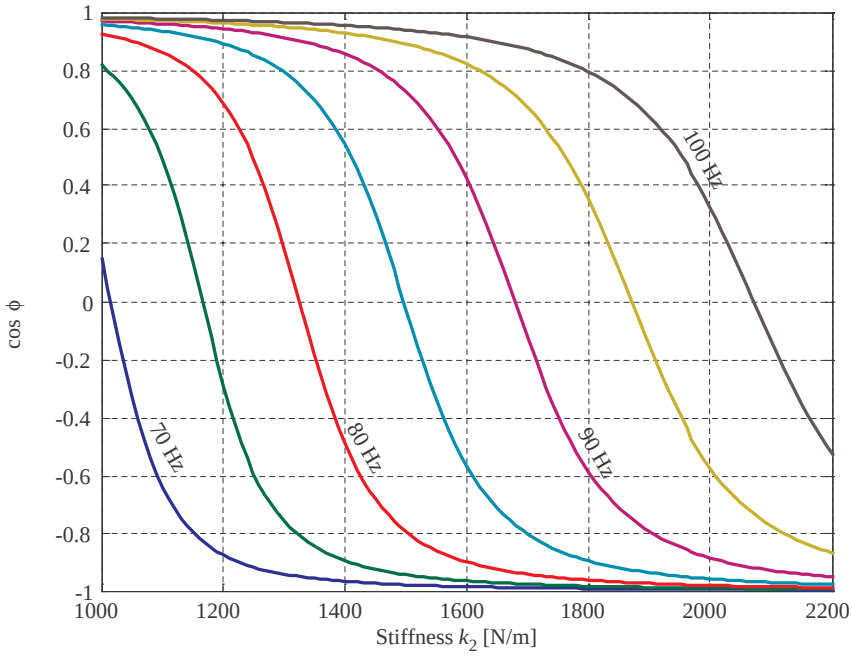

Figure 4 The cosine of the phase difference vs. neutralizer stiffness at different excitation frequencies (m_1=0.0036 kg; m_2=0.0053 kg; η=0.1)

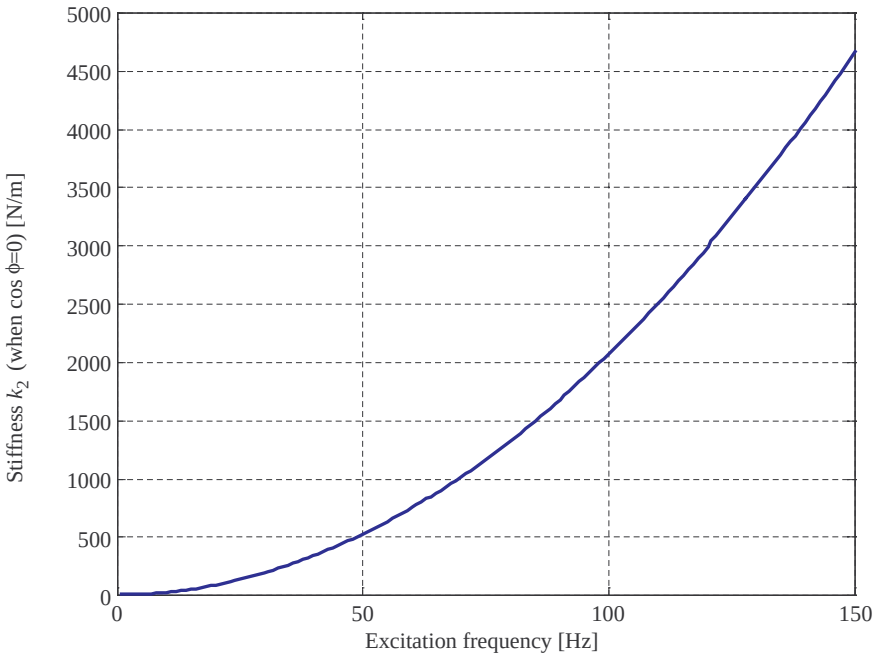

Figure 5 The tuned value of the neutralizer stiffness vs. the excitation frequency (m_1=0.0036 kg; m_2=0.0053 kg; η=0.1)

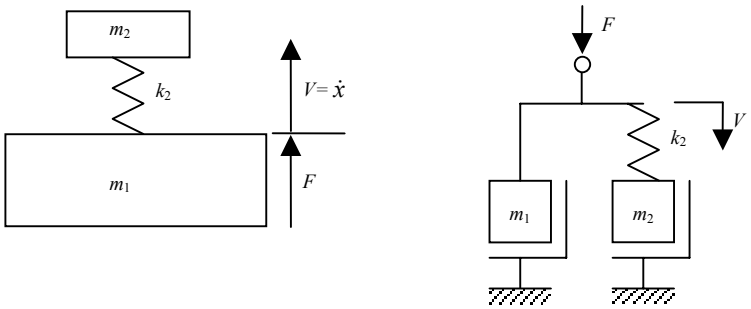

Figure 6 Impedance schematization of the vibration neutralizer.

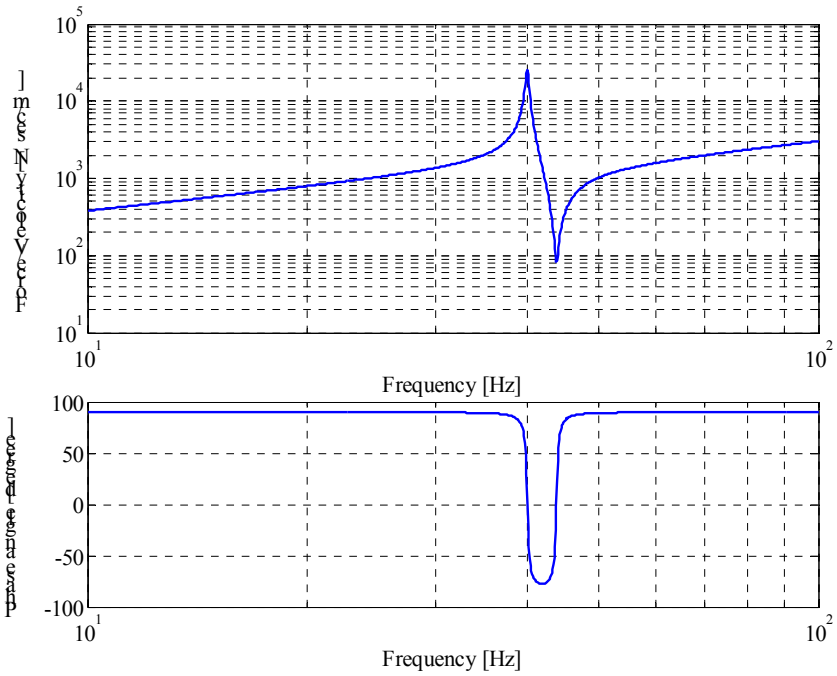

Figure 7 Impedance of a system comprising a mass and a neutralizer (m_1=5 kg; m_2=1 kg; k_2=63165 N/m; η=0.01)

Tables

n	1	2	3	4	5
$\chi_n L$	4.730	7.853	10.996	14.137	$\approx\left(n+\frac{1}{2}\right)\pi$

Table 1 Values of $\chi_n L$ for the free flexural vibrations of a free-free beam

3. Shape Memory Alloys

3.1. Introduction

This section introduces the properties of SMA. The mathematical models used to describe such properties are discussed in order to present the tools to design a mechanical structure involving their use. Since the TVA, described in this report, involves the temperature control of SMA wire, a thermal model of such a system is developed. An electrical current will be used to input heat in the material and change the temperature of the wire so as to change its mechanical properties. A short review of the application of SMA as a smart material in controlled systems is also presented.

Shape memory alloys are metals that have the property by which they can remember their original size and shape and revert to it at a characteristic transformation temperature. Generally, they can be plastically deformed at some relatively low temperature, and upon exposure to some higher temperature will return to their shape prior to the deformation. Materials that exhibit shape memory only upon heating are referred to as having a one way shape memory. Some materials also undergo a change in shape upon re-cooling, showing a so-called two way shape memory effect. The shape memory effect can be a one way or two way effect depending on the type of the material training[1].

Although a relatively wide variety of alloys exhibit the shape memory effect, only those that can recover substantial amounts of strain or that generate significant force upon changing shape are of commercial interest. In such materials, heating and cooling could produce large mechanical deformation (thermomechanical strain is in the range of 5-10%). To date, this has been the nickel-titanium alloys and copper-base alloys such as CuZnAl and CuAlNi.

The first recorded observation of the shape memory transformation was by Chang and Read in 1932. They noted the reversibility of the transformation in AuCd by metallographic observations and resistivity changes. However, it was not until 1960, when Buehler and co-workers at the Naval Ordnance Laboratory discovered the effect

[1] MATERIAL TRAINING: Two-way shape memory behaviour is accomplished by introducing internal stresses in the material during the martensitic phase: this can be accomplished by deforming the specimen in the austenitic phase and cooling the material while maintaining this state of stress. This process introduces internal stresses in the material that will cause a two way shape memory effect.

in equiatomic nickel-titanium (NiTi), that research into both the metallurgy and potential practical uses began in earnest. They named it NiTiNOL to include the acronym of the name of their laboratory. Study of shape memory alloys has continued at an increasing pace since then, and more products using these materials are coming to the market each year. For instance because of their biocompability and superior resistance to corrosion, shape memory alloys have gained wide usage in the medical field as bone plate, artificial joints, orthodontic devices, coronary angioplasty probes, arthroscopic instrumentation, etc. [10, 14, 15]

Following this introduction, the next section outlines the properties of the SMA and deals with the thermo-mechanical models that can be used to describe the behaviour of the material. Besides a complex tri-dimensional constitutive model, a simplified model appropriate for SMA wires, is described. The third subsection describes the thermal behaviour of a SMA wire, as the main objective of this report is to control the temperature of a SMA wire acting as a TVA. The fourth subsection outlines the properties of the SMA wire used to build the TVA described in this report. The SMA properties given by the company and those observed in the experiments are compared. The fifth subsection summarizes some applications of SMA in control devices and a summary subsection ends the section.

3.2. Phase transformation: shape memory effect and superelasticity

3.2.1. Crystallography of martensite and austenite

The shape memory effect is related to the molecular structure of the material, i.e. SMA materials undergo a phase transformation when heated or cooled. The phase change is between two solid phases and involves rearrangement of atoms within the crystal lattice. The internal structure is different at different temperatures. The low temperature phase is known as martensite, with highly twinned crystalline structure, and the high temperature phase is called austenite, with a body-centered cubic structure (see Figure 9).

Martensite, the low temperature phase, is relatively soft whereas austenite, the high temperature phase, is relatively hard. In order to understand this phenomenon, it is useful to consider the highly simplified two-dimensional representation of the material's crystalline arrangement shown in Figure 9. Each box represents a grain of

material with its corresponding grain boundaries. The martensite grains form a heavily twinned structure, meaning they are oriented symmetrically across grain boundaries. The twinned structure allows the internal lattice of individual grains to change while still maintaining the same interface with adjacent grains. As a result, SMA can experience large macroscopic deformations while maintaining remarkable order within its microscopic structure.

3.2.2. Hysteresis loop – model of transformation

The difference between the transition temperatures upon heating and cooling is called hysteresis. Hysteresis is generally defined as the difference between the temperatures at which the material is 50 % transformed to austenite upon heating and 50 % transformed to martensite upon cooling. This difference can be up to 20-30 °C.

The phase transformation model has five parameters: the fraction of martensite in the material ξ; the temperature at which austenite phase transformation starts and finishes, A_s and A_f; the temperature at which martensite phase transformation starts and finishes, M_s and M_f. Material tests reveal that the relationship between martensitic fraction ξ and temperature θ takes the form shown in Figure 10 [10, 16, 17]. During a full transformation the functions $\xi_{M\to A}(\theta)$, from the martensite to the austenite state, and the function $\xi_{M\leftarrow A}(\theta)$, from the austenite to the martensite state, are similar to a cosine function given by

$$\xi_{M\to A} = \begin{cases} 1 & \theta < A_s \\ \frac{1}{2}\cos\left(\pi \frac{\theta - A_s}{A_f - A_s}\right) + \frac{1}{2} = C_{M\to A} & A_s \le \theta \le A_f \\ 0 & \theta > A_f \end{cases} \tag{16}$$

$$\xi_{M\leftarrow A} = \begin{cases} 1 & \theta < M_f \\ \frac{1}{2}\cos\left(\pi \frac{\theta - M_f}{M_s - M_f}\right) + \frac{1}{2} = C_{M\leftarrow A} & M_f \le \theta \le M_s \\ 0 & \theta > M_s \end{cases} \tag{17}$$

During a partial transformation the function of the martensite $\hat{\xi}_{M\to A}(\theta)$ and $\hat{\xi}_{M\leftarrow A}(\theta)$ are given by

$$\hat{\xi}_{M\to A} = E_{MA}\xi_{M\to A} \tag{18}$$

$$\hat{\xi}_{M\leftarrow A} = \left[(1 - E_{AM})\xi_{M\leftarrow A}\right] + E_{AM} \tag{19}$$

where E_{MA} and E_{AM} are the amplitude of these functions that change depending on the history of the deformation and must be updated when there is a change in the gradient of temperature in accordance with

$$E_{MA} = \begin{cases} \hat{\xi}_{M\leftarrow A} & \theta < A_s \\ \dfrac{\hat{\xi}_{M\leftarrow A}}{C_{M\rightarrow A}} & A_s \le \theta \le A_f \\ \hat{\xi}_{M\leftarrow A} & \theta > A_f \end{cases} \tag{20}$$

$$E_{AM} = \begin{cases} \hat{\xi}_{M\rightarrow A} & \theta < M_f \\ \dfrac{\hat{\xi}_{M\rightarrow A} - C_{M\leftarrow A}}{1 - C_{M\leftarrow A}} & M_f \le \theta \le M_s \\ \hat{\xi}_{M\rightarrow A} & \theta > M_s \end{cases} \tag{21}$$

The transformation temperatures are also functions of stress: these parameters increase with an increase in tensile stress. Thus, phase transformation can occur at constant temperature by applying stress to the SMA. Increasing the stress increases the temperature associated with the phase transformation. So even if the temperature is constant, the fraction of martensite increases due to the increase in the applied stress. Experiments demonstrate that the critical temperatures are a linear function of the applied stress.

Increasing the stress results in a shift towards the martensitic phase and away from the austenitic phase. A simple rule to remember is that **increasing the stress is equivalent to decreasing the temperature**. These effects can be modelled by incorporating an equivalent temperature into the equation

$$\begin{cases} \theta^{eq.}_{M\leftarrow A} = \theta - \dfrac{\sigma}{C_M} \\ \theta^{eq.}_{M\rightarrow A} = \theta - \dfrac{\sigma}{C_A} \end{cases} \tag{22}$$

where C_A=tan(α) and C_M=tan(β) (see Figure 11). Usually $\alpha=\beta$.

3.2.3. Constitutive model of SMA

The stress-strain relations of martensite and austenite are quite different as shown in Figure 12 [14]. Austenite presents a bilinear elastoplastic behaviour. Martensite shows a plateau with deformation at constant stress. This is due to the de-twinning of the twinned structure. Such deformation (martensite residual strain) can be recovered up to 10% by heating the SMA.

The stress state in an SMA component is a function of three primary state variables. They are the fraction of martensite, the temperature at which the component is operating and the strain at which the component is functioning. Therefore

$$\bar{\sigma} = \bar{\sigma}(\bar{\varepsilon}, \theta, \xi) \tag{23}$$

Here $\bar{\sigma}$ is the Piola-Kirchoff stress tensor and $\bar{\varepsilon}$ is the Green strain tensor [10, 16, 18] because SMA components are usually involved in large strain applications (strains of the order fo 10^{-1} rather than 10^{-6}).

A constitutive expression can be obtained from the integration of the differential equation 23 with respect to time from the initial conditions $\bar{\varepsilon}_0$, θ_0, ξ_0. Thus

$$\bar{\sigma} - \bar{\sigma}_0 = D(\bar{\varepsilon} - \bar{\varepsilon}_0) + \Theta(\theta - \theta_0) + \Omega(\xi - \xi_0) \tag{24}$$

where D is the elastic matrix, Θ is the thermo-elastic tensor and Ω is the transformation tensor.

However, the SMA device used in the work described in this report operates only in the elastic region and utilises just the change in the Young modulus.

3.2.4. Shape memory effect and superelasticity

The fundamental coupling mechanism in SMA materials is thermomechanical because the stress-strain behaviour is strongly linked to the phase of the material.

Supposing that it operates at a constant temperature, a simplified model could be made in order to explain the two main effects of SMA. In such a model a linear elastic behaviour is exhibited when ξ=1 or 0, but with different stiffness constants, whereas a large increase in strain occurs during the phase transformation. Thus, the stress strain response exhibits two linear elastic regions and a plateau with a large increase in strain (softening) during the phase change (see Figure 13-b in which letters help to follow the several steps; Figure 13-a maps the same steps in the martensite fraction plane). If we load the material when it is in the austenitic phase (step a) we induce the A→M phase change (steps b to c) until reaching a total martensitic state (step d). Now, if we unload the material we induce a residual strain, i.e. a permanent deformation (see step e in Figure 13-b), because the M→A phase transformation will not occur. Only upon heating the wire the martensitic residual strain may be recovered and the material reaches again the step a. This is called **shape memory effect**.

Starting with $\xi=0$ and $\theta>A_f$ (step a of Figure 14) and loading the material, it reaches the full martensitic phase (step d), like in the previous case. But in this case, unloading the

material it passes through the M→A transformation (step e to f), we obtain another softening effect and the material exhibits a hysteresis loop. The area of the hysteresis loop (among the steps b-c-e-f) is equivalent to the amount of energy dissipated during the stress strain cycle. This behaviour is called **superelastic effect**.

A typical ductile material can absorb a large amount energy only when the stress becomes higher than the yield stress of the material so that it undergoes plastic deformation. This property is a problem because repeated loading will eventually cause failure (low cycle fatigue). On the contrary, SMA exhibits a superelastic stress-strain response that make SMA suitable for absorbing and dissipating energy: increasing the applied stress will cause what appears to be a yielding of the material, but reducing the stress back to zero results in zero strain.

3.2.5. Simplified mechanical relations

In the linear region the stress strain relationship is simply (E is the elastic modulus)

$$\sigma = E(\varepsilon - \varepsilon_0)$$

The amount of stress that occurs before the phase transformation depends on the initial temperature of the material and the values of C_M and C_A. At the limit of linear behaviour the equivalent temperature equals the martensite start temperature M_S (see Figure 15-a,b) and

$$\theta_{\lim}^{eq.} = \theta - \frac{\sigma_{\lim}}{C_M} = M_S$$

So at the temperature θ_0 the linear elastic strain is

$$\sigma_{\lim} = C_M(\theta_0 - M_S)$$

The constitutive relationship during a phase transformation, assuming constant temperature, is equal to

$$\sigma = E(\varepsilon - \varepsilon_0) - ES_L(\xi - \xi_0)$$

where S_L is the maximum strain recovery (see Figure 16-a,b), which is a property of the material and is usually given for a particular material.

3.3. Thermal behaviour of a wire of SMA

This subsection concerns the behaviour of a single wire of SMA which may be electrically heated. This will later to be used as a variable stiffness element in a TVA.

The first law of thermodynamics states that the change in internal energy U of a system is equal to the heat added to the system minus the work done by the system. A simple wire does no work so the balance of energy is expressed by

$$\mathrm{d}Q = \mathrm{d}U$$

where Q is heat flow through the system.

The variation of internal energy is related to the change in the temperature θ of the system by

$$\frac{\mathrm{d}U}{\mathrm{d}t} = \rho V c_p \frac{\mathrm{d}\theta}{\mathrm{d}t}$$

where ρ is the density, V is the volume and c_p is the specific heat of the system.

If there are no sources of heat the temperature of the wire tends to the ambient temperature. The only heat exchange is convective dissipation for which the heat loss can be approximated by

$$\frac{\mathrm{d}Q}{\mathrm{d}t} = -\alpha A_e\left(\theta(t) - \theta_a\right)$$

where α is the convective coefficient and A_e represents the surface of heat exchange.

If the wire is heated by a current of intensity I the net heat input is expressed by

$$\frac{\mathrm{d}Q}{\mathrm{d}t} = I^2 R - \alpha A_e\left(\theta(t) - \theta_a\right)$$

where the electrical resistance R of the wire is

$$R = \rho_e \frac{L}{A}$$

setting ρ_e as the electrical resistivity and, L and A as the length and the cross section of the wire.

So, when the wire cools down, it follows that

$$\begin{cases} \rho V c_p \dfrac{\mathrm{d}\theta}{\mathrm{d}t} = -\alpha A_e\left(\theta - \theta_a\right) \\ \theta(t=0) = \theta_0 \end{cases}$$

Given the initial condition, the temperature is given by

$$\theta(t) = \left(\theta_0 - \theta_a\right)e^{-t/\tau} + \theta_a \tag{25}$$

in which the time constant τ is

$$\tau = \frac{\rho V c_p}{\alpha A_e} \tag{26}$$

In the same way, when the wire heats up, it satisfies

$$\begin{cases} \rho V c_p \dfrac{\mathrm{d}\theta}{\mathrm{d}t} = I^2 R - \alpha A_e (\theta - \theta_a) \\ \theta(t=0) = \theta_0 \end{cases}$$

whose solution, given the initial condition, is

$$\theta(t) = [\theta_0 - (\theta_a + \beta)] e^{-\frac{t}{\tau}} + (\theta_a + \beta) \tag{27}$$

in which the "current constant" β is defined as

$$\beta = \frac{I^2 R}{\alpha A_e} \tag{28}$$

This term represents the difference between the steady state "hot" temperature and the ambient temperature. In the limit of $t \to \infty$ equation 27 becomes

$$\theta(\infty) = \theta_a + \beta \tag{29}$$

For SMA devices, it is important also to consider the release and absorption of the latent heat of phase transformation, ΔH, which tends to slow down heating as well as cooling [19, 20]. When an electric current circulates in a SMA wire, its temperature increases according to the exponential equation. When the wire temperature reaches A_s the material begins to absorb energy to sustain phase transformation. Once the phase transformation is over the temperature of the wire increases again in an exponential manner. In the same way, when the current is shut off the wire starts to cool down but at the temperature M_s the material begins to release the latent heat of transformation until phase transformation is over.

Physically, during the phase transformation the internal energy of the wire is expressed by

$$\frac{\mathrm{d}U}{\mathrm{d}t} = \rho V \left(c_p \frac{\mathrm{d}\theta}{\mathrm{d}t} - \Delta H \frac{\mathrm{d}\xi}{\mathrm{d}t} \right)$$

This equation is inconvenient because of the presence of the differential of the martensitic fraction. An estimate of the order of magnitude of the influence of the transformation on the response of the SMA wire can be formed by computing the time taken for the transformation to occur. Supposing the phase transformation is isothermal, the transformation time is given by

$$\Delta t = \frac{-\rho V \Delta H \Delta \xi}{I^2 R - A_e (\theta_t - \theta_a)}$$

where the temperature of transformation can be approximated by

$$\theta_t = \begin{cases} \dfrac{M_s + M_f}{2} & \text{Austenite} \rightarrow \text{Martensite transformation} \\ \dfrac{A_s + A_f}{2} & \text{Martensite} \rightarrow \text{Austenite transformation} \end{cases}$$

A physically realistic approximation of this process can be realized by approximating the experimental curve of the heat flow (see Figure 17) by a second order polynomial to model the change of specific heat during the phase transformation [20], i.e.

$$\hat{c} = \begin{cases} a\theta^2 + b\theta + d & \text{during phase transform.} \\ c_p & \text{otherwise} \end{cases}$$

The latent heat of transformation is calculated by integrating the specific heat with respect to temperature

$$H = \frac{1}{A_f - A_s}\int_{A_s}^{A_f} \hat{c}\,\mathrm{d}\theta = \frac{1}{M_s - M_f}\int_{M_f}^{M_s} \hat{c}\,\mathrm{d}\theta$$

A rough approximation of this behaviour could be made by considering the specific heat during the phase transformation to take a different value which includes the latent heat of transformation. Moreover to avoid the problem due to the hysteresis we can pose a simple equation for the specific heat, namely

$$\hat{c} = \begin{cases} e \cdot c_p & M_f \le \theta \le A_f \\ c_p & \theta < M_f; \theta > A_f \end{cases} \tag{30}$$

Figure 18 shows the expected effect of such approximation.

The steady state temperature of the system when a current I is passed through the wire can be found from

$$\left.\frac{\mathrm{d}Q}{\mathrm{d}t}\right|_{t=\infty} = I^2 R - \alpha A_e\left(\theta(\infty) - \theta_a\right) = 0$$

The convective coefficient is given in terms of the steady state temperature as

$$\alpha = \frac{I^2 R}{A_e\left(\theta(\infty) - \theta_a\right)} \tag{31}$$

3.4. Nickel-Titanium alloys (Nitinol) properties

For the vibration neutralizer, Nitinol SM495 wire, with a diameter of 2 mm was used. Table 2 shows material properties provided by the company. It is believed that this refers to the properties of the material in the martensite state.

The company comments on this data as follows: “These values should only be used as guidelines for developing material specifications. Properties of Nitinol Alloys are strongly dependent on processing history and ambient temperature. The mechanical and shape memory properties shown here are typical for standard shape memory wire at room temperature tested in uniaxial (tensile) tension. Bending properties differ, and depend on specific geometries and applications. Modulus is dependent on temperature and strain. Certain shapes or product configurations may require custom specifications.”

The company also add to each sample the results of a free-recovery test in which are reported the measured temperatures of austenite transformation. Table 3 shows the results of such a test.

Table 4, extracted from different papers and books [9, 10, 14, 21], synthesizes the most important values necessary to make provision for the behaviour of a SMA component. For instance, from this table we can infer that the Young modulus should increase by 2-3 times from the martensite to the austenite state. However, the experimental results in this report described in subsection 5.2 showed that there were significant discrepancies between data provided by the company and the estimated values.

Table 5 shows the values used in the calculations to predict the behaviour of the Nitinol wire used in the project, that have showed a good agreement with the experimental tests. All the values cited have been measured except the latent heat of transformation because of the lack of the proper equipment (see section 5).

3.5. Achieving control structures using SMA

SMA devices have been publicised in many fields but, in engineering, these materials have been used mainly as force actuators. They also offer vibration control potential based on three important principles [11]: 1) the large increase in the elastic modulus in the transition from martensitic to austenitic phase; 2) the creation of internal stresses; 3) the dissipation of energy through inelastic hysteresis damping.

For instance, Baz et al [19] demonstrated theoretically and experimentally the feasibility of utilizing SMA in controlling the flexural vibration of a flexible cantilever beam. They controlled the cantilever beam by means of two SMA wires mounted on the opposite side and placed external to the structure in order to enhance the cooling. The two actuators were used to control only the first bending mode of the beam. A non contacting sensor measured the flexural deflection and the error signal was used to

trigger an on-off controller with a controlled dead band. The control action was sent to two power amplifiers that energized the actuators to provide the control forces. The excitation was just a step imposed at the free end.

Moreover SMA could also be used to build an active tuned vibration absorber (ATVA). Liang and Rogers explored two different techniques for SMA in vibration control [9, 22, 23]. The first was active properties tuning (APT), where the change in the elastic modulus of SMA with heating was used to modify the dynamic characteristics of a composite plate in which the SMA wires had been embedded. The other technique was the active strain energy tuning (ASET). In that application, SMA elements were given initial plastic strains before insertion into a composite material. Heating the SMA then resulted in in-plane forces within the plate, with subsequent changes in the structure's natural frequency and mode shapes.

In some applications it is not practical to redesign an entire structural system to apply this technique. An alternative approach is to use just the adaptive properties of SMA to realize an ATVA. An SMA spring element whose stiffness is directly dependent on the elastic modulus of the spring material can be constructed as the adaptive spring in an ATVA. Following the work of Liang and Rogers, Williams et al [9] designed and built an ATVA using spring elements composed of three pairs of SMA wires and one pair of steel wires. On/off actuation of the SMA elements created an ATVA with four discrete tuned frequencies. The absorber showed variation of the natural frequency of approximately 15%. Manual tuning of the ATVA actuation during a stepped-sine base excitation of the primary system showed a wider notch of attenuation than was possible with a non-adaptive absorber.

An other problem rising from the use of SMA is the choice of the proper control. Classical control could be a first step but much better results could be obtained by means of modern control techniques. Actual structures are very complex, nonlinear in behaviour, and subject to load spectra that could vary during the structure's life. To address these problems, at least three adaptive control approaches are suggested by Giurgiutiu [11]: (i) adaptive signal processing; (ii) model reference adaptive control; (iii) self tuning regulator. Moreover, some researchers prefer to compensate the inherent non-linearity associated with SMA using sliding mode controller [24, 25].

The main limitations of the SMA absorber are the slow response time (bandwidth is limited due to heating and cooling restrictions and can only achieve a few Hz at best) and the poor energy conversion efficiency when actuated with an electrical signal. The

response times of SMA components are limited by heat transfer. Very rapid heating could be achieved employing very intense currents, but the time needed for cooling is always long compared to the vibratory period of common mechanical structures. For SMA actuators an approach has been found suitable to overcome this inherent limitation [10]. The approach is based on using several SMA wires in parallel and putting current in subsets of these during successive cycles. For instance a rectangular pulse could be used and multiplexed on several parallel wires to increase the frequency response of the actuators.

Moreover, SMA has no sensing capability (even if the electric resistance value of SMA could be utilized to monitor the phase transformation [26]) and usually they need complex control systems.

3.6. Summary

The main advantage of SMA materials is their capability to recover large strain (up to 10%) with a high power/weight ratio. In addition, they have inherent simplicity, compactness, and they contribute to a clean, silent and spark-free working condition.

Future research aims to develop magnetic shape memory materials in order to increase the speed of response of the material. Moreover magnetic shape memory alloys can function both as sensors and as actuators. Recently shape memory polymers have received an increasing interest. They possess the same basic shape memory effect and elasticity memory effect as shape memory alloys, but they can change their elastic modulus up to 500 times around their glass transition temperatures.

The previous section showed how to design a TVA. This section has introduced the SMA properties and the mathematical description of such properties has been given. A thermal and mechanical model of SMA wire has been described. Also a short review of the application of SMAs has been presented. In the next section all the basic theory described in the previous sections will be used to design a SMA wire TVA.

Figures

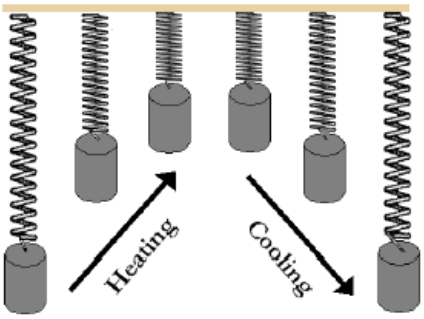

Figure 8 The typical behaviour of a SMA spring.

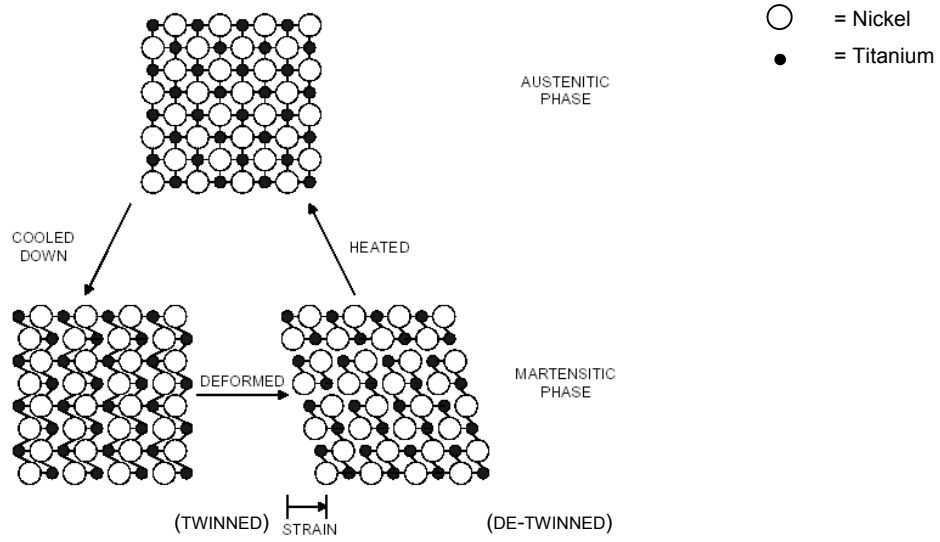

Figure 9 Change in crystal structure accompanying phase change in shape memory alloy [10]

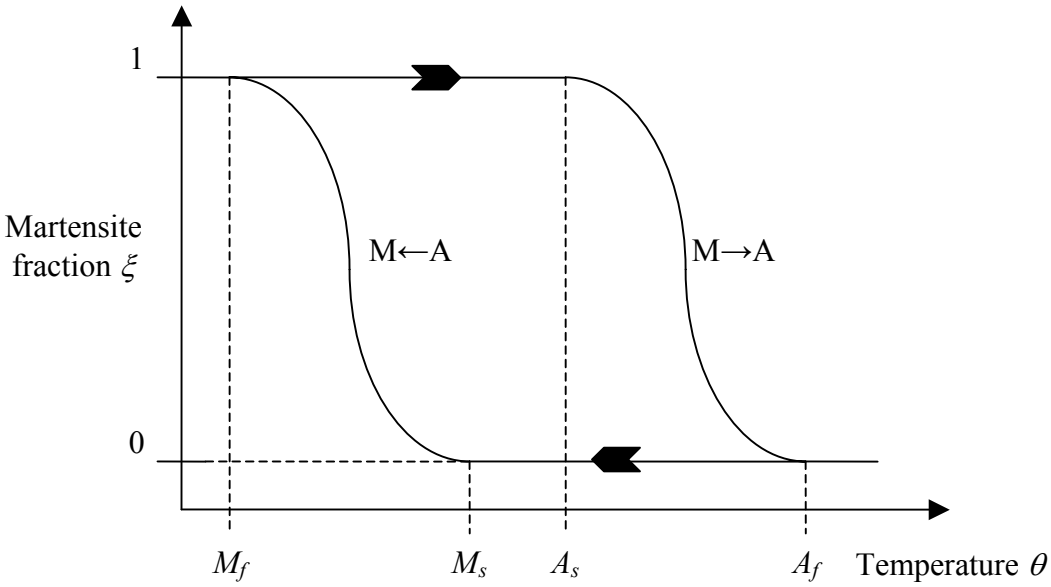

Figure 10 Mathematical modelling of martensitic fraction in SMA

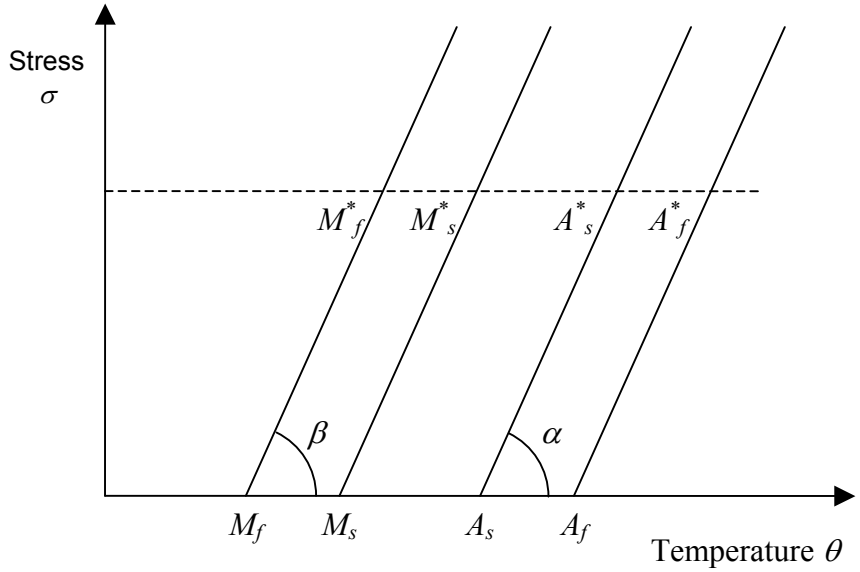

Figure 11 Influence of stress on critical phase change temperatures

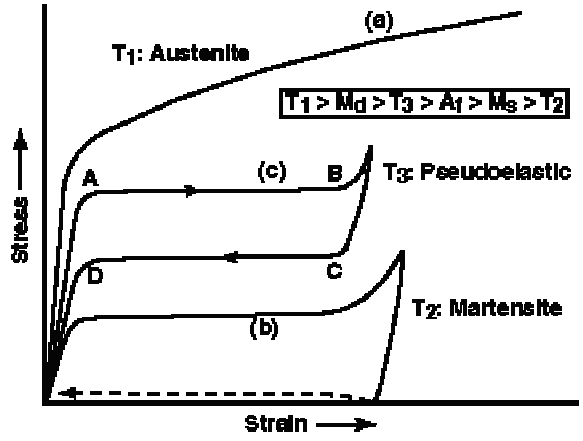

Figure 12 Mechanical behaviour of a SMA in austenite, martensite and transition state [14]

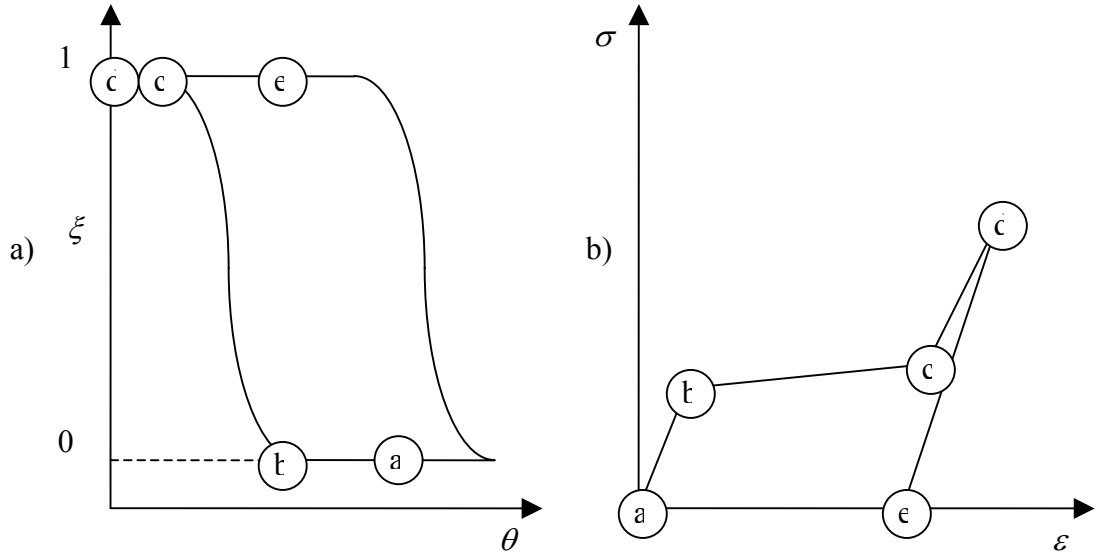

Figure 13 Shape memory effect: a) martensite fraction plane; b) stress strain behaviour of austenite-martensite alloy

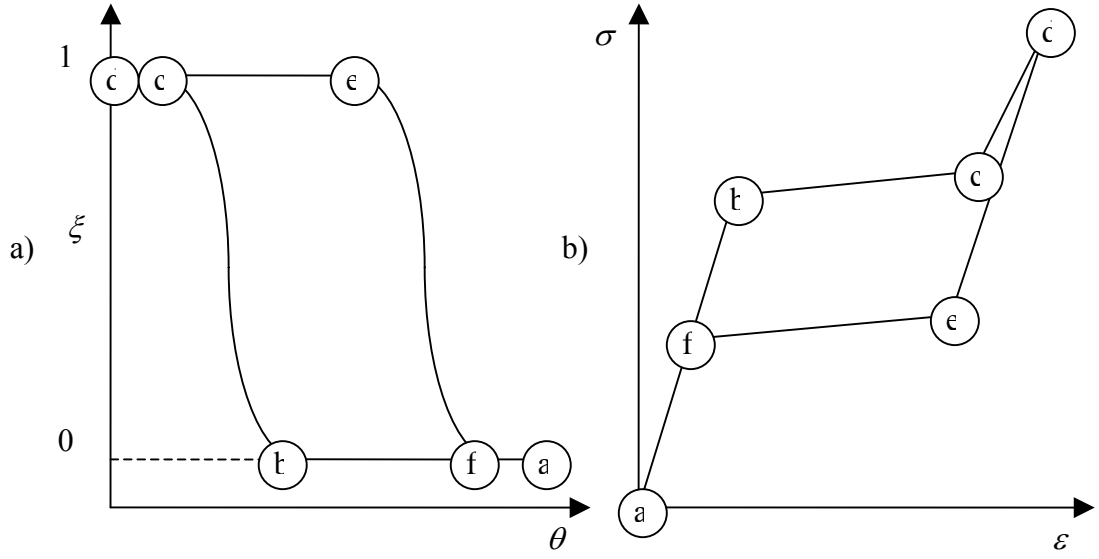

Figure 14 Super-elasticity effect: a) martensite fraction plane b) stress strain plane

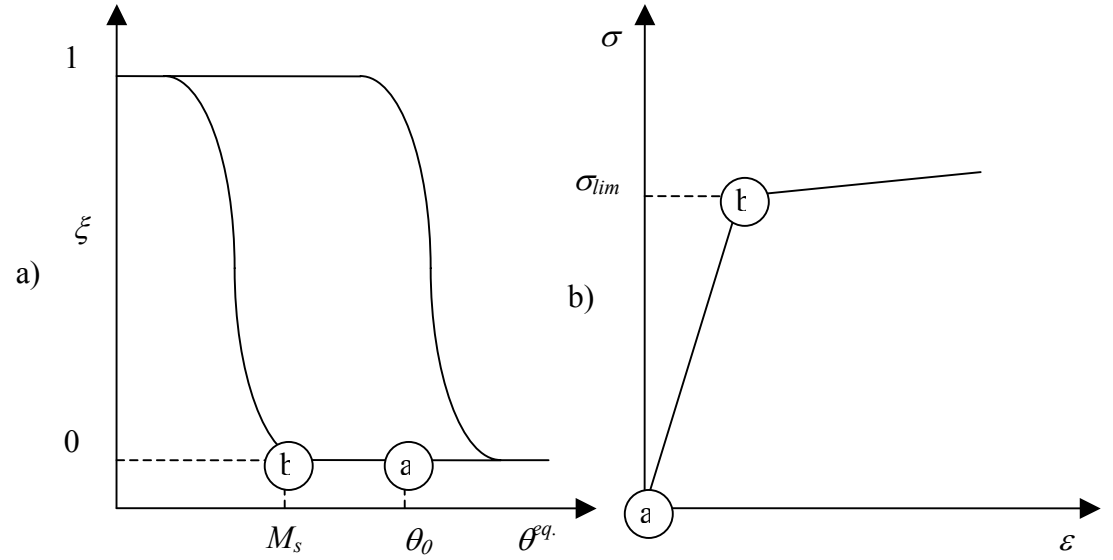

Figure 15 Linear elastic stress limit: a) martensite fraction plane b) stress strain plane

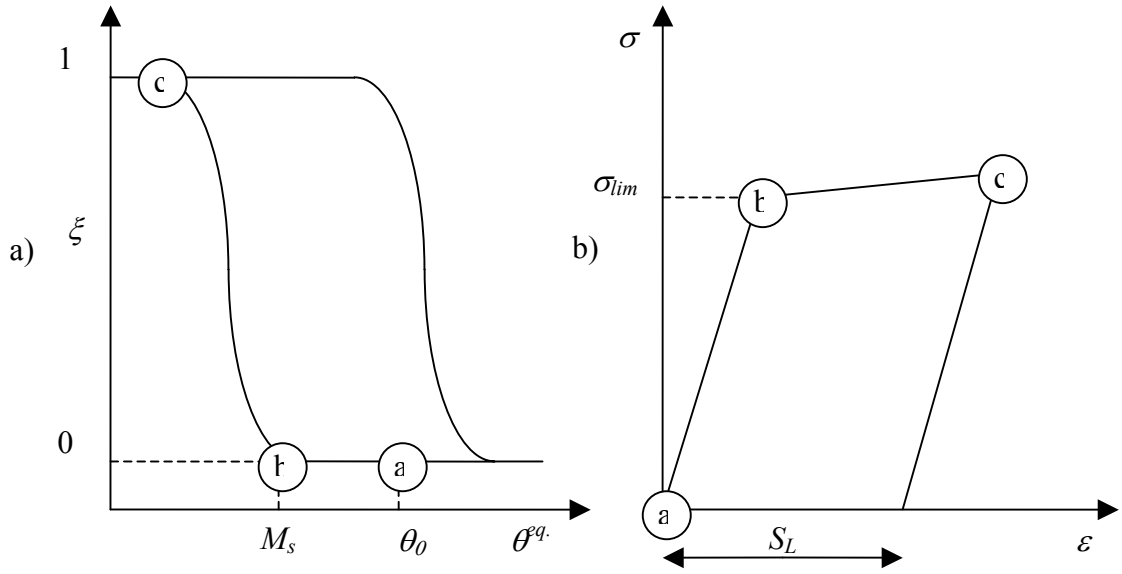

Figure 16 Constitutive modelling at constant temperature : a) martensite fraction plane b) stress strain plane

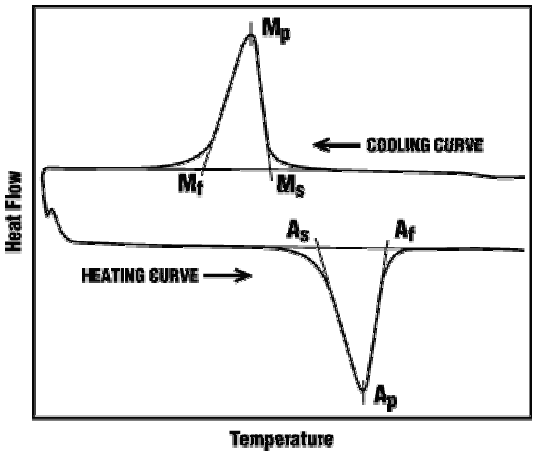

Figure 17 Experimental curve of the heat flow during phase transformations [27]

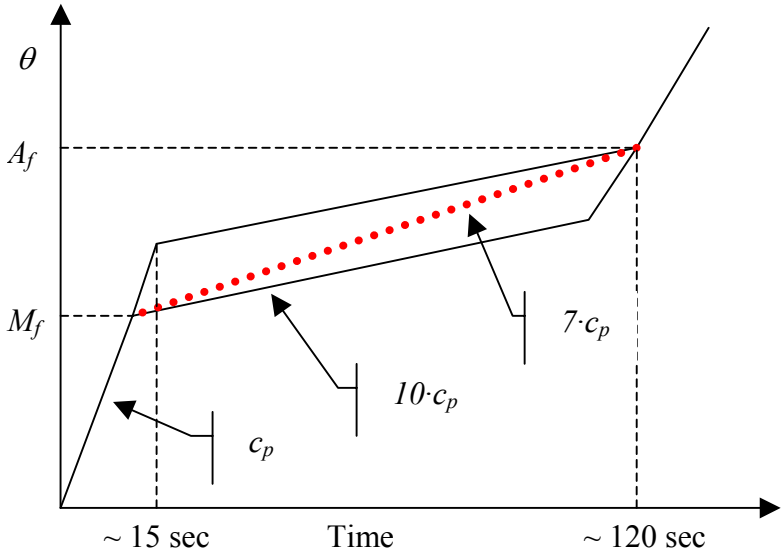

Figure 18 Heating up and cooling down curves through transition and (·····) approximated curve (numerical data have been inferred from the experimental works)

Tables

PHYSICAL PROPERTIES	Melting Point	1310 °C
	Density	6450 kg/m^3
	Electrical Resistivity	$0.76 \cdot 10^{-6}$ Ωm
	Modulus of Elasticity	$28\text{-}41 \cdot 10^3$ MPa
	Coefficient of Thermal Expansion	$6.6 \cdot 10^{-6}$ °C^{-1}
MECHANICAL PROPERTIES	Ultimate Tensile Strength (UTS) (min)	1100 MPa
	Total Elongation (min)	10%
SHAPE MEMORY PROPERTIES	Loading Plateau Stress @ 3% strain (min)	100 MPa
	Shape Memory Strain (max)	8.0%
	Transformation Temperature (A_f)	60 °C
COMPOSITION (in weight percent)	Nickel (nominal)	54.5 wt.%
	Titanium	Balance
	Oxygen (max)	0.05 wt.%
	Carbon (max)	0.02 wt.%

Table 2 Nitinol SM495 wire physical properties [28]

A_s	A_f
66.11 °C	73.25 °C

Table 3 Austenite transition temperatures

Young's Modulus[2]	austenite	approx. 83 GPa
	martensite	approx. 28 to 41 GPa
Yield Strength	austenite	195 to 690 MPa
	martensite	70 to 140 MPa
Ultimate Tensile Strength	fully annealed	895 MPa
	work hardened	1900 MPa
Poisson's Ratio		0.33
Elongation at Failure	fully annealed	25 to 50%
	work hardened	5 to 10%
Hot Workability		quite good
Cold Workability		difficult due to rapid work hardening
Machinability		difficult, abrasive techniques preferred
Resistivity	austenite	approx. $1 \cdot 10^{-3}$ Ωm
	martensite	approx. $0.8 \cdot 10^{-3}$ Ωm

Table 4 Common mechanical properties of SMA

Austenite start temperature	A_s	45 °C
Austenite finish temperature	A_f	60 °C
Martensite finish temperature	M_f	35 °C
Martensite start temperature	M_s	50 °C
Martensite Young modulus	E_1	40 GPa
Austenite Young modulus	E_0	59 GPa
Loss factor	η	0.0175
Specific heat	c_p	322 J/(kg K)
Latent heat of transformation	H	24200 J/kg

Table 5 Experimental data collection; details of measurement are in Section 5

[2] Highly nonlinear with temperature

4. Design of the test rigs

4.1. Introduction

This section outlines the design and set-up of the experimental test rigs. As described in section 2, in this report a beam vibration absorber is studied. The aim was to build an SMA TVA using a simple beam configuration. As SMAs are sold only in a few shapes, among which wire is one, and they could be soldered and worked only with much difficulty the simplest configuration of TVA was chosen. Moreover, wires allow direct heating with current. Even though this was simple, this particular configuration has not been deeply studied before.

In a preliminary study a brass TVA was constructed (subsection 4.2). Brass wire was used because it has mechanical properties very similar to those of Nitinol SMA, and its thermo-mechanical behaviour is well understood. Some preliminary tests were carried out on this test rig (subsection 4.3), after which a SMA TVA was designed (subsection 4.4).

4.2. Brass test rig

The design of the test rig was straightforward. The resonance frequency was chosen to be between 80 and 120 Hz. For a given diameter of wire, this determines the length.

Moreover, so that the thermal behaviour of a wire could be measured the test rig was equipped with a thermocouple. In order to evaluate the convective heat transfer coefficient the temperature of the wire and that of the air were measured.

Figure 19 shows the design of the TVA. It was connected to a shaker via a stud and an impedance head. The length of the brass wire was determined by the range of the resonance frequency. Figure 20 shows a picture of the brass TVA.

The dynamic characteristics of the test rig were calculated using the equations reported in section 2. The mechanical properties used for the brass wire are shown in Table 6. The dimensions of the test rig are given in Table 7.

The only problematic issue was the feasibility of realizing the proper boundary condition without making the structure too heavy. A free-free beam supported in the middle is symmetric, so the slope at the middle is zero. In order to realize such a boundary condition the centre of the wire was supported in a Jelutong wood block. This wood is a good electrical insulator, has a high yield stress together with a very low

density. The high yield stress allows the proper boundary conditions to be realized and the low density ensures there is not too much influence on the dynamics of the system. Table 8 shows the main properties of the Jelutong wood.

As shown before (see subsection 2.2), we can find the properties of an equivalent 2dof system (Figure 6). The characteristics are given in Table 9.

Figure 21 shows the predicted impedance of the brass test rig. The impedances of both a free-free beam (obtained from equation 13) and a 2dof approximation are shown (obtained from equation 6 and 15).

4.3. The brass TVA experimental tests

The experimental set-up used to investigate the behaviour of the brass TVA consisted of the following equipment: an ICP® impedance head transducer (PCB 288D01), LDS shaker (V201), a constant-current signal conditioner, a noise generator, an amplifier, an ammeter with 1A full-range fuse, a spectrum analyser (Hewlett Packard), an oscilloscope, a 10 A ammeter, a thermocouple, a 10 A current generator and the test rig. The diagram in Figure 22 illustrates the rig schematically.

In Table 10 the properties of the impedance head are given, while Table 11 shows the settings used for the HP analyzer.

Figure 23 shows the measured point impedance at the middle of the beam. In Figure 24 the same results are shown in a polar plot. Figure 25 shows the coherence of the measurements. The theoretical results in Figure 23 and Figure 24 include the mass of the test rig, but there are still large differences between the two responses. In order to obtain an accurate and suitable model, the parameters of the two dof system were estimated by fitting such a model to the experimental results. The test rig was weighed. The results are reported in Table 12. The mass m_1 was increased by 20 grams (about the weight of the Jelutong and aluminium block) and the mass m_2 by 0.5 grams (approximately the weight of the soldering points). The very good agreement can be see in Figure 23. The stiffness in the model has not been changed.

After preliminary checks on the experimental results the circle fitting method was applied to estimate the modal properties of the first mode of the system. Table 13 shows the results of the analysis. Figure 26 and Figure 27 show the results.

To confirm that the TVA behaves in a linear manner a simple linearity test was carried out, by measuring the FRFs at different excitation loads. Figure 28 shows the result. Moreover, the electrical wires were fixed to the rig by adhesive tape but the results

were better without the tape (see Figure 29) because of the not-negligible stiffness of the wires.

Thermal tests were carried out to find an estimate for the convective coefficient. A current was imposed (see Table 14) and the ambient temperature and that of the wire at the starting and final time of each test were measured. Each test took 5 minutes and six tests were carried out in order to obtain an averaged value. The tests were carried out without vibrating the TVA. For each test, the convective coefficient α has been calculated using the equations 28 and 29. The results, shown in Table 15, show that the average convective coefficient $\overline{\alpha}$ is 20.53 N/m^2K, which is a reasonable value, in accordance with values in the literature.

4.4. SMA test-rig

The SMA TVA was designed in the same way as the brass TVA as described in the subsection 4.2. The mechanical properties used were those given in section 3 (see Table 2 and Table 4). Figure 30 shows the final drawing of the TVA whereas Figure 31 shows the TVA fixed to the impedance head and connected to the shaker.

The theoretical input impedance of the SMA TVA based on a 2dof model is shown in Figure 32, where also the impedance of a steel TVA of the same dimensions is shown. The dimensions of the TVA are shown in Table 16. For the steel a density of 7800 kg/m^3 and a Young modulus of 210 10^9 Pa has been used. For the SMA, a density of 6500 kg/m^3 was adopted. The Young modulus of the SMA was set at 40 10^9 Pa for the cold state (martensitic phase) and 100 10^9 Pa for the hot state (austenitic phase). As was done for the brass TVA the parameters of an equivalent two dof system were estimated for the SMA TVA and are shown in Table 17.

Finally adopting the same corrections for the masses adopted for the brass test-rig, gave the impedances shown in Figure 33.

4.5. Summary

After designing and setting up a free-free beam TVA made using a brass wire a similar device using SMA wire has been built. The SMA TVA has been subjected to some preliminary tests. The experimental study is outlined in the next section.

Figures

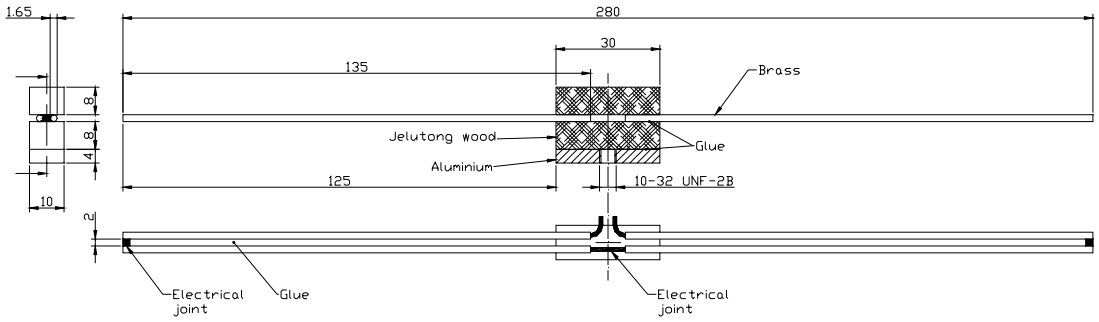

Figure 19 Drawing of the brass test rig

Figure 20 Picture of the brass test rig

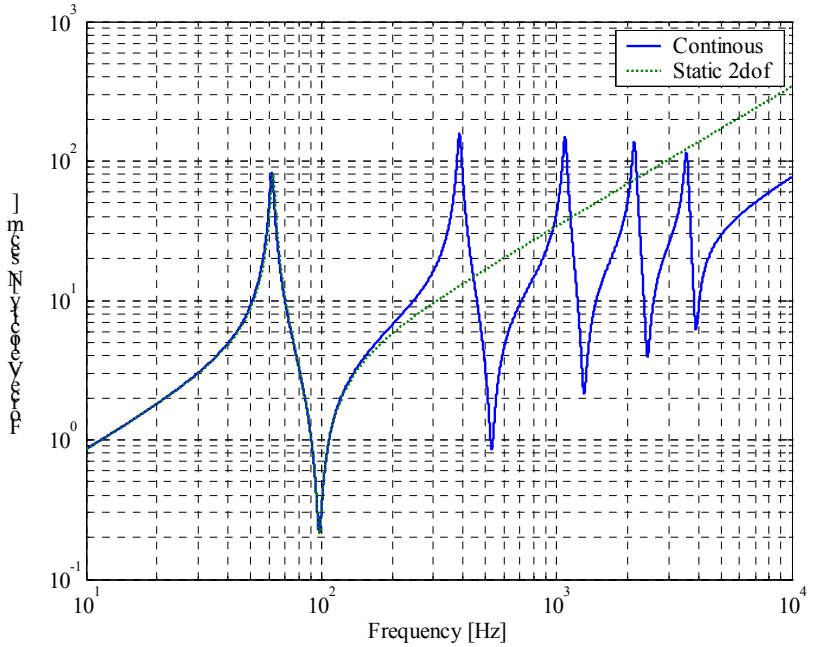

Figure 21 Predicted impedance of the brass test rig: the continuous line is the impedance of the free-free beam whereas the hatched one is that of the two dof approximation

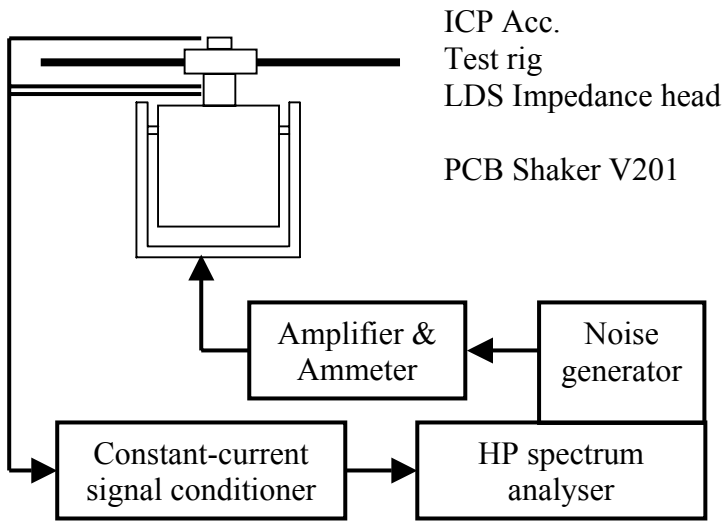

Figure 22 Outline of the test rig set-up

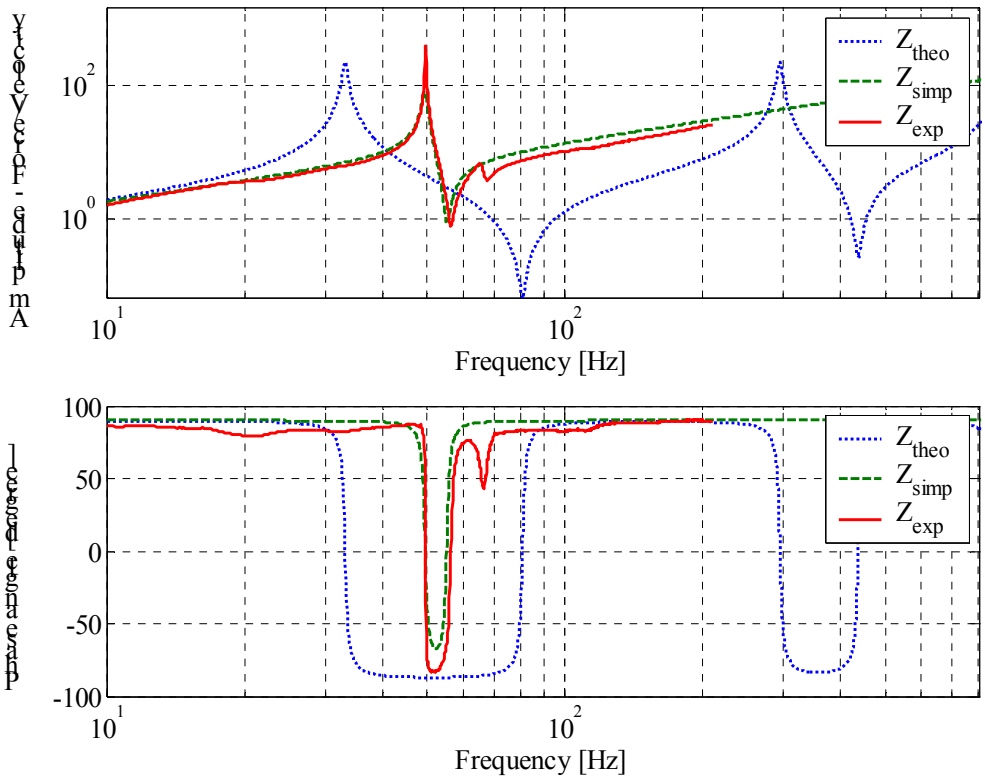

Figure 23 Comparison between calculated and experimental FRF impedance:
—— measured; · · · · beam model; - - - - 2 dof approximation

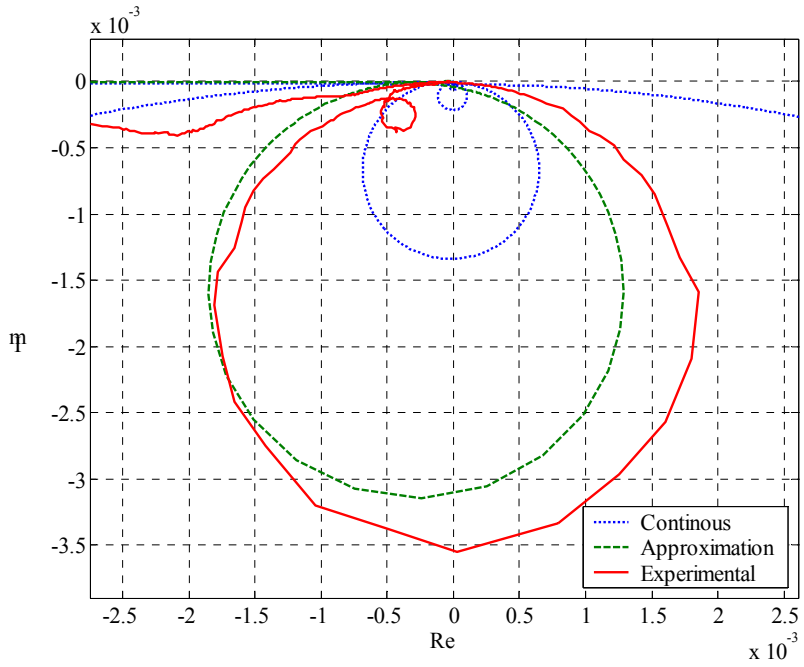

Figure 24 Polar plot of receptance: —— measured; · · · · beam model; - - - - 2 dof approximation

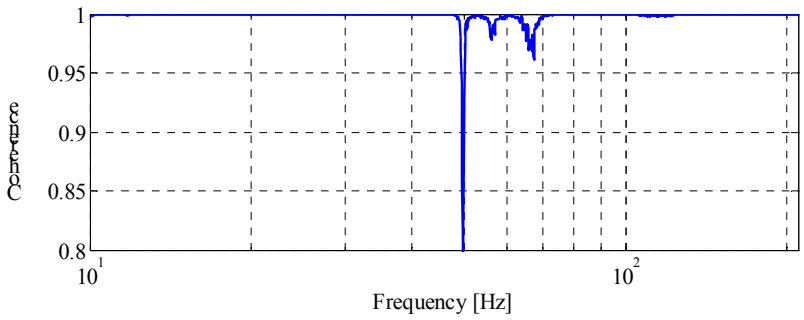

Figure 25 Coherence of the experience

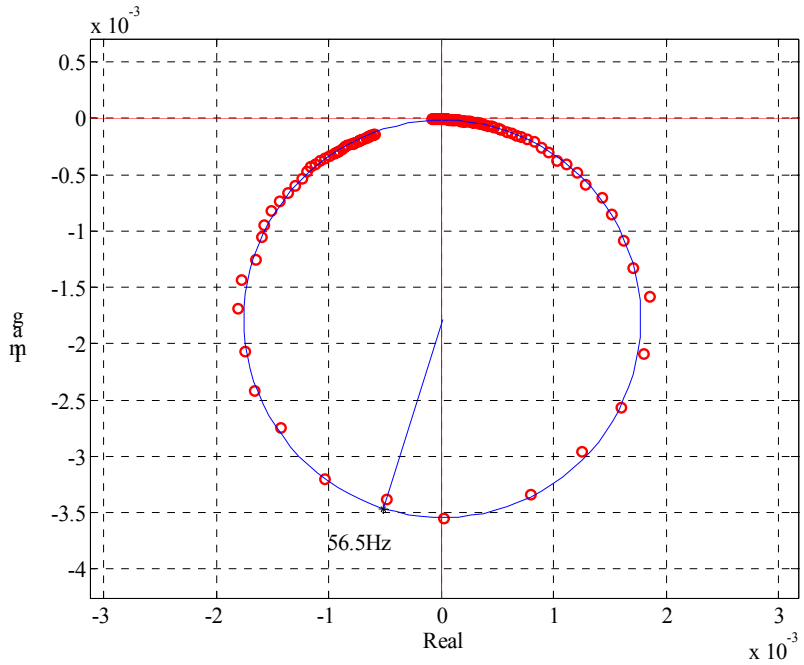

Figure 26 Circle fitting on the experimental receptance points

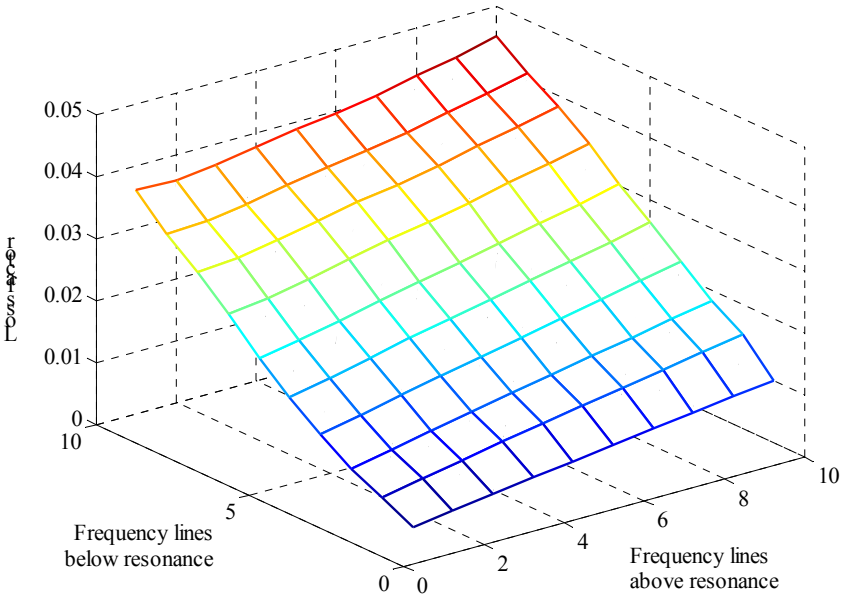

Figure 27 Carpet plot of the estimated loss factor

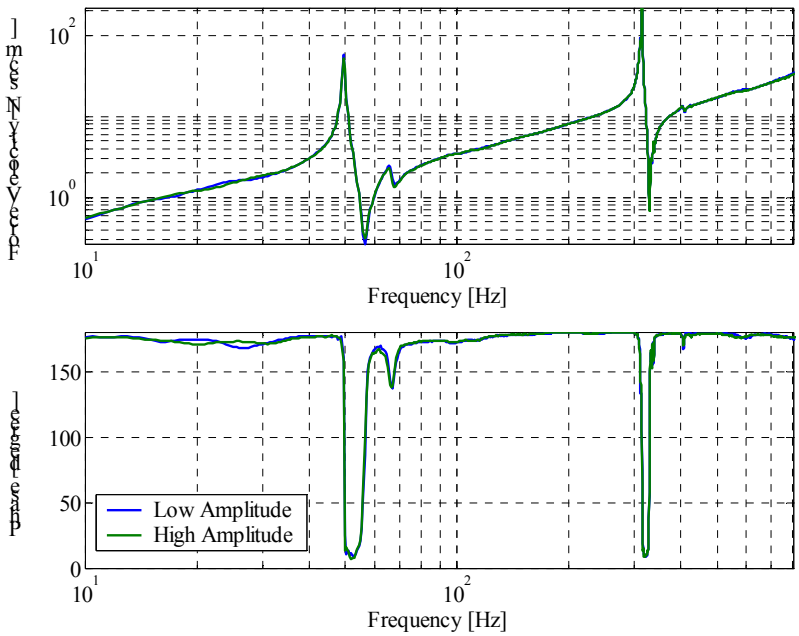

Figure 28 Comparison between experimental impedance FRF obtained with different amplitudes of excitation

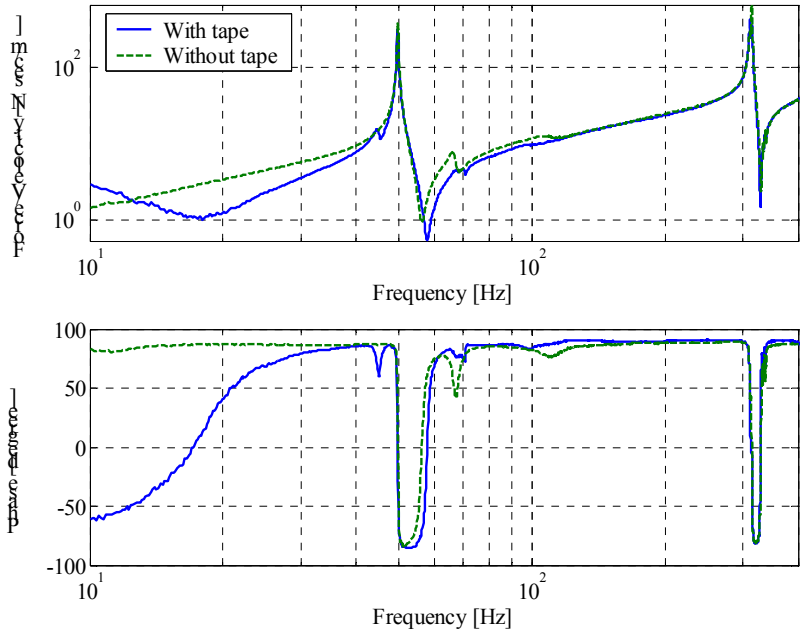

Figure 29 Comparison between experimental impedance with and without adhesive tape to support the heating wires

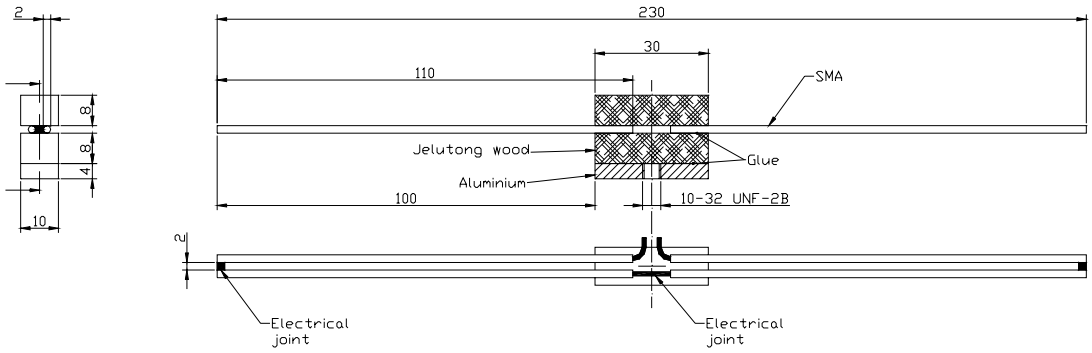

Figure 30 Drawing of the SMA test rig

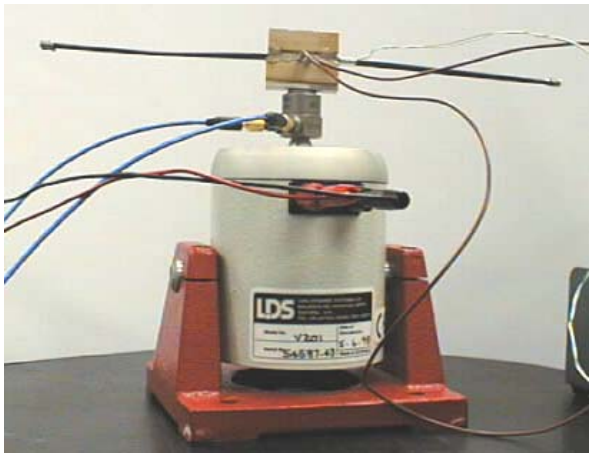

Figure 31 The SMA test rig: the SMA TVA is attached to the shaker through the impedance head

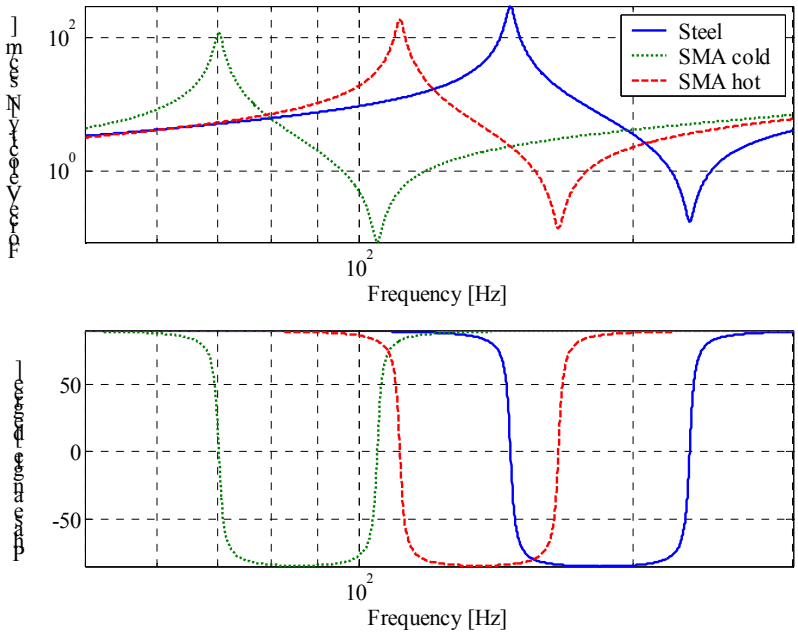

Figure 32 Predicted behaviour of the SMA TVA (hatched line for austenite state and dotted line for martensite state) compared to a steel TVA (continuous curve);Loss factor $\eta=0.018$

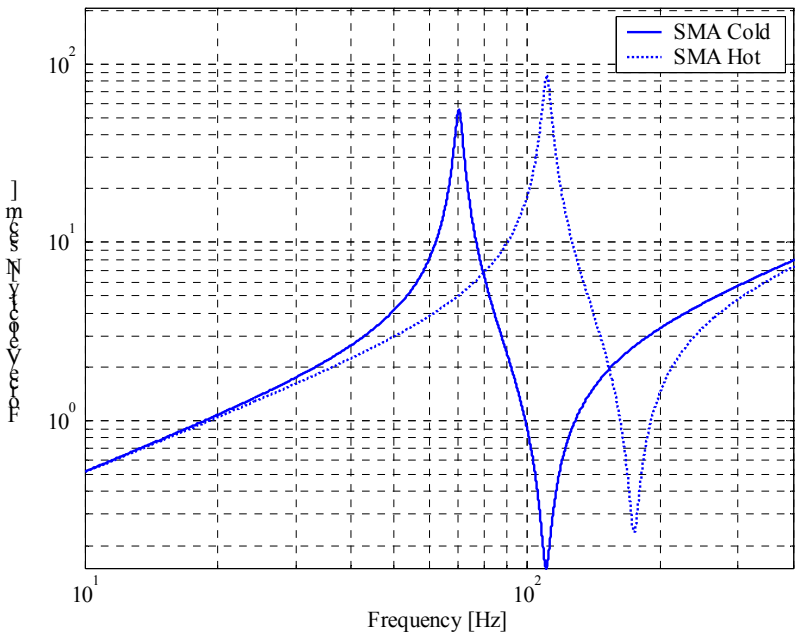

Figure 33 Predicted behaviour of the SMA TVA corrected with the adjustments made for the brass TVA; · · · · austenite state ; —— martensite state

Tables

Yield stress	Y_s	115-390 MPa
Young modulus	E	101 GPa
Density	ρ	8550 kg/m^3
Specific heat	c_p	370 J/(kg K)
Electrical resistivity	ρ_e	$62 \cdot 10^{-9}$ Ωm

Table 6 Brass (70/30) mechanical properties

Total Length	L	0.25 m
Diameter	d	0.00165 m

Table 7 Main dimensions of the brass test rig

Modulus of rupture	Young modulus	Density
Y_R	E	ρ
38.6-50.3 GPa	8.0-8.1 GPa	360 kg/m^3

Table 8 Jelutong (Dyera costulata) mechanical properties

m_1	m_2	k	f_a	f_r
0.0054 kg	0.0080 kg	1223 N/m	~ 62.2 Hz	~ 97.9 Hz

Table 9 Brass vibration neutralizer properties

Accelerometer	Sensitivity:	-10.2 mV / m·s^{-2} ±10%
	and on the signal conditioner	x1
	Measurement range:	±5V = ±490.5 m·s^{-2} pk
	Frequency range (±5%)	1 to 5000 Hz
Force transducer	Sensitivity:	22.4 mV / N ±10%
	and on the signal conditioner	x10
	Measurement range:	±5V = ±222.4 N pk

Table 10 Impedance head ICP® PCB 288D01 characteristics

Hardware set-up	Active channels:	2
Source:	Type:	Continuous random
	Output:	1 V
	Amplifiers:	0.1 A on ammeter
Input set-up/Front end ranges	1 - force transducer:	auto-range
	2 - accelerometer	auto-range
Acquisition properties	Start frequency:	10 Hz
	Span frequency:	200 Hz
	Frequency line:	1600
	Average type:	Stable
	Number of average:	20
	Window:	Hanning
	Exponential time constant:	1000 sec
	Force width:	1000 sec
	Reference mode:	Single channel
	Ref. Channel:	1
	Overload reject:	■
	Manual preview:	□
	Manual arm:	□
	Overlap:	0 %

Table 11 Setting of HP analyser

Total weight (test rig and wires):	27.9 g
Approximated test rig weight: *(wire supported by ground)*	18.3 g

Table 12 Weight of the brass test rig

Natural frequency:	56.50 Hz
Loss factor:	0.0227
${}_rA_{jk}$:	9.615-i 3.005
${}_rB_{jk}$:	(5.374-i 1.070)·10^{-4}

Table 13 Results of the circle fitting (see appendix A. Circle fitting - SDOF modal analysis)

Current	I	8 A
Single test duration	Δt	5’ (minutes)
Diameter	d	0.00165 m
Length	L	0.500 m
Area of heat exchange	A_e	0.0025918 m^2
Resistivity	ρ_e	6.20E-08 Ωm
Resistance	R	0.0144979 Ω

Table 14 Characteristics of thermal tests

Test	Ambient Temperature	Temperature of the wire after 5 min.	Convective coefficient	
n°	θ_a [°C]	$\theta_{5'}$ [°C]	α [W/m^2K]	
1	21.6	39.3	20.22	
2	21.4	39.6	19.67	
3	20.4	37.5	20.93	
4	20.5	37.9	20.57	
5	21.0	38.5	20.46	$\overline{\alpha}$
6	21.2	38.0	21.31	20.53

Table 15 Experimental evaluation of the convective coefficient

Total Length	L	0.2 m
Diameter	d	0.002 m

Table 16 Main dimensions of the SMA test rig

	m_1	m_2	k	f_a	f_r
COLD STATE	0.0033 kg	0.0049 kg	946.2 N/m	70.1 Hz	110.4 Hz
HOT STATE	0.0033 kg	0.0049 kg	2365.6 N/m	110.9 Hz	174.6 Hz

Table 17 SMA TVA predicted properties (simplified 2 dof system)

5. SMA experimental work

5.1. Introduction

The SMA TVA designed in the section 4 is now studied in order to validate its effectiveness. First some preliminary tests were carried out in order to examine the behaviour of such a device in the cold (martensitic phase) and in the hot state (austenitic phase). Then similar tests were carried out at several temperatures in order to outline the steady state characteristics of the SMA TVA. An analysis of the dynamical behaviour of the device during heating and cooling completes the section.

5.2. Preliminary tests

Two preliminary tests were carried out to fit the parameters of the 2dof models to the experimental data and estimate the increase of the Young modulus from the cold to the hot state.

The first test was carried out at the ambient temperature. Data are shown in Table 18 which shows the temperature of the SMA wire and the ambient temperature. The difference of 2°C between the temperature of the wire and the ambient temperature could be attributed to the poor precision of the two thermocouples used. The same test carried out for the brass TVA was carried out on the SMA TVA in the cold state. All the settings were the same as those reported in section 4.

Figure 34 shows the experimental results. In order to fit the measured data mass m_1 was increased by 18 grams and the mass m_2 by 1 gram and the loss factor η was set to 0.018. Figure 35 shows the coherence of the measurement while Figure 36 shows a complex plot of the measured receptance FRF.

Applying the circle fitting method (see appendix A. Circle fitting - SDOF modal analysis) to the experimental data gave the results of Table 13. Figure 37 shows the circle fit and Figure 38 draws the respective carpet plot.

The same test was then carried out on the SMA TVA in the hot state (see Table 20). Figure 39 shows the experimental results, with the theoretical result using the change in elastic modulus expected from the manufacturers data. It is evident that the change in elastic modulus of the SMA TVA is lower than that expected. The loss factor η was set to 0.017. Figure 40 shows the coherence of the measurements whereas in Figure 41 the same results are shown in the complex plane. Applying the circle fitting method to the

experimental data gave the results in Table 21. Figure 42 shows the circle fit and Figure 43 draws the respective carpet plot.

As has already been noted, the increase in the Young modulus is less than that expected. An increase of at least 150% from the martensite to the austenite states was expected from the manufacturer data, i.e. an increase from 40 GPa to 100 GPa in the Young modulus. However, an increase of only 47.5% was obtained. The Young's modulus in the hot state was estimated to be 59 GPa, and this gave the predictions shown in Figure 44. The reason for the differences, could be that the dynamic properties of the SMA are different from the static ones and that the bending response is different from the tensile response.

Notwithstanding, the increase in the tuned frequency is about 14 Hz (see Table 17), giving an increase of 17.5%. Such an increase is quite worthwhile for practical applications even if smaller than the expected one (57%). Williams et al. [9] obtained the same increase (about 15%) using the SMA in parallel with steel wire. The stiffness of wires in parallel is the sum of each stiffness. The stiffness of the steel cannot be modified and, moreover, is bigger than that of the SMA. Thus steel wires allow there to be a higher base natural frequency, but limit the tuning range. Even if the test rig described in the report shows a poor performance of SMA, it is a very simple design and fully exploits the performance of the material.

5.3. Steady state tests

The second phase of experimental characterization of the SMA test rig was to evaluate the relationship between temperature and tuning frequency of the TVA. As it is easier to control the current through the SMA, that introduces heat to the system, several measurements were made at different current levels, always allowing the system to reach the steady state temperature first.

The first tests involved heating the SMA TVA. These tests are shown in Table 23. It was very difficult to estimate the final temperature accurately, particularly during the phase transition, because of fluctuation on the recorded temperatures measured using the thermocouple. Table 24 gives various data of the SMA test rig.

Plotting the measured impedances (see Figure 45), the change of the tuning frequency is clearly evident. Figure 46 shows the variation of the impedance with frequency as a function of temperature, and Figure 47 shows the same as a function of current. The maximum and minimum impedances are clearly evident. From these tests also the

transition temperatures could be inferred. We can infer that A_s is about 45°C and A_f about 60°C. These temperatures seem to correspond to currents of 5A and 6.5A respectively under the measurement conditions obtaining.

During the experimental tests the temperature of the SMA was also measured so that the thermal behaviour of the test rig could be inferred. For example, the convective coefficient α is shown in Figure 48. It is clear that the average value of the convective coefficient is about 40 W/m^{2}K. This is larger than the value obtained for the brass wire. This is probably due to the fact that here the value is estimated on the vibrating structure. So this value is more useful because it is the value for the equipment in the working conditions.

Similar tests were carried out when the SMA TVA was cooling. These tests are listed in Table 25. During this experiment the measured temperature fluctuation was larger below 42°C and the coherence in such a range was not so good.

Plotting all the impedance FRF obtained (see Figure 49) the change in the tuning frequency as in the previous test is evident. Figure 50 shows the variation of the impedance peak and trough versus temperature, and Figure 51 the same variation versus current. Note that during cooling there is an extra shift in the properties of the SMA for which there is no explanation currently.

It is evident that there is an hysteresis of about 10°C because the transition is between 30°C and 50°C. So we can infer that M_s is about 50°C and M_f about 35°C. These temperatures correspond to currents of about 5.5A and 3.5A respectively. It is noteworthy that the company do not give any information about the hysteresis of the SMA wire.

The results of the thermal characterization of the convective coefficient are plotted in Figure 52. The value of the convective coefficient is about 40 W/m^{2}K only above the transition temperature and it becomes smaller up to 25 W/m^{2}K below 50°C. This behaviour is strange because it does not correspond to the behaviour during heating. Perhaps a superelastic dissipation of energy contributes to the dissipation of energy from the wire.

5.4. Continuous tests

Two transient tests were carried out in order to evaluate the time that the phase transformation takes. Table 26 gives the parameters for these two experiments. Figure 53 shows the result of the first experiment in which the SMA wire was heated from

25°C to 78°C during the 240 seconds of acquisition. Figure 54 shows the result of the cooling of the wire from 72°C to 27°C. The ambient temperature was about 12°C and the current was 9.5A. Figure 55 shows the same results in a different way.

In order to evaluate the frequency response the H_1 estimator has been utilized (implemented by the function `tfe` in Matlab). H_1 is a transfer function estimate that links the input signal f (force signal) to the output signal vector x (response signal). Such a estimate is the quotient of the cross spectrum of f and x and the power spectrum of f:

$$\hat{H}_1(f) = \frac{\hat{S}_{fx}(f)}{\hat{S}_{ff}(f)}. \tag{32}$$

It is well-known that this estimate is better at the antiresonance where primarily the response signal suffers from noise.

From the analysis of the results, we conclude that the system takes about 120 seconds to pass from the cold state to the hot state and about 80 seconds to pass from the hot to the cold state. The fact that the state of cooling is quicker can be attributed to effective convective dissipation.

Notwithstanding the very good results, unusual behaviour is noticed in Figure 54 when the cold state is almost completely reached, i.e. a kind of "over-cooling" appears. Maybe there is an end effect during the cooling down and the heating up in that the part of the wire far from the free ends reaches the final temperature later. So the total system is constituted by two wires in series of martensite and austenite phases during the transient. Considering that the stiffness of two wires in series is the reciprocal of the sum of the reciprocals of the individual stiffnesses, and that the stiffness is inversely proportional to the cube of the length of the beam, this phenomenon slows down the change in the total stiffness at the beginning. Maybe during this moment the wire is expanding and the stiffness decreases for this reason. Afterwards the Young modulus increases and the total stiffness increases again.

The final series of experimental tests was carried out to investigate the influence of the hysteresis on the response time. In order to implement a continuously tunable SMA TVA, it will involve a mixture of martensite and austenite phases, and there will be hysteresis in the consequent phase transformation. Typically there would be a martensite fraction of 0.5 approximately so that the stiffness of the TVA could be increased or decreased as necessary.

Figure 56 shows the response of the SMA TVA under varying transient heating conditions. The left-hand figures show the behaviour as the TVA is heated to a temperature between A_s and A_f and then cooled down again to the ambient temperature. The right-hand figures show the behaviour when the SMA TVA is cooled down to a temperature between M_s and M_f and then heated up again to the steady hot state. The encouraging result is that no hysteresis effects are visible, so that the hysteresis seems to be a phenomenon whose time constants are an order of magnitude less then the time constants of heating or cooling the wire.

5.5. Summary

The thermo-mechanical characteristic of a TVA built up with a SMA wire has been investigated. The tuning frequency of such a device can change by about 15% passing from the cold to the hot state of the SMA wire. This good result is due to a change in the Young's modulus by about 47.5%, although, according to the company, it should be about 175%. Even if SMA has strong nonlinear behaviour and showed a strange "extra-cooling" effect, not recorded before from other researchers, its use is advisable. In fact the SMA TVA is mechanically very simple, cheap and the electrical supply is easily available.

In order to use the device in practical application a controller is needed. The controller should compensate for the non-linearities of the SMA and tune the TVA to the excitation frequency. The next section deals with the control of a TVA and in particular an SMA TVA.

Figures

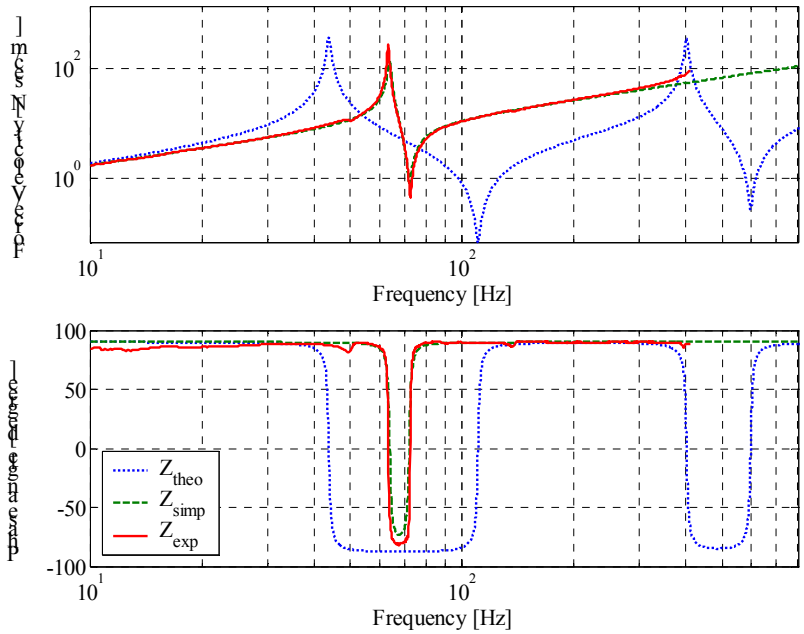

Figure 34 Comparison between calculated and experimental FRF impedance (cold state):
—— measured; · · · · beam model; - - - - 2 dof approximation

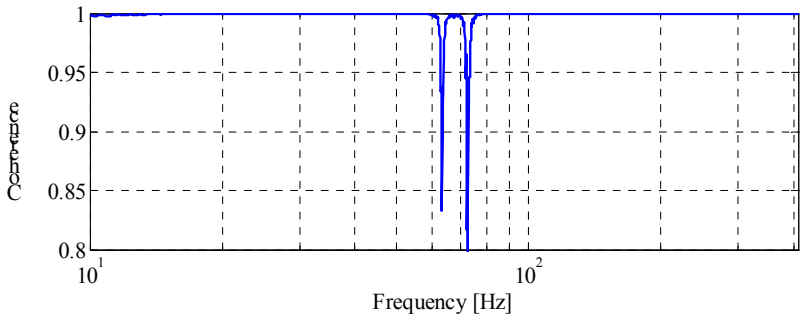

Figure 35 Coherence of the experience - cold state

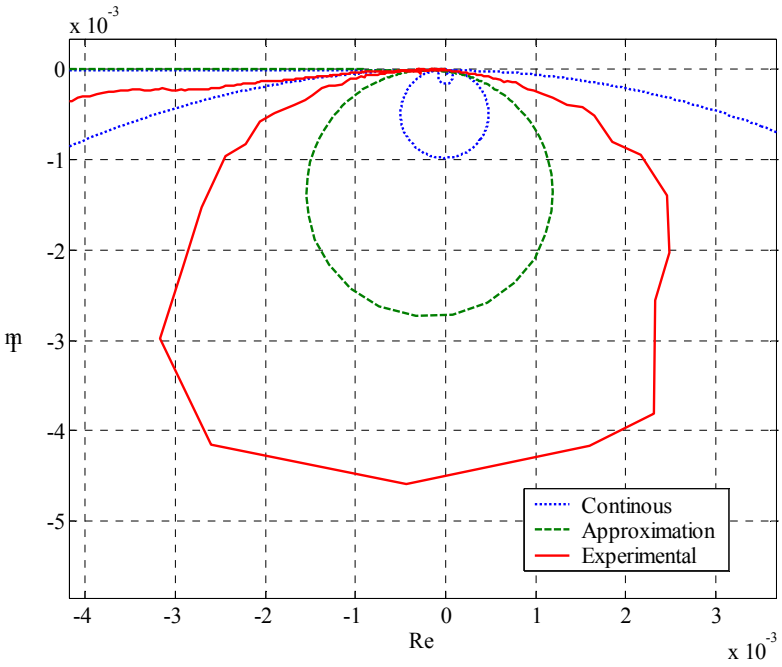

Figure 36 Polar plot of receptance (cold state):

—— measured; · · · · beam model; - - - - 2 dof approximation

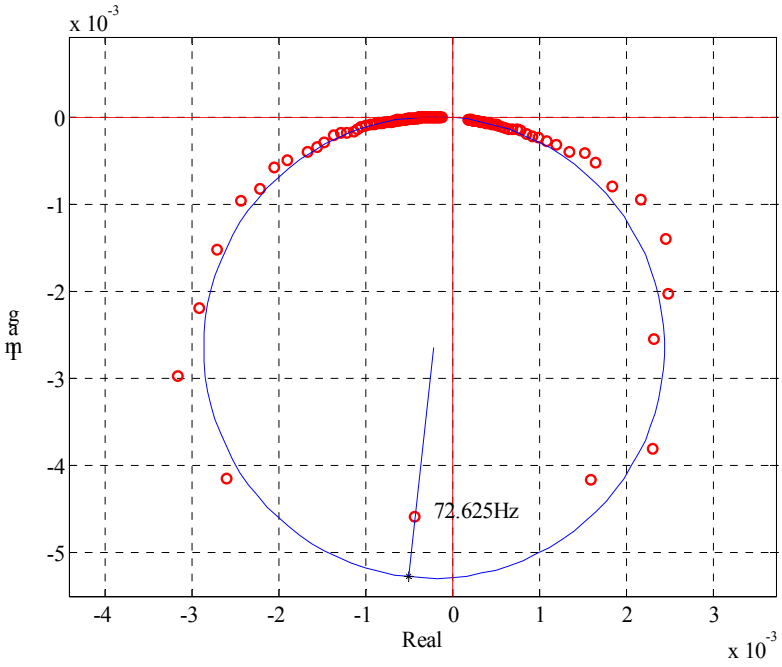

Figure 37 Circle fitting on the experimental receptance points; cold state

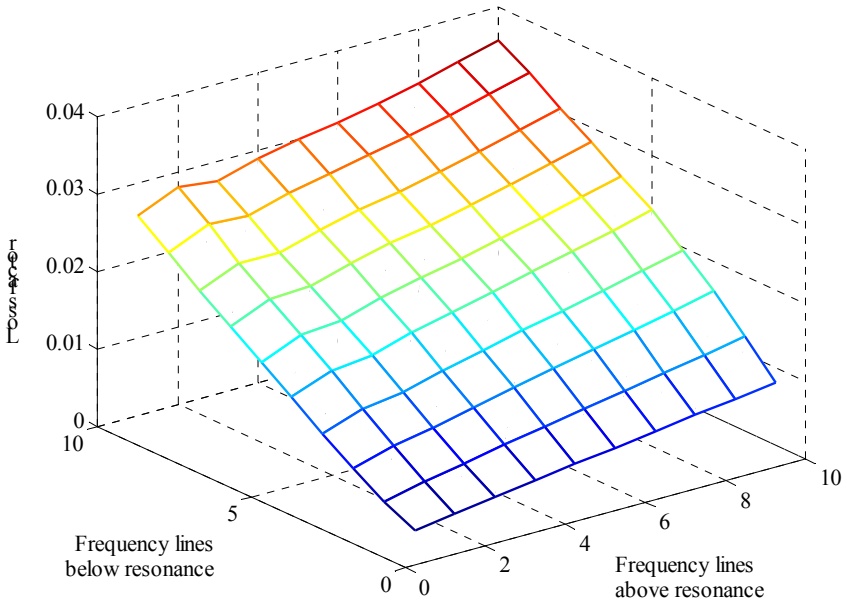

Figure 38 Carpet plot of the estimated loss factor; cold state

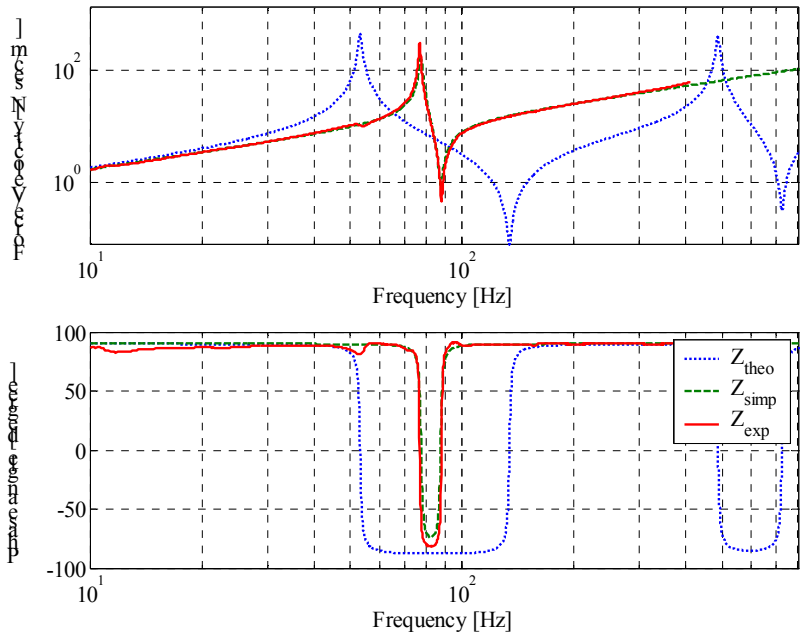

Figure 39 Comparison between calculated and experimental FRF impedance (hot state):

—— measured; · · · · beam model; - - - - 2 dof approximation

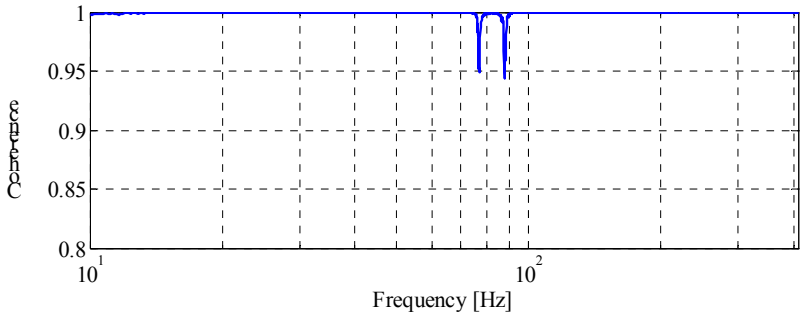

Figure 40 Coherence of the experience (hot state)

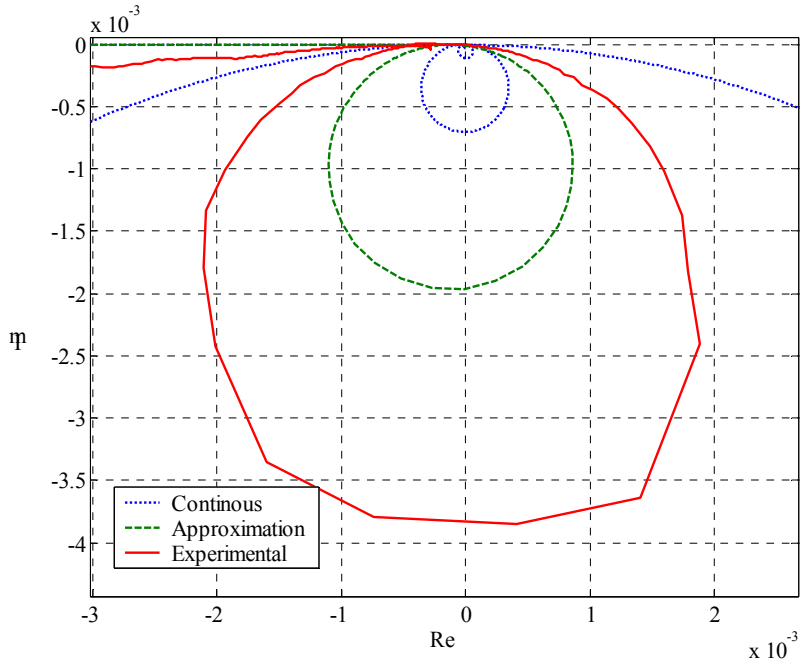

Figure 41 Nyquist plot of receptance (hot state):

—— measured; · · · · beam model; - - - - 2 dof approximation

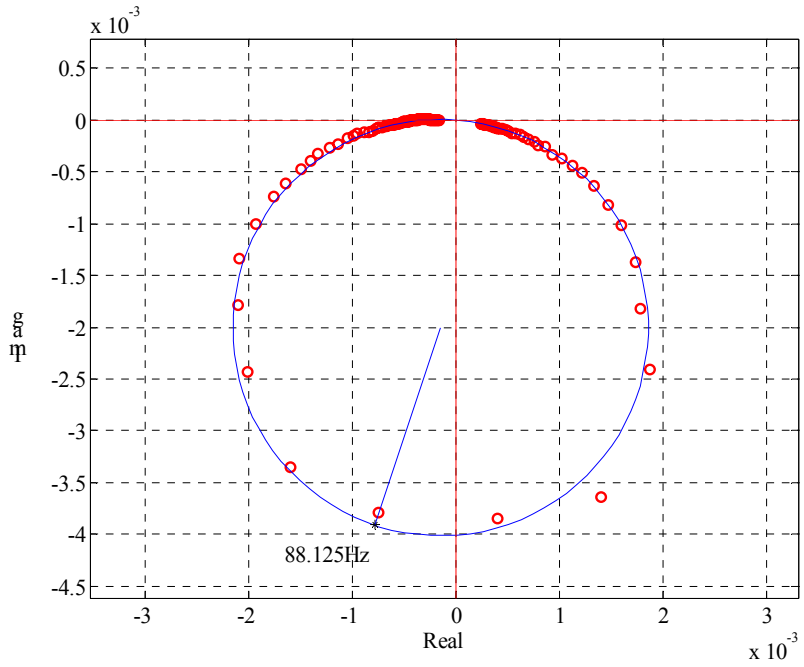

Figure 42 Circle fitting on the experimental receptance points; hot state

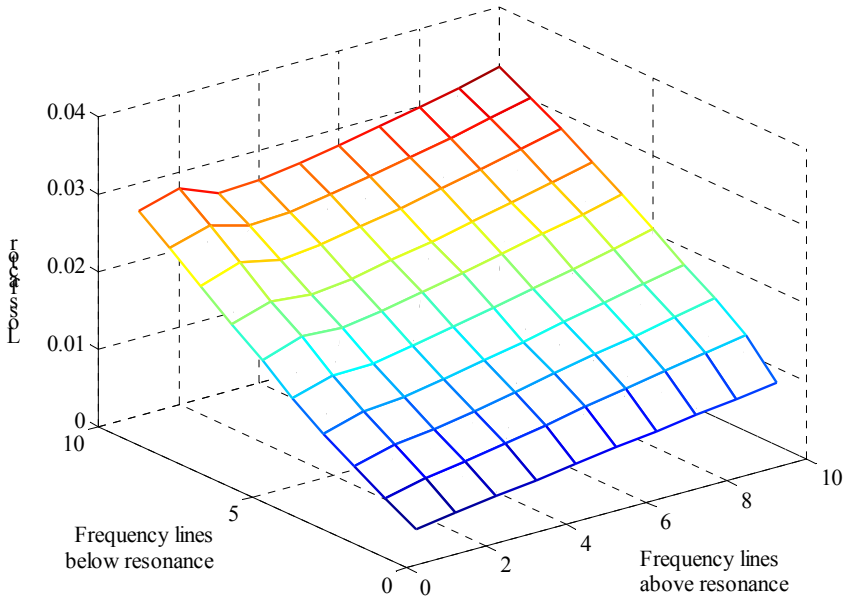

Figure 43 Carpet plot of the estimated loss factor; hot state

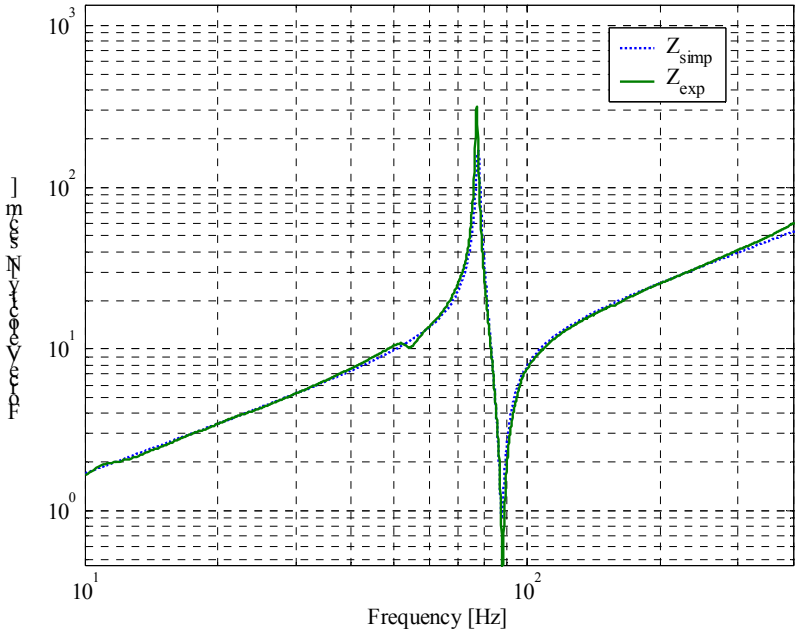

Figure 44 Fitting of the two dofs simplified system to the experimental data when the Young modulus of the austenite is set at 59 MPa

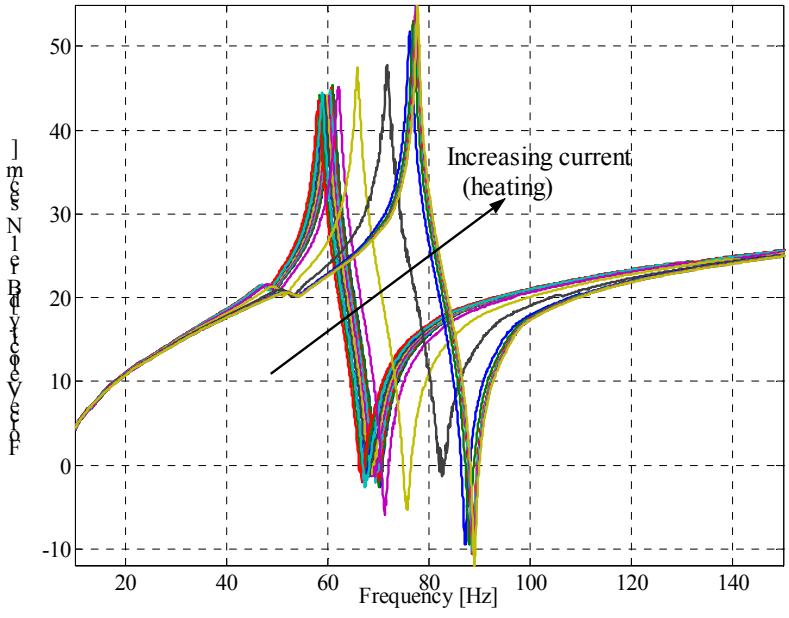

Figure 45 Variation of the impedance FRF during heating of the TVA

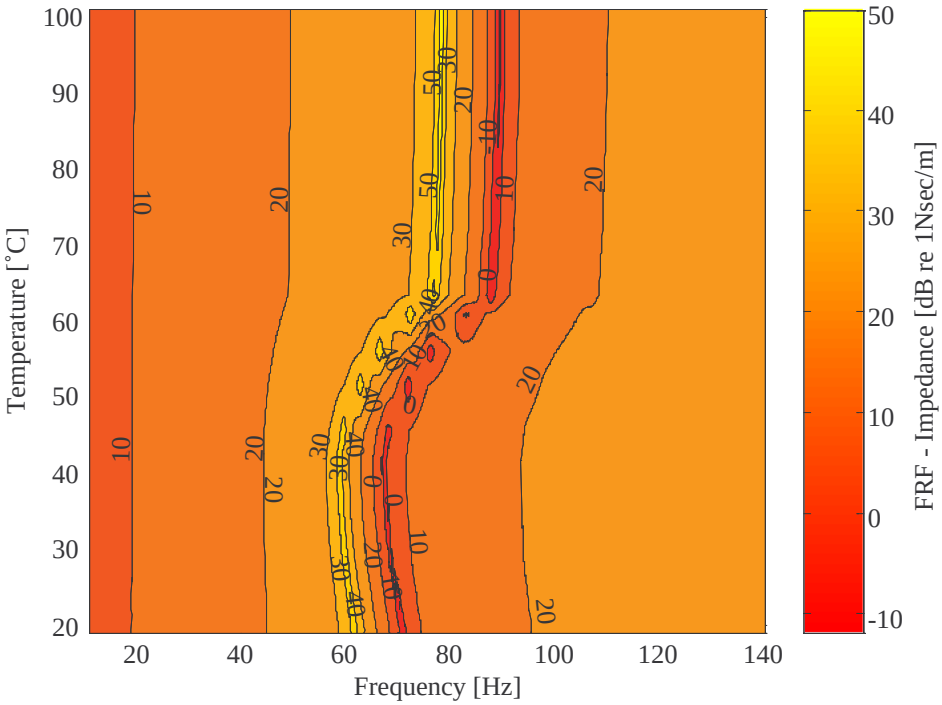

Figure 46 Variation of the FRF impedance versus temperature during heating

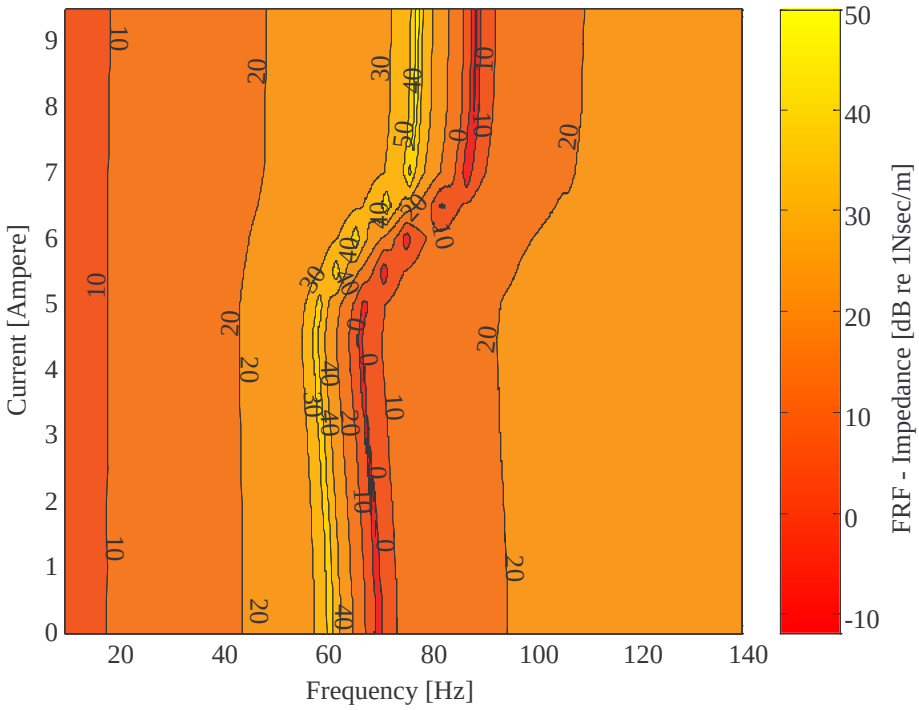

Figure 47 Variation of the FRF impedance versus current during heating

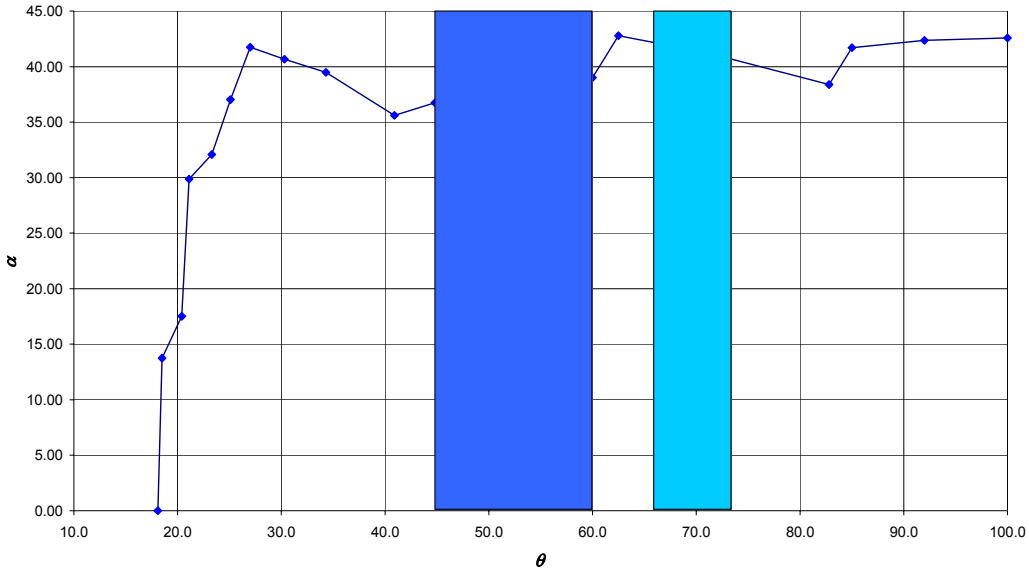

Figure 48 Convective coefficient versus temperature during heating
(right marked zone is the zone of transition declared by the SMA supply company, left marked zone is the zone inferred from the measurements)

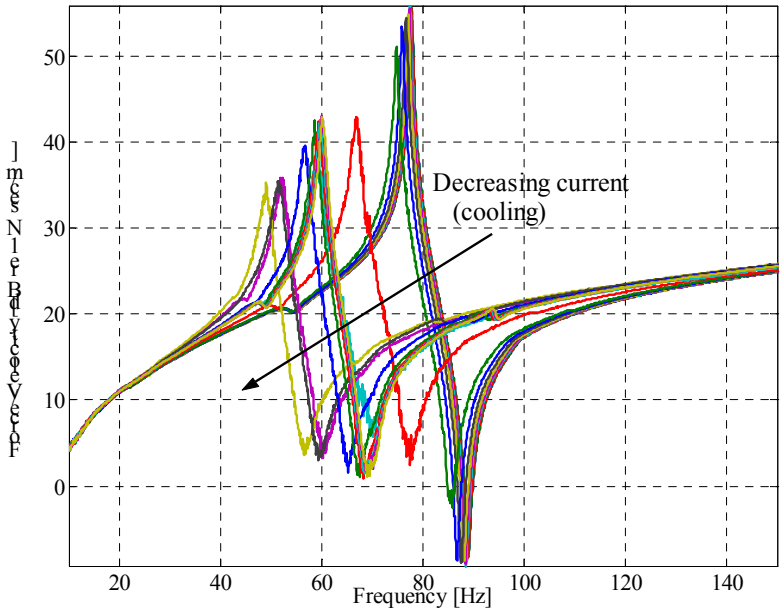

Figure 49 Variation of the FRF impedance during the cooling of the TVA

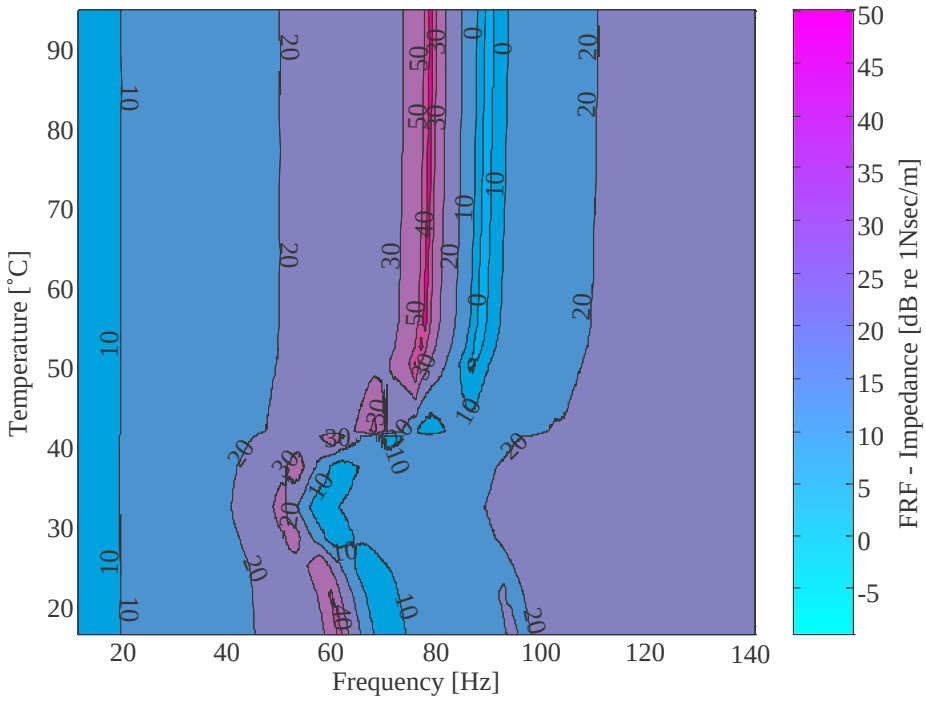

Figure 50 Variation of the FRF impedance versus temperature during cooling

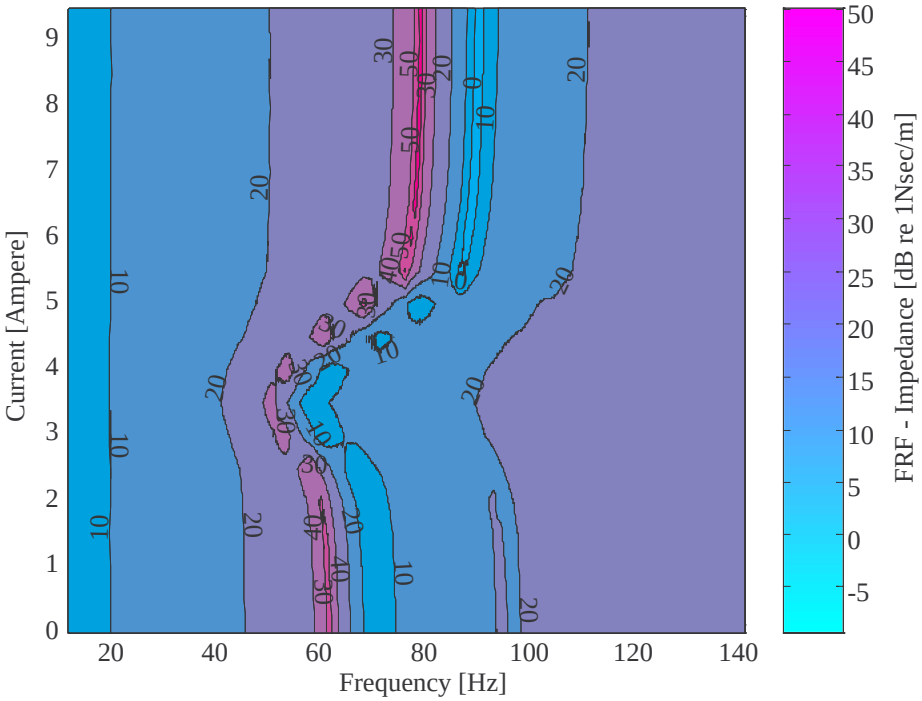

Figure 51 Variation of the FRF impedance versus current during cooling

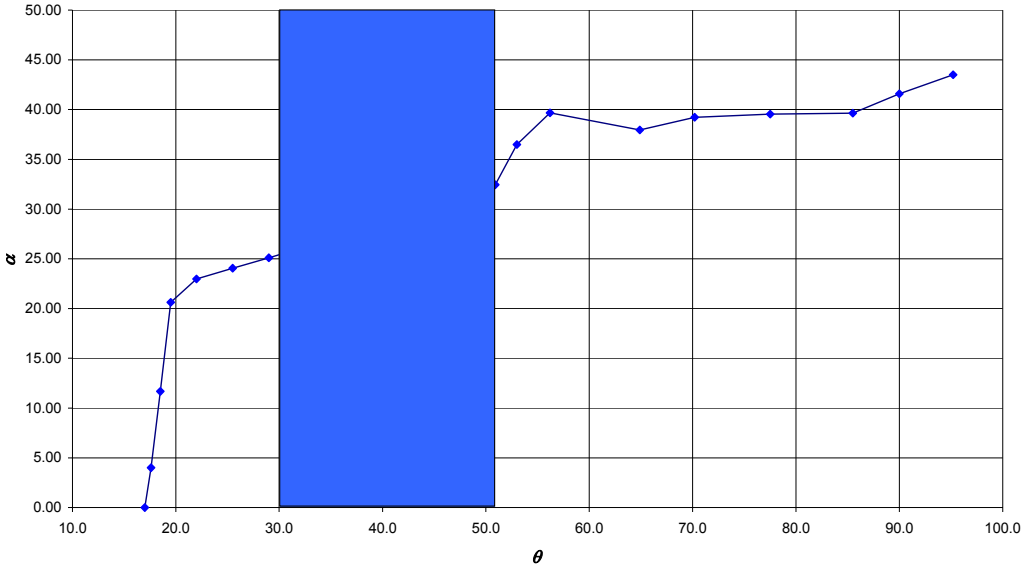

Figure 52 Convective coefficient versus temperature during cooling (violet zone is the zone of the measured transition)

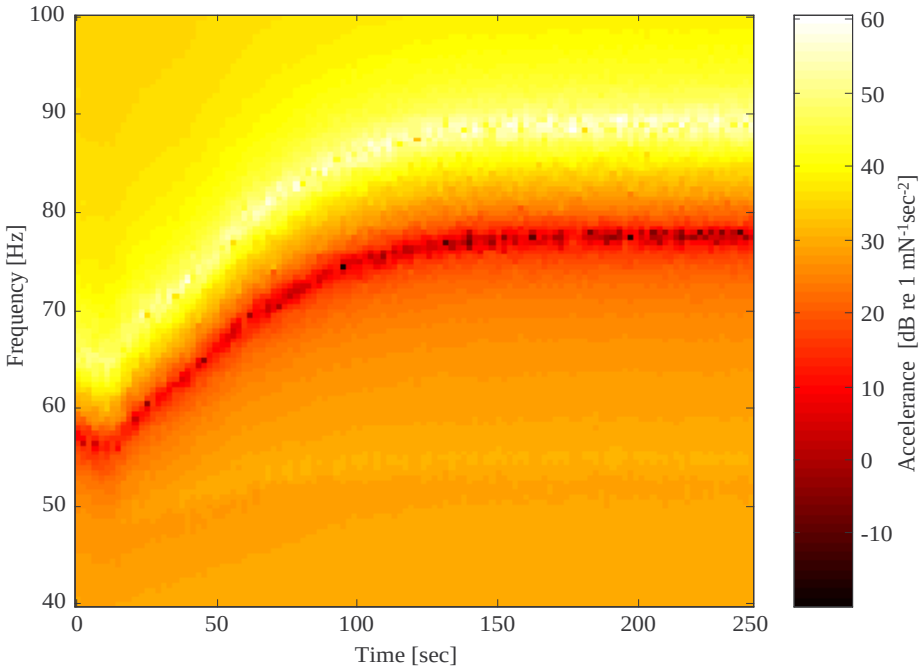

Figure 53 Variation of the accelerance versus time during heating

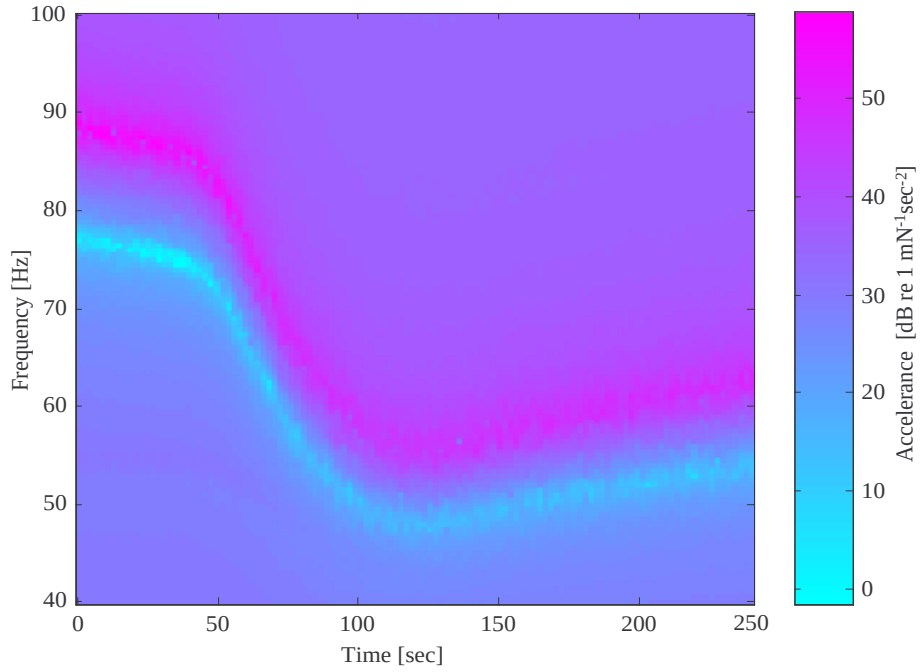

Figure 54 Variation of the accelerance versus time during cooling

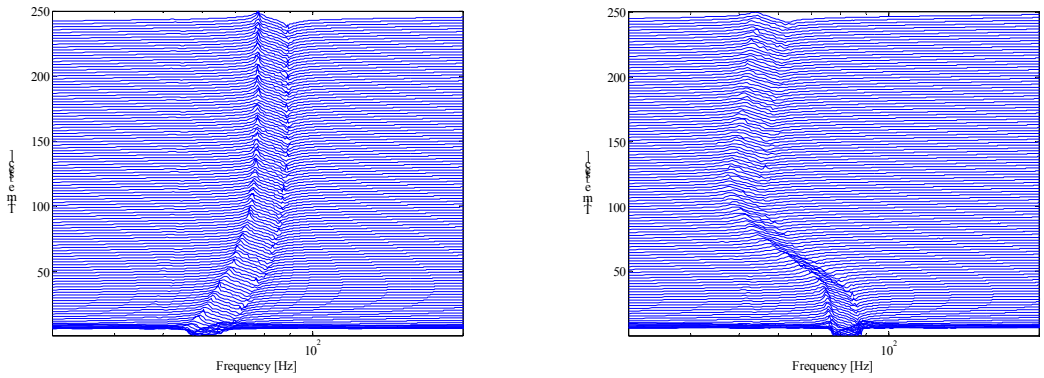

(a) **(b)**

Figure 55 Variation of impedance with time; (a) heating up and (b) cooling down

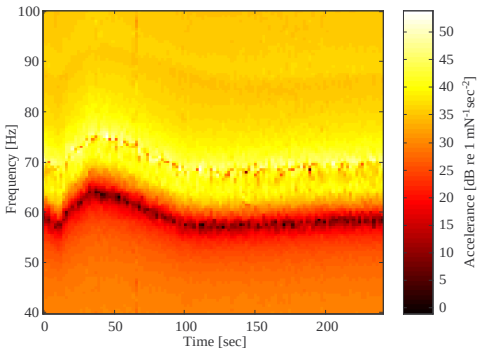

θ_1=~20°C - θ_2=47°C

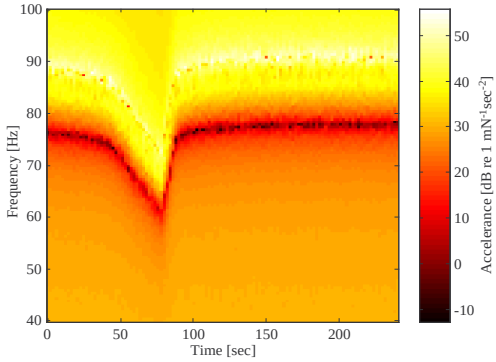

θ_1=~70°C - θ_2=44°C

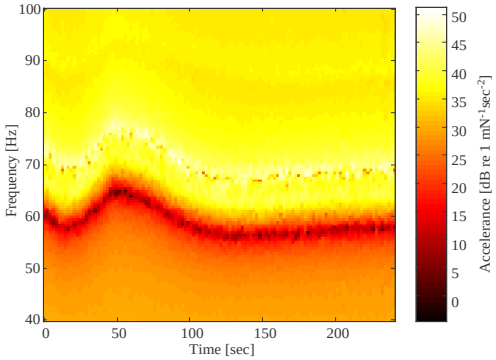

θ_1=~20°C - θ_2=51°C

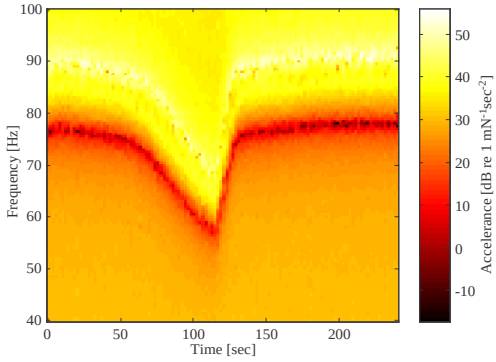

θ_1=~70°C - θ_2=41°C

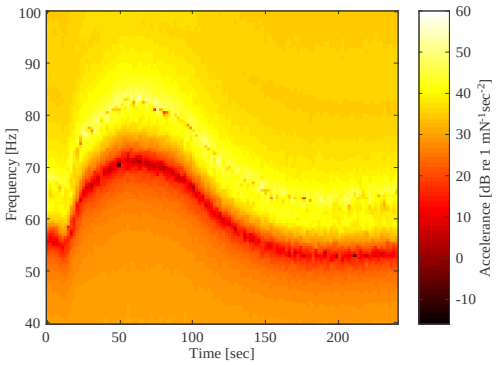

θ_1=~20°C - θ_2=54°C

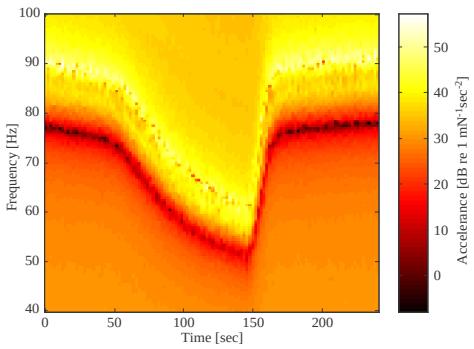

θ_1=~70°C - θ_2=37°C

Figure 56 Transient variations of the FRF accelerance versus the time: for each figure are indicated the start (θ_1) and switch (θ_2) temperature of the wire; the ambient temperature was about 17°C

Tables

Temperature of the wire	θ_w	19.5 °C
Ambient temperature	θ_a	17.4 °C
Current	I	0 A

Table 18 Setting of the first test (cold state)

Natural frequency ω_r:	72.65 Hz
Loss factor η:	0.018219
${}_rA_{jk}$:	20.019-i 2.238
${}_rB_{jk}$:	(8.047-i 0.619)·10^{-5}

Table 19 Results of the circle fitting on the cold SMA TVA

Temperature of the wire	θ_w	81.7 °C
Ambient temperature	θ_a	19.3 °C
Current	I	8.2 A

Table 20 Setting of the second test (hot state)

Natural frequency ω_r:	88.125 Hz
Loss factor η:	0.01703
${}_rA_{jk}$:	19.899-i 6.629
${}_rB_{jk}$:	(4.856-i 1.010)·10^{-4}

Table 21 Results of the circle fitting on the hot SMA TVA

	m_1	m_2	k	f_a	f_r
COLD STATE	0.0213 kg	0.0059 kg	946.2 N/m	63.9 Hz	72.2 Hz
HOT STATE	0.0213 kg	0.0059 kg	1395.7 N/m	77.6 Hz	87.6 Hz

Table 22 SMA TVA inferred properties (simplified 2 dof system)

Test	File	Wire temperature	Ambient temperature	Current	Tension	Temperature difference	Convective coefficient
n°	name	θ_w [°C]	θ_a [°C]	I [A]	U [V]	$\Delta\theta$ [K]	α [W/m^{2}K]
1	sma00_01.dat	18.1	17.6	0.0	0.0	0.5	0.00
2	sma00_02.dat	18.5	17.8	0.5	0.2	0.7	13.75
3	sma00_03.dat	20.4	18.2	1.0	0.4	2.2	17.50
4	sma00_04.dat	21.1	18.2	1.5	0.4	2.9	29.87
5	sma00_05.dat	23.3	18.5	2.0	0.5	4.8	32.09
6	sma00_06.dat	25.1	18.6	2.5	0.6	6.5	37.02
7	sma00_07.dat	27.0	18.7	3.0	0.7	8.3	41.75
8	sma00_08.dat	30.3	18.7	3.5	0.8	11.6	40.66
9	sma00_09.dat	34.3	18.7	4.0	0.9	15.6	39.49
10	sma00_10.dat	40.9	19.0	4.5	1.0	21.9	35.60
11	sma00_11.dat	44.8	18.6	5.0	1.1	26.2	36.74
12	sma00_12.dat	50.7	18.4	5.5	1.2	32.3	36.06
13	sma00_13.dat	55.1	18.5	6.0	1.3	36.6	37.87
14	sma00_14.dat	60.0	18.3	6.5	1.4	41.7	39.01
15	sma00_15.dat	62.5	18.4	7.0	1.5	44.1	42.78
16	sma00_16.dat	71.0	18.5	7.5	1.6	52.5	41.25
17	sma00_17.dat	82.8	18.6	8.0	1.7	64.2	38.38
18	sma00_18.dat	85.0	18.3	8.5	1.8	66.7	41.71
19	sma00_19.dat	92.0	18.4	9.0	1.9	73.6	42.37
20	sma00_20.dat	100.0	18.4	9.5	2.0	81.6	42.58

Table 23 SMA heating steady state tests

Diameter	d	0.002 m
Length	L	0.440 m
Area of heat exchange	A_e	0.002764602 m^2
Resistivity	ρ_e	7.60E-07 Ωm
Resistance	R	0.106442826 Ω

Table 24 Main data of the test rig

Test	File	Wire temperature	Ambient temperature	Current	Tension	Temperature difference	Convective coefficient
n°	name	θ_w [°C]	θ_a [°C]	I [A]	U [V]	$\Delta\theta$ [K]	α [W/m^{2}K]
1	sma01_01.dat	95.2	15.3	9.5	0.0	79.9	43.49
2	sma01_02.dat	90.0	15.0	9.0	0.2	75.0	41.58
3	sma01_03.dat	85.5	15.3	8.5	0.4	70.2	39.63
4	sma01_04.dat	77.5	15.2	8.0	0.4	62.3	39.55
5	sma01_05.dat	70.2	15.0	7.5	0.5	55.2	39.23
6	sma01_06.dat	64.9	15.2	7.0	0.6	49.7	37.96
7	sma01_07.dat	56.2	15.2	6.5	0.7	41.0	39.68
8	sma01_08.dat	53.0	15.0	6.0	0.8	38.0	36.48
9	sma01_09.dat	50.9	15.0	5.5	0.9	35.9	32.44
10	sma01_10.dat	42.5	15.1	5.0	1.0	27.4	35.13
11	sma00_11.dat	41.8	15.2	4.5	1.1	26.6	29.31
12	sma01_12.dat	38.0	15.1	4.0	1.2	22.9	26.90
13	sma01_13.dat	33.0	15.1	3.5	1.3	17.9	26.35
14	sma01_14.dat	29.0	15.2	3.0	1.4	13.8	25.11
15	sma01_15.dat	25.5	15.5	2.5	1.5	10.0	24.06
16	sma01_16.dat	22.0	15.3	2.0	1.6	6.7	22.99
17	sma01_17.dat	19.5	15.3	1.5	1.7	4.2	20.63
18	sma01_18.dat	18.5	15.2	1.0	1.8	3.3	11.67
19	sma01_19.dat	17.6	15.2	0.5	1.9	2.4	4.01
20	sma01_20.dat	17.0	15.0	0.0	2.0	2.0	0.00

Table 25 Steady state tests during cooling

Acquired time:	240 sec.
Scan frequency:	512 Hz
Current:	9.5A
Heating up:	from 25°C to 78°C
Cooling down:	from 72°C to 27°C
Ambient temperature:	about 12°C
H_1 evaluation:	`[frf,f]=tfe(C1(i:j),C2(i:j),1024,fs,512,100);`

Table 26 Settings of the transient experimental tests

6. Control technique

6.1. Introduction

This section concerns the problems that the SMA TVA controller design presents. First a dynamical model of a generic TVA has been studied and implemented in Simulink®. Then different control techniques have been taken in to account and their efficiency has been compared using a performance index. The robustness of such controllers has been tested by simulating noise disturbances. Finally the control of the SMA TVA has been attempted.

6.2. Numerical simulation of a TVA

A Simulink® model of the TVA (see Figure 1) a system comprising the host machine mass and the dynamic vibration absorber has been constructed. The equations of motion of the two masses are

$$\begin{aligned} m_1\ddot{x}_1 + c_2(\dot{x}_1 - \dot{x}_2) + k_2(x_1 - x_2) &= f_1 \\ m_2\ddot{x}_2 + c_2(\dot{x}_2 - \dot{x}_1) + k_2(x_2 - x_1) &= f_2 \end{aligned} \tag{33a,b}$$

Thus the accelerations of the masses are given by

$$\begin{aligned} \ddot{x}_1 &= \frac{f_1}{m_1} - \frac{c_2(\dot{x}_1 - \dot{x}_2)}{m_1} - \frac{k_2(x_1 - x_2)}{m_1} \\ \ddot{x}_2 &= \frac{f_2}{m_2} - \frac{c_2(\dot{x}_2 - \dot{x}_1)}{m_2} - \frac{k_2(x_2 - x_1)}{m_2} \end{aligned} \tag{34a,b}$$

The force f_2 acting on the absorber mass is zero. The Simulink® model of the system is shown in Figure 57.

In the time domain it is not possible to use hysteretic damping, so viscous damping has been used with a viscous damping coefficient given by

$$c_2 = \eta m_2 \omega_a = \frac{\eta k_2}{\omega_a} \tag{35}$$

Such a coefficient has been calculated by equating the dissipated powers for excitation at the resonance frequency (i.e. $\omega=\omega_a$) because that is the normal working frequency for a properly tuned TVA. Table 27 shows the values of the system constants used for the tests carried out.

6.3. Tuning strategy

The velocities of the main system and the neutraliser masses for discrete frequency motion can be expressed by

$$\begin{aligned} \dot{x}_1(t) &= \left|\dot{X}_1\right| \cos \omega t \\ \dot{x}_2(t) &= \left|\dot{X}_2\right| \cos(\omega t - \phi) \end{aligned} \tag{36a,b}$$

The time averaged product of the velocities over one cycle of period T can be written as

$$\overline{\dot{x}_1 \dot{x}_2} = \frac{1}{T} \int_0^T \dot{x}_1 \dot{x}_2 \mathrm{d}t = \frac{\left|\dot{X}_1\right|\left|\dot{X}_2\right|}{2} \cos \phi \tag{37}$$

Thus the time averaged product of the velocities of the machine and TVA masses is proportional to the phase between the velocities. In section 2 it was seen that, when the TVA is tuned, the velocities are in quadrature, so their time averaged product is zero and thus cos(ϕ) is zero. Therefore this signal can be used as an error signal in a control system (see Figure 58). For example, a steepest descent method seeks an operating point where $\overline{\dot{x}_1 \dot{x}_2} = 0$ could be implemented.

In practise it is more convenient to consider the normalized time averaged product

$$\mathrm{norm}\left(\overline{\dot{x}_1 \dot{x}_2}\right) = 2 \frac{\overline{\dot{x}_1 \dot{x}_2}}{\left|\dot{X}_1\right|\left|\dot{X}_2\right|} = \cos \phi \tag{38}$$

so that the error lies between -1 and 1 and does not depend on the amplitudes of the motion.

It should be noted that this tuning is not optimal. It coincides with the optimum only when η=0, but is a very good approximation for small damping (see [2]).

6.4. Numerical implementation of adaptive controls

A comparison of different control systems is carried out in order to find the adaptive control technique most suitable to tune a TVA. During this preliminary analysis an ideal TVA, with no delay in the actuation response, was considered. Later the same adaptive control techniques were applied to a model of an SMA TVA.

The same excitation signal was used to evaluate the various control algorithms. The excitation frequency was sinusoidal with a frequency that varied linearly from 75 Hz to 150Hz, from t=5 to t=15 (see Figure 59). The simulations were run for 20 sec. The Simulink® block that generates the excitation frequency was realized using the equations taken from [1]. Figure 60 shows the phase angle between the velocities of the

machine and oscillator masses, cos(ϕ), and the velocity of the host mass, V_1 when such an excitation force is imposed. No adaptation was involved with the absorber being tuned to 82.3 Hz (see Table 27). The function cos(ϕ) was estimated using equation 37, by integrating over a fixed period of 0.1 sec.

As can be seen above, cos(ϕ) (given by equation 38) can be used as an error signal, i.e. at the n-th time step in a discrete control system the error signal is

$$e_n = \cos\hat{\phi} \tag{39}$$

where $\cos\hat{\phi}$ is an estimate for the time average of equation 38.

Supposing that the stiffness of the TVA is to be updated every T_c second. A simple linear method of adapting the stiffness is given by

$$k_{n+1} = k_n - Pe_n \tag{40}$$

where P is the proportional control constant. The period T_c between updates of the stiffness is set to 0.1 sec for all the tests. The error at the n-th time step is estimated using equation 37 integrating over the period of control T_c.

Because the variation of the stiffness versus cos(ϕ) is highly non-linear, there is no reason to use just a simple proportional method. Following the classical control theory a PID controller, with a proportional control constant P, a derivative control constant D and a integral control I, could be used so that

$$k_{n+1} = k_n - \left(Pe_n + Ii_n + Dd_n\right) \tag{41}$$

where i_n is the integral of the error and is given by

$$i_n = i_{n-1} + e_n \tag{42}$$

and d_n is the derivative of the error given by

$$d_n = \frac{e_n - e_{n-2}}{2T_c} \tag{43}$$

It might be preferable to use a non-linear updating algorithm since the system is non-linear. For example to try to follow this non linearity, a polynomial function that update the stiffness in a non linear way, given for instance by

$$k_{n+1} = k_n - P\left(e_n + e_n^3 + e_n^5\right) \tag{44}$$

could be used. A similar non linear function could also been obtained using fuzzy logic (see [7]).

In order to compare the performances of several control systems a performance index is needed. One such index is the integral of the absolute value of the error, *IAE*, given by

$$IAE = \int_{o}^{\infty} |e(t)| \mathrm{d}t \tag{45}$$

There are other indices, and for vibration control purposes, the time required for the system to tune within some limit of its optimal value is another possibility.

Figure 61 shows the Simulink® model. The "control" block is changed to implement the chosen control algorithm. Each control block is formed from other sub-blocks. The first evaluates the average of $\dot{x}_1\dot{x}_2$, $\left|\dot{X}_1\right|$ and $\left|\dot{X}_2\right|$ over each control period T_c. Such quantities are needed in order to evaluate the error, e_n, and to change the stiffness. Figure 62 shows this subsystem. In order to evaluate $\left|\dot{X}_1\right|$ and $\left|\dot{X}_2\right|$ it is noted that the amplitude of a function $f(t) = A\sin\omega t$ is given by

$$A = \frac{\pi}{2T_c}\int_{0}^{T_c} |f(t)| \mathrm{d}t \tag{46}$$

in which T_c is a multiple of the period $2\pi/\omega$.

The second subsystem implements the control algorithm. After the evaluation of the error e_n, the stiffness is updated. Figure 63 shows the control subsystem for the polynomial of equation 45. Figure 64 and Figure 65 show the subsystems for the PID and fuzzy control systems respectively.

The performances of the various control algorithms are compared. In order to make realistic comparisons, the maximum change in the stiffness per adaptation was kept approximately the same. In the following figures the *IAE*, the stiffness *k*, the phase between the velocities, cos(ϕ), and the velocity of the machine mass, V_1, are shown as functions of time. Figure 66-68 show results for proportional, polynomial, fuzzy and PID controls respectively.

While PID control is central to classical control theory, here its performance is poor. The reason is that we are realizing adaptive control rather than classical feedback control. Fuzzy control shows the better *IAE*, but the performances of the three systems are very similar. Proportional control seems to reach optimal tuning somewhat quickly (compare cos(ϕ) of different control algorithms).

The main drawback of fuzzy control is that it is more complex to implement because it needs digital control, whereas the other two control algorithms are analogue and simpler. The use of fuzzy control is justified when there are many inputs. For implementations, a choice is made between the proportional and polynomial control.

The latter is somewhat preferable because it is more flexible control. More constants could be used for each term in the polynomial and so the updating function, k_n-k_{n+1}=$f(e_n)$, could take almost any form.

Next a continuous updating control was implemented, to verify its feasibility, assuming that the TVA has an immediate response. Figure 70 shows the Simulink® model for the polynomial control. In this case only $\overline{\dot{x}_1\dot{x}_2}$ is required since it is proportional to cos(ϕ)

$$\overline{\dot{x}_1\dot{x}_2} = Q\cos\phi$$

where Q is the constant of proportionality (see equation 37).

The integral of $\overline{\dot{x}_1\dot{x}_2}$ is evaluated every control period, of duration T_c=0.1 sec, but the stiffness is updated in real time. Figure 71 shows the results for polynomial control and Figure 72 for the fuzzy control. Once more the performance of the fuzzy control was somewhat better but not enough to justify its use.

Comparing Figure 67 to Figure 71 and Figure 68 to Figure 72 shows that the performance of the continuous control is better than that one of the discrete control.

6.5. Effect of noise on control

In order to verify the robustness of the adaptive control, simulations with noise added to the velocities signals were performed. The ratio between the amplitudes of the velocity of the machine mass, V_1, and of the noise, N, were 20, 10 and 5 dB.

Results with white noise added to the velocities of both the machine and the TVA masses, V_1 and V_2, are shown in Figure 73-75. Moreover, Figure 76-78 show the result for the continuous updating control. The continuous updating performance seems to be very robust whereas the discrete control has a poor performance. Generally the performance gets worse as the noise level increases, as would be expected.

6.6. Control of SMA TVA

A Simulink® model of a SMA TVA was implemented based on the analysis described in chapter 3. The block diagram is shown in Figure 79. Figure 80 shows the thermal subsystem model. The input to the subsystem is the current, I, and the output is the temperature of the wire, θ. The latent heat of transformation has been taken into account by using a different specific heat constant for $\theta \in \lfloor M_f ; A_f \rfloor$ (see equation 30). Figure 81 shows the constitutive model that relates the temperature of the SMA, θ, to the martensite ratio, ξ.

After the martensite ratio has been evaluated, the Young modulus is estimated by assuming that there is a linear relation between the martensite ratio and the Young modulus, given by

$$E = (E_m - E_a)\xi + E_a \tag{47}$$

Figure 82 shows the block diagram of the subsystem that estimates the Young modulus. The stiffness of the absorber spring is then given by

$$k_2 = \frac{EI}{\rho A}\frac{\chi_1^4}{L^4}\frac{m_1 m_2}{m_1 + m_2} \tag{48}$$

Control requires estimates of $\dot{x}_1\dot{x}_2$, $\left|\dot{X}_1\right|$ and $\left|\dot{X}_2\right|$ (see Figure 62). Here the current that flows through the SMA wire is updated, instead of the stiffness directly, with the updated current at the (i+1)th time step being given by

$$I_{i+1} = I_i - P\cos\phi(t) - D\frac{\mathrm{d}[\cos\phi(t)]}{\mathrm{d}t} \tag{49}$$

The control is PD control with the error being given by the phase between the velocities of the machine and resonator masses.

The system is updated every T_c=0.1 sec. In the first simulation there is a constant excitation frequency of 90Hz. Figure 84 shows the results for proportional control. It is evident that, even if the amplitude of the velocity of the machine mass is reduced, the current and cos(ϕ) fluctuate and do not reach a steady value. Figure 85 shows the result of PD control. The current reaches an almost constant steady value, while the error signal cos(ϕ)≈0, indicating that the SMA TVA is optimally tuned.

Next simulations were performed with frequency of excitation changing slowly from 90Hz to 80Hz (see Figure 86). Figure 87 shows the results for proportional control and Figure 88 for PD control. The implemented control seems to be effective but adapts very slowly.

6.7. Summary

A controller for a generic TVA has been designed. The simulations carried out have showed a good performance and robustness of the controller. Such a controller, with some little modifications, has been applied also to the SMA TVA model. It has shown good performance, even if reduced by the thermal characteristics of the SMA wire.

Figures

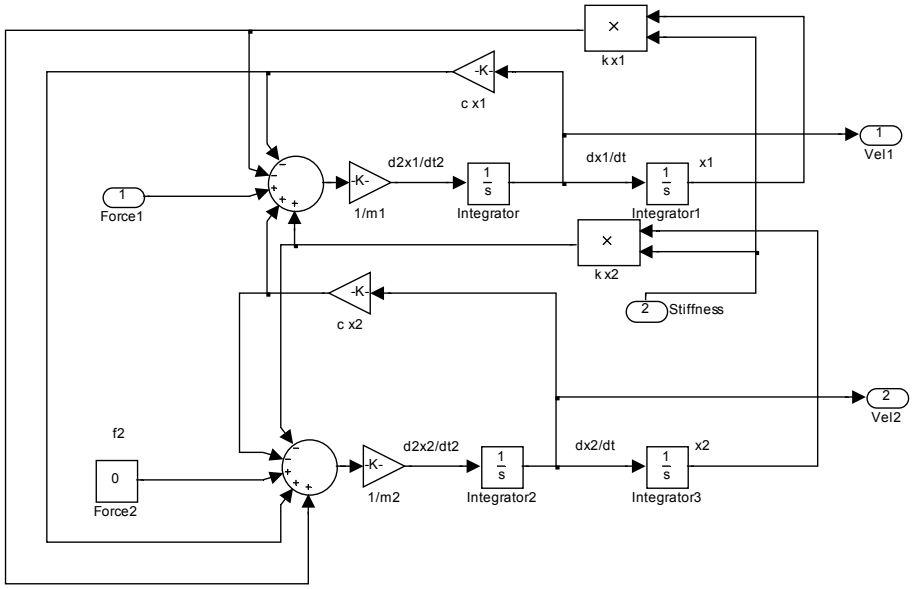

Figure 57 Model of a dynamic vibration absorber attached to a mass m_1

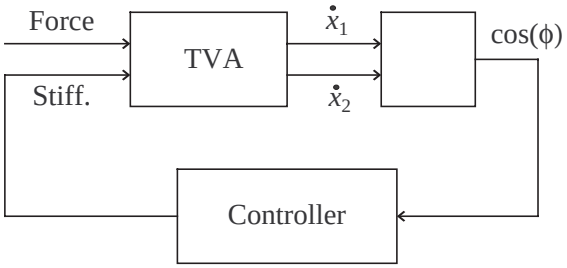

Figure 58 Block diagram of a controlled TVA

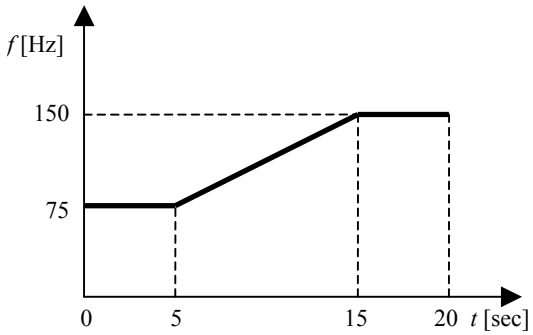

Figure 59 Frequency of the excitation force versus time

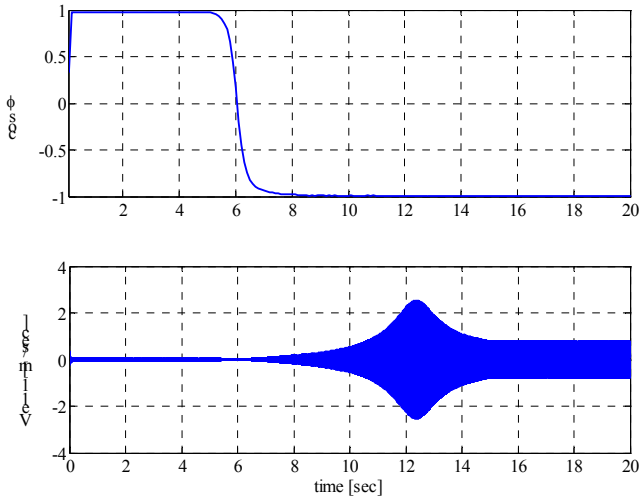

Figure 60 Response of the TVA system

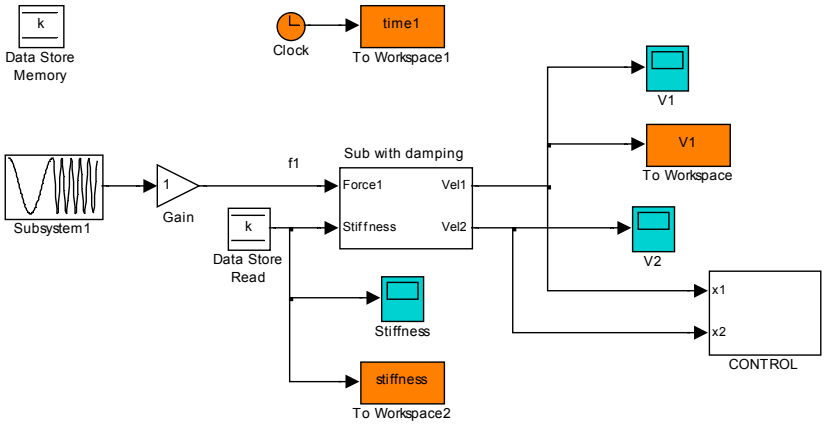

Figure 61 Simulink® general model

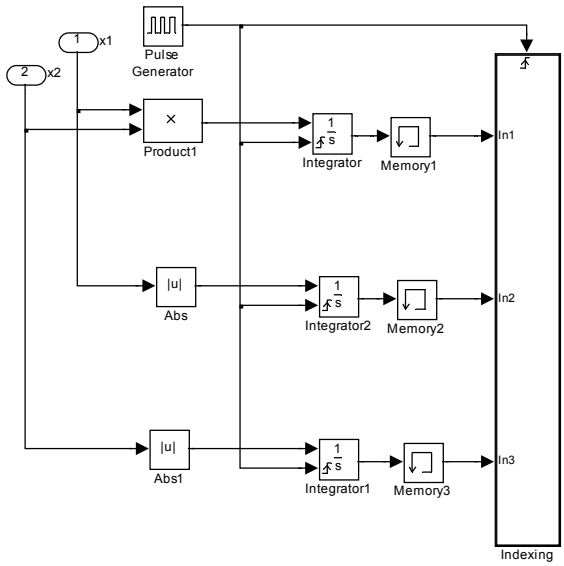

Figure 62 Evaluation of $\dot{x}_1\dot{x}_2$, $\left|\dot{X}_1\right|$ and $\left|\dot{X}_2\right|$ at each control step

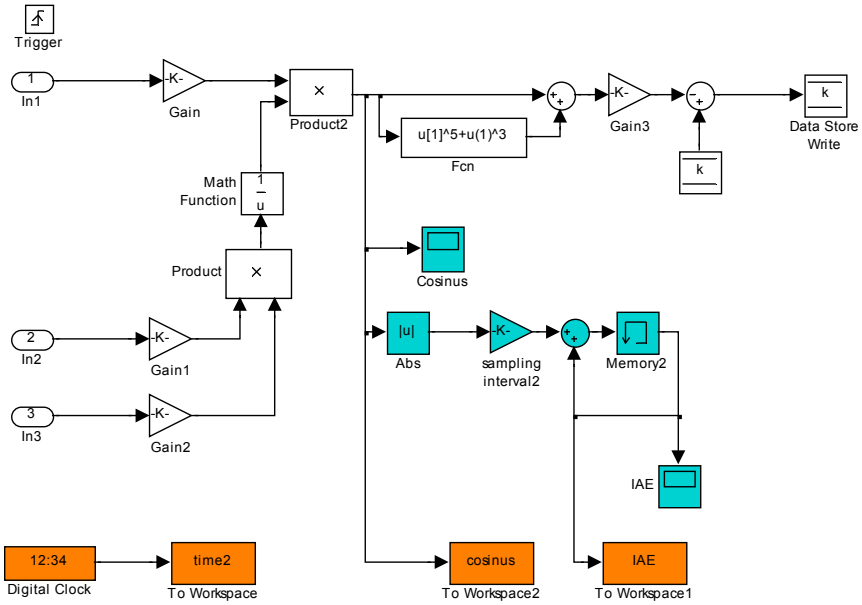

Figure 63 Simulink® subsystem for the polynomial control

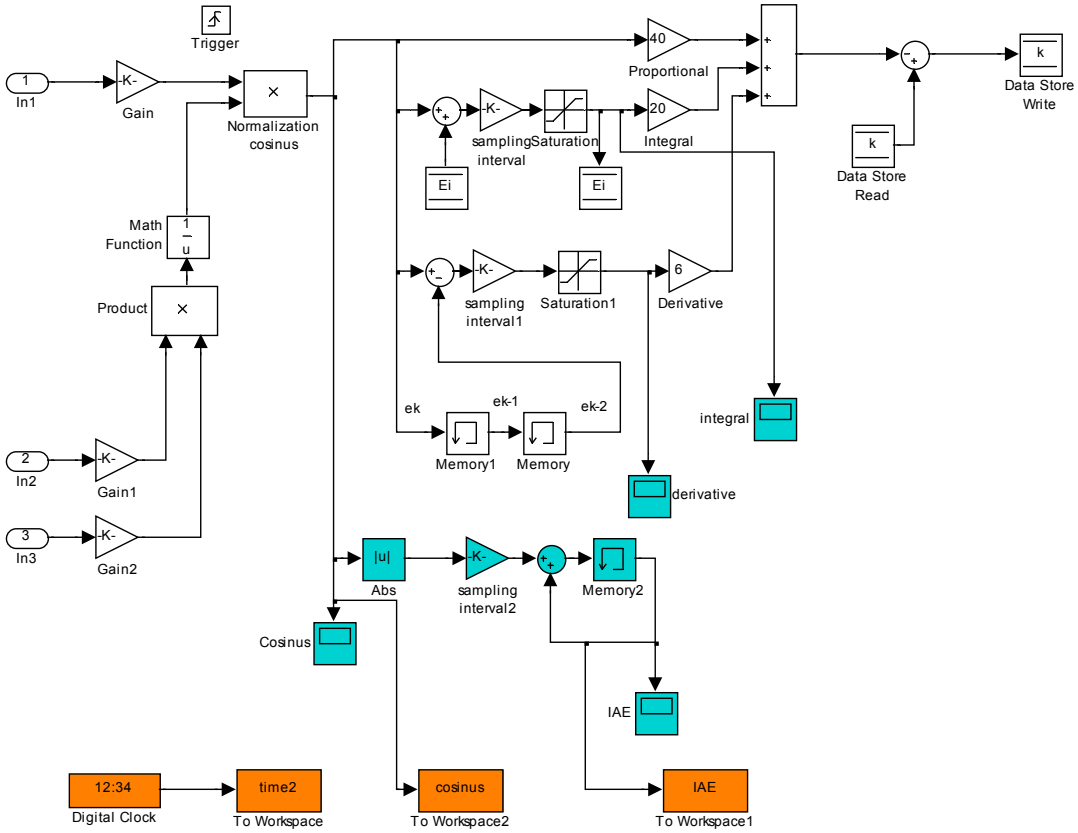

Figure 64 Simulink® control subsystem for the PID control

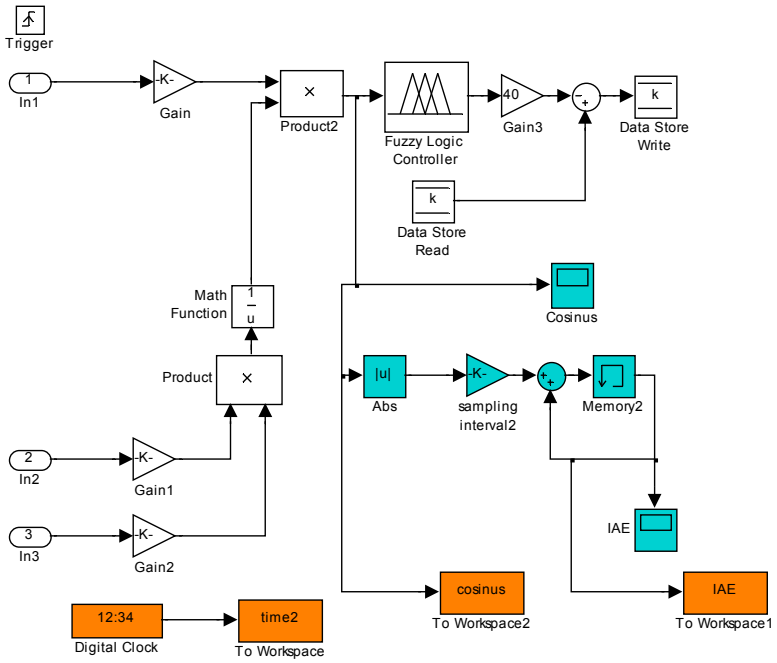

Figure 65 Simulink® control subsystem for fuzzy control

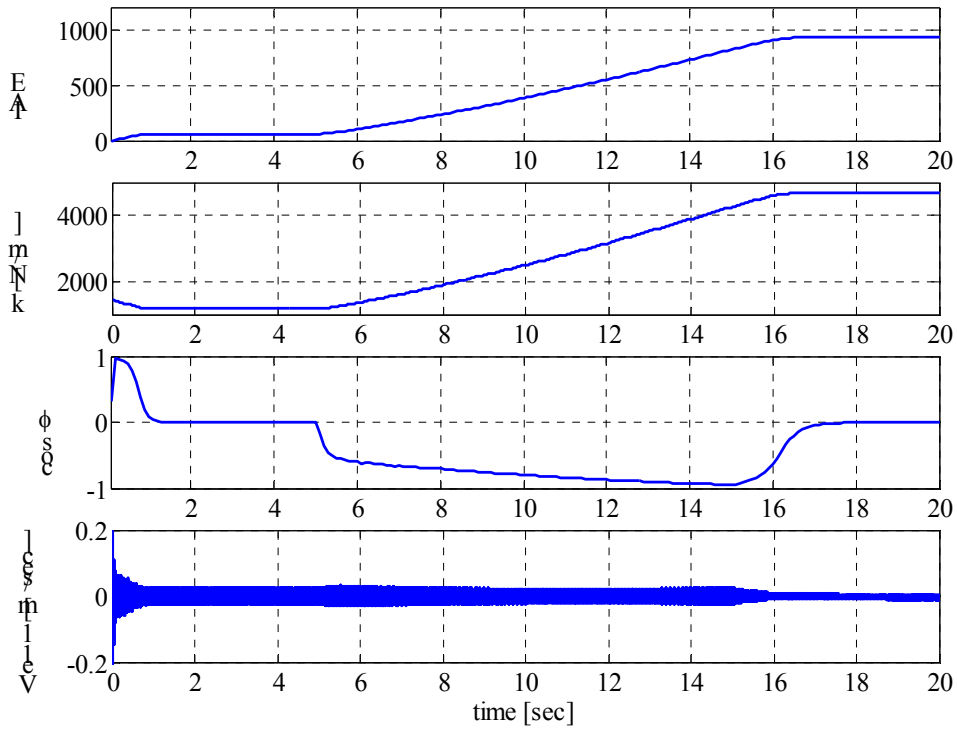

Figure 66 Control test results: proportional control with control constant *P*=40

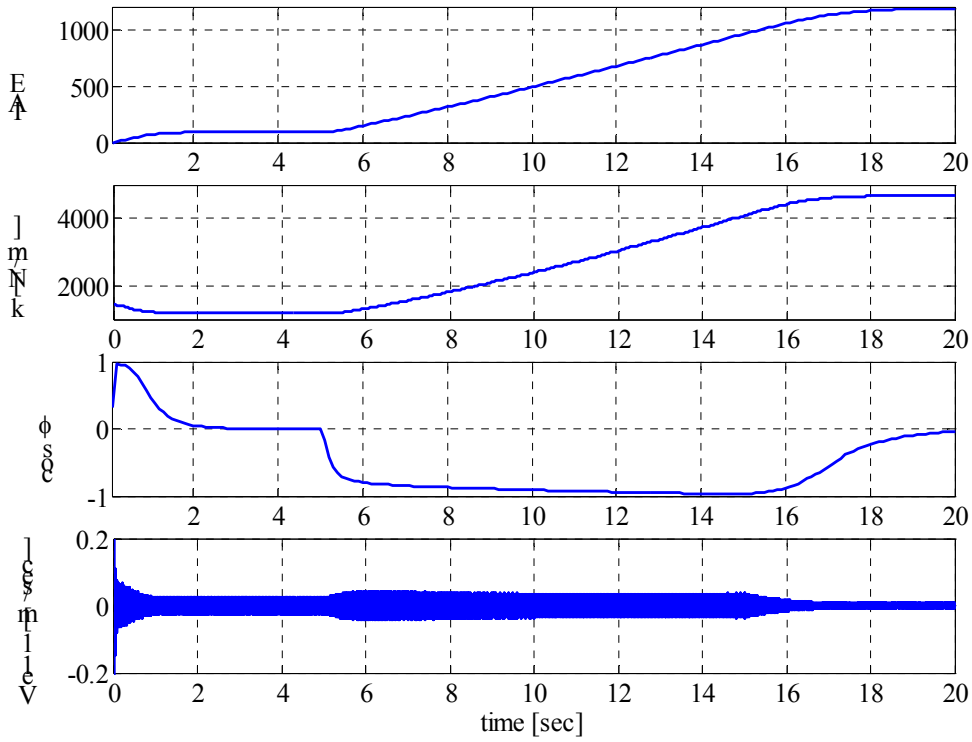

Figure 67 Control test results: polynomial control with control constant *P*=40/3

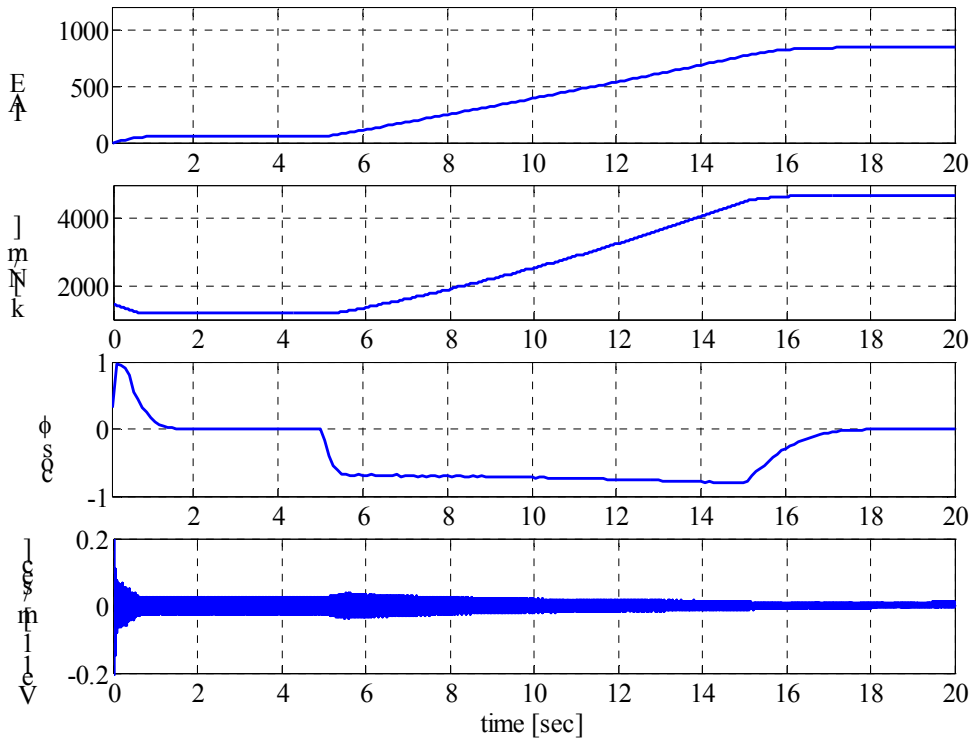

Figure 68 Control test results: fuzzy control with control constant *P*=40

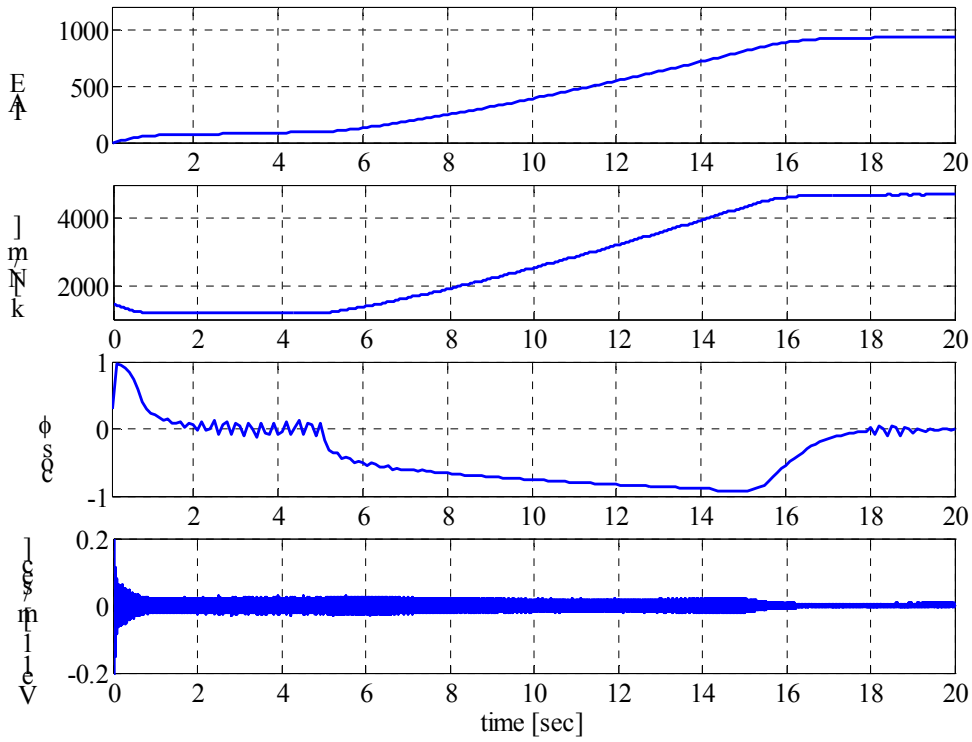

Figure 69 Control test results: PID control with control constants *P*=40, *I*=20 and *D*=8

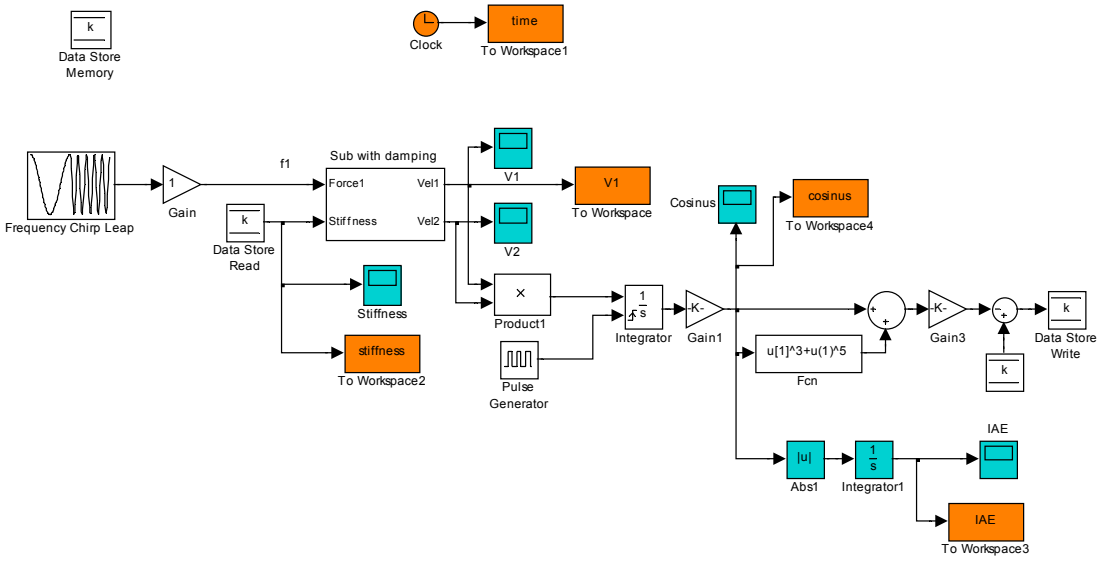

Figure 70 Simulink® system for the continuous updating polynomial control of a TVA

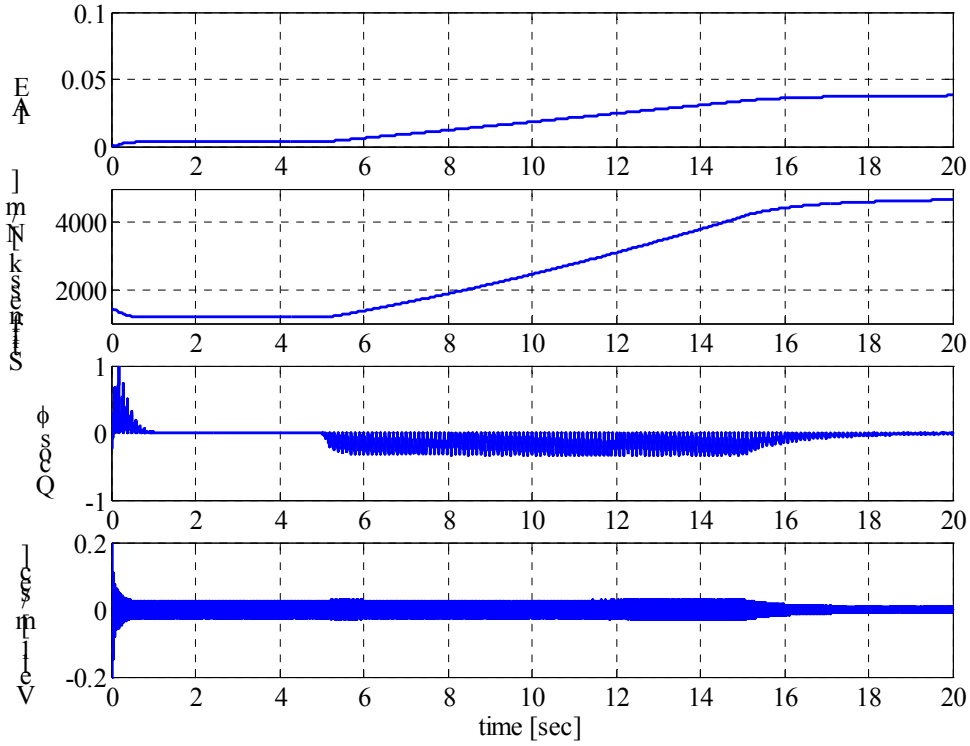

Figure 71 Continuous updating control test results: polynomial control; control constant *P*=40/3

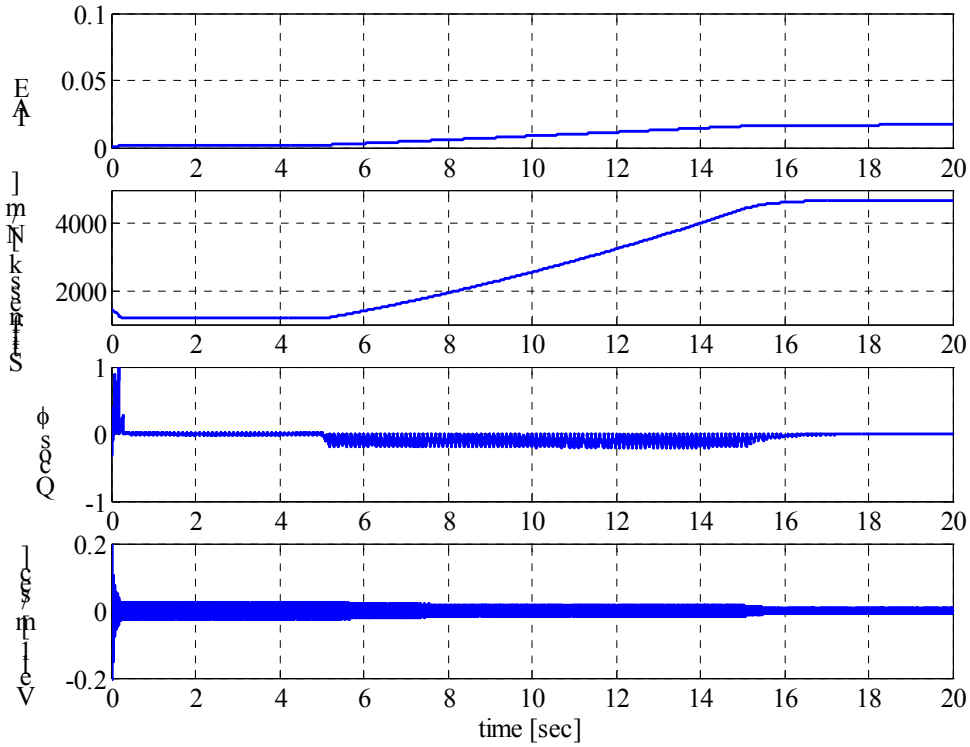

Figure 72 Continuous updating control test results: fuzzy control with control constant *P*=40

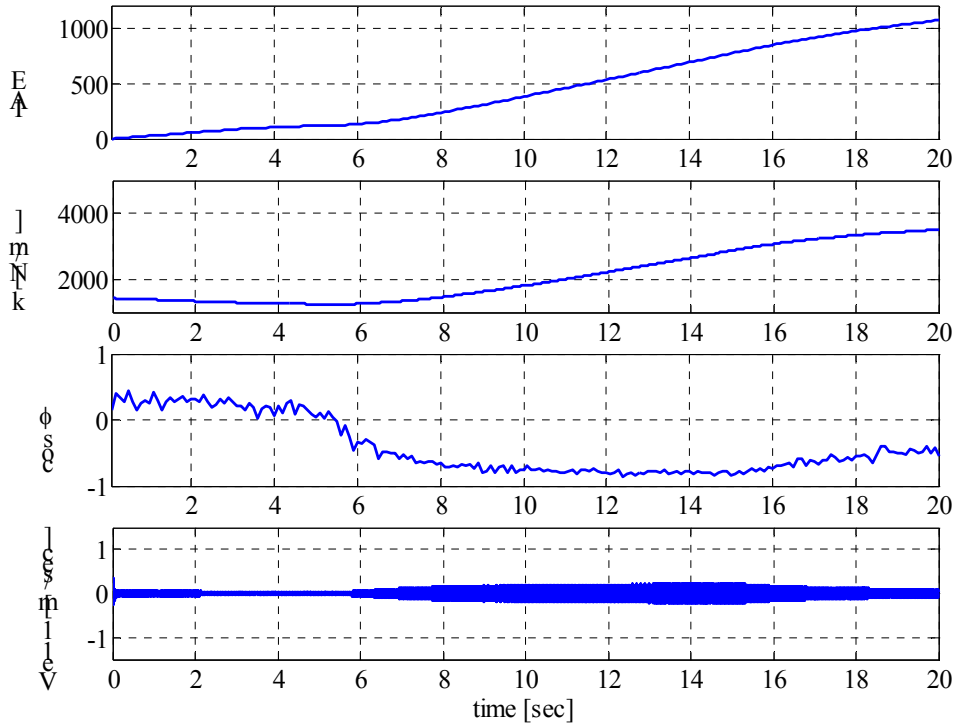

Figure 73 Noise control test results: polynomial control (*P*=40/3) with 20 dB signal to noise ratio

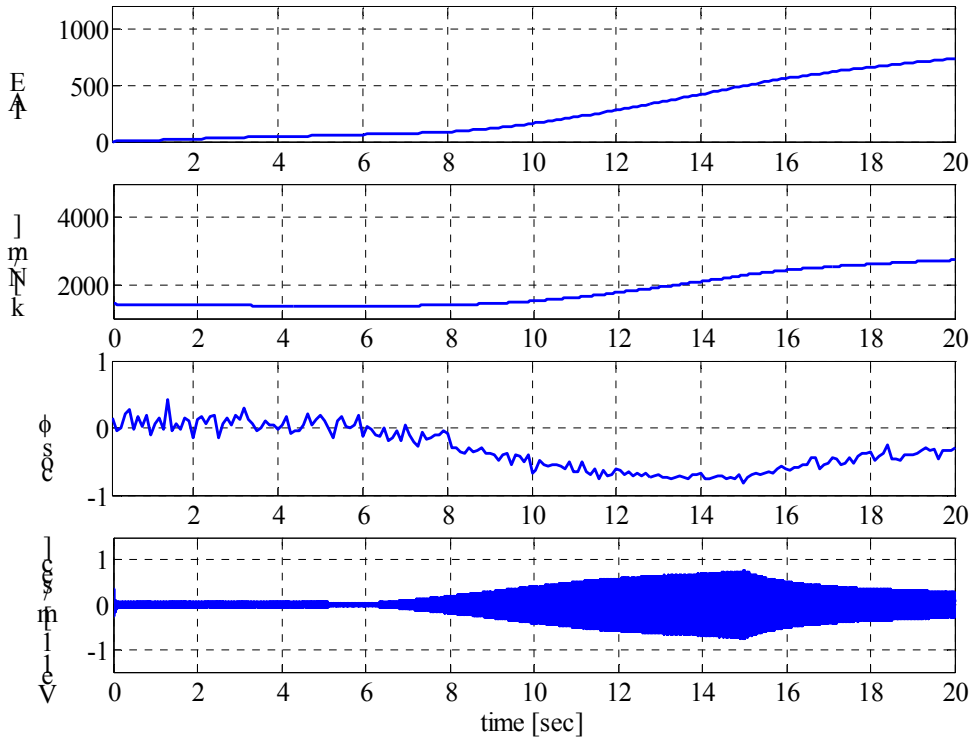

Figure 74 Noise control test results: polynomial control (*P*=40/3) with 10 dB signal to noise ratio

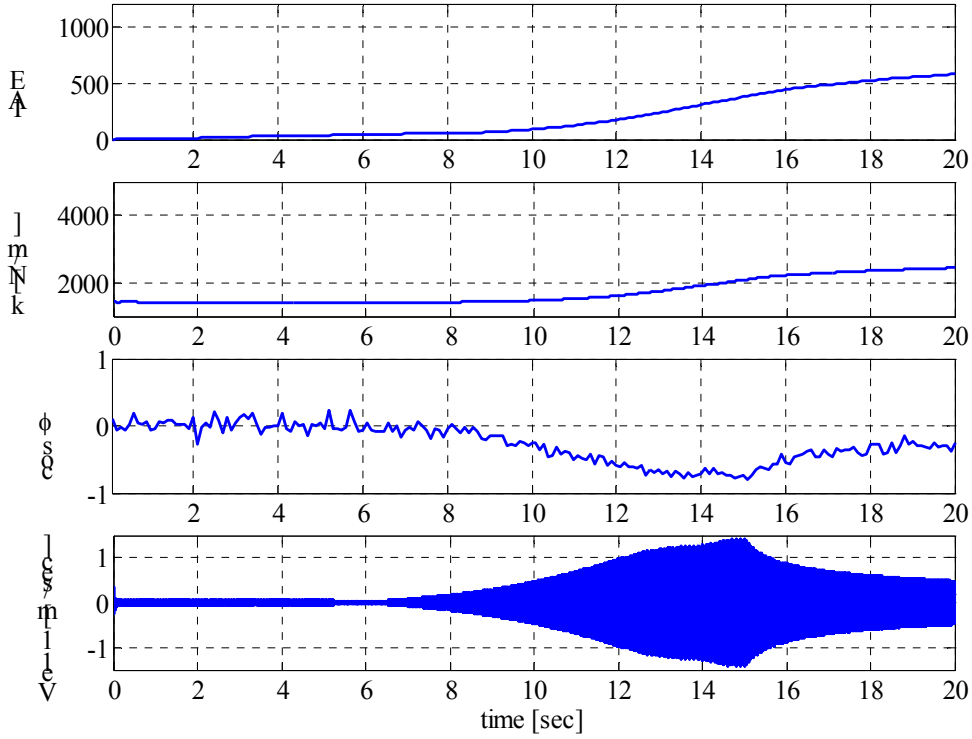

Figure 75 Noise control test results: polynomial control (*P*=40/3) with 5 dB signal to noise ratio

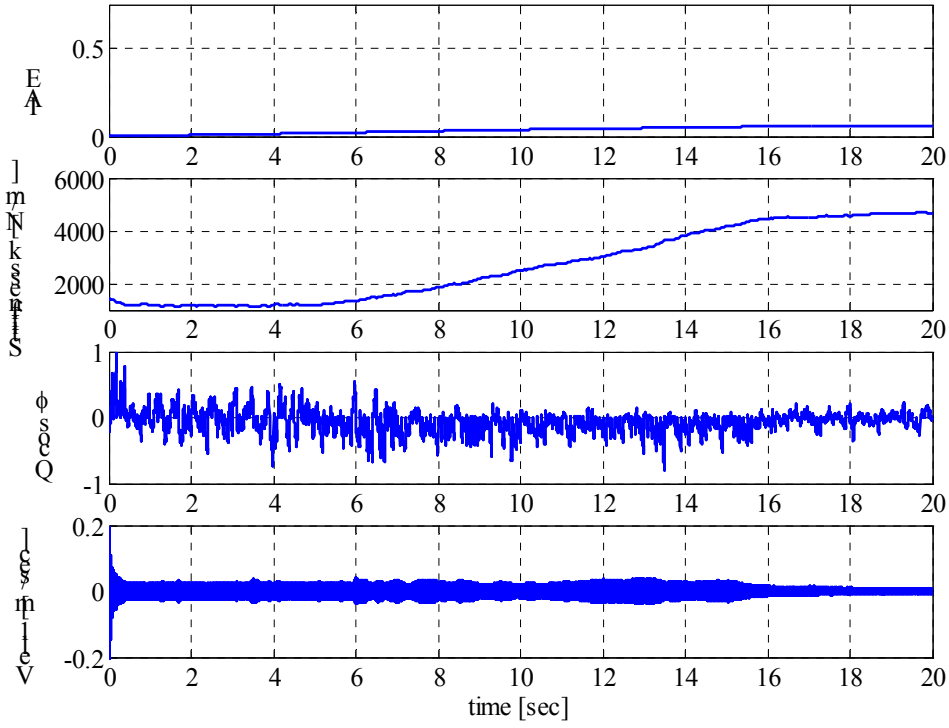

Figure 76 Noise control results: polynomial continuous control (*P*=40/3); 20 dB signal to noise ratio

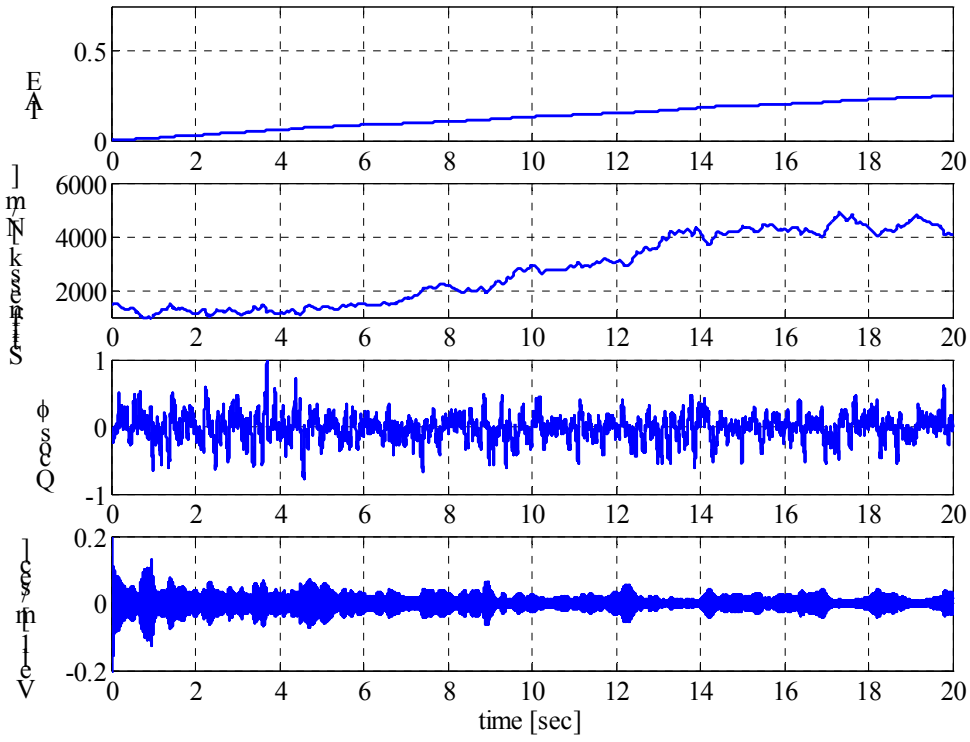

Figure 77 Noise control test results: polynomial continuous control (*P*=40/3); 10 dB signal to noise ratio

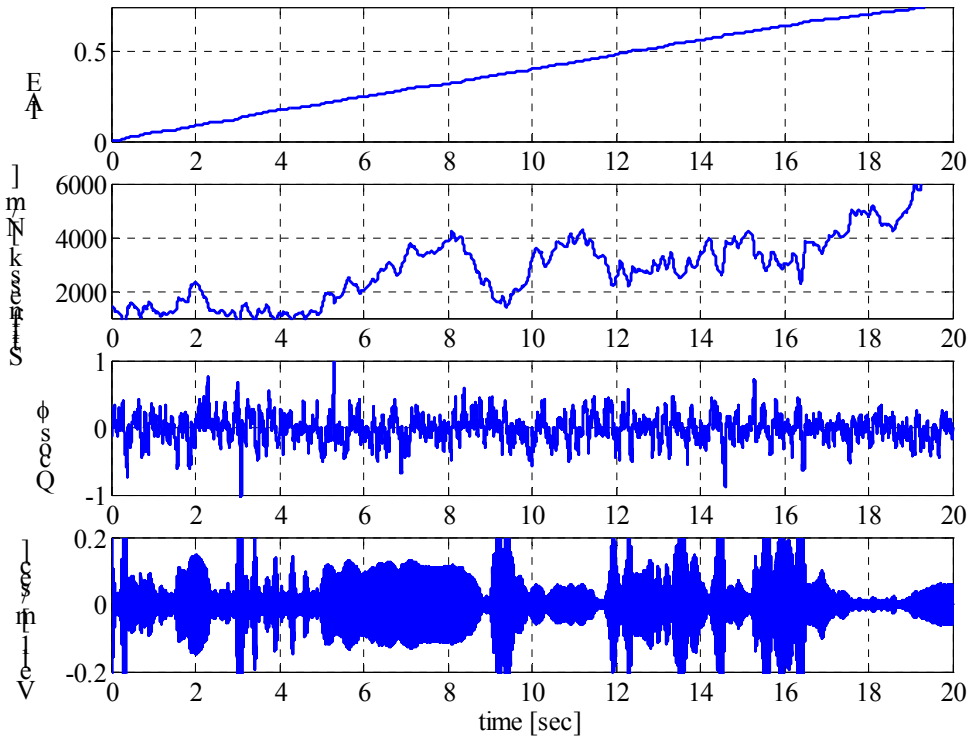

Figure 78 Noise control test results: polynomial continuous control (*P*=40/3); 5 dB signal to noise ratio

a)

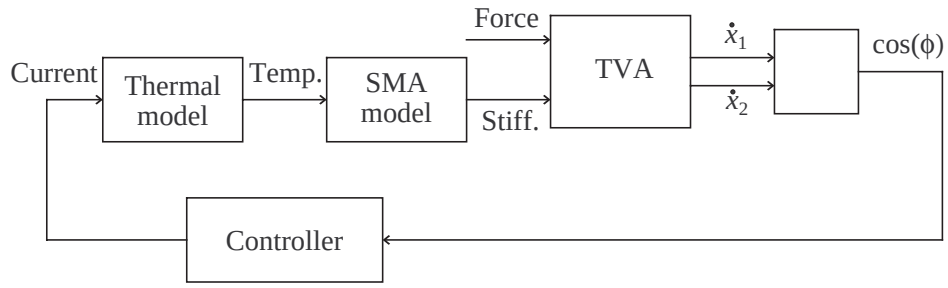

b)

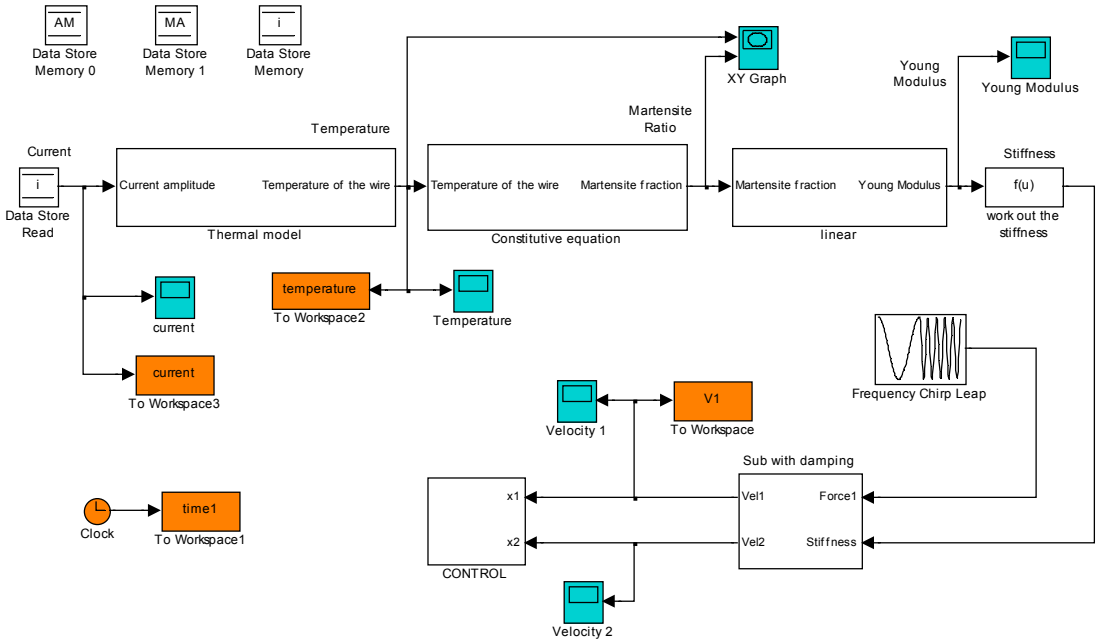

Figure 79 SMA TVA control: a) block diagram; b) Simlink® model

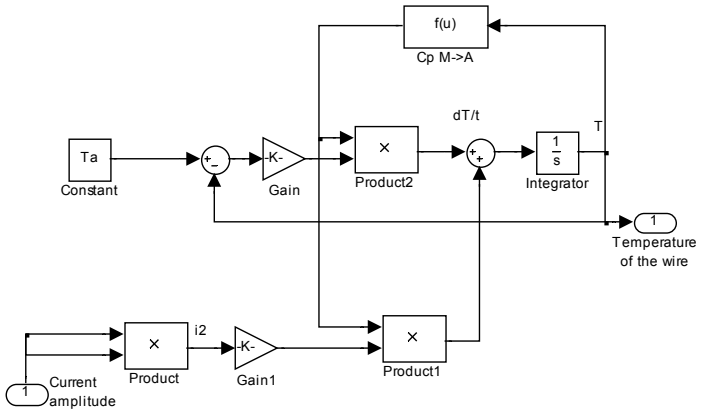

Figure 80 Thermal model subsystem

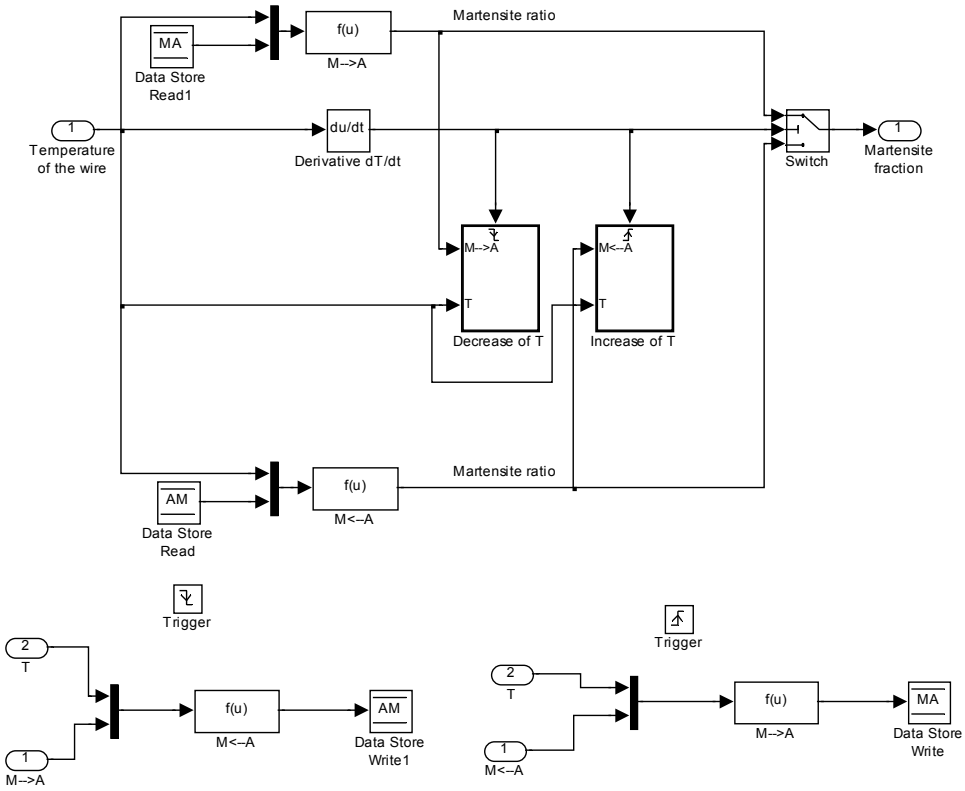

Figure 81 Constitutive subsystem

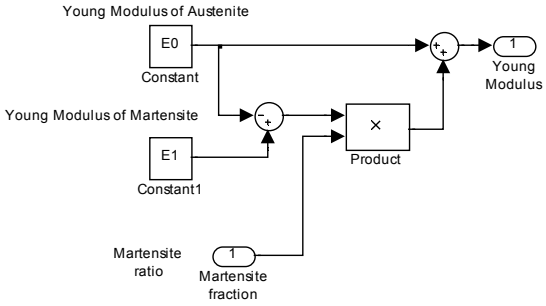

Figure 82 Young modulus evaluation subsystem

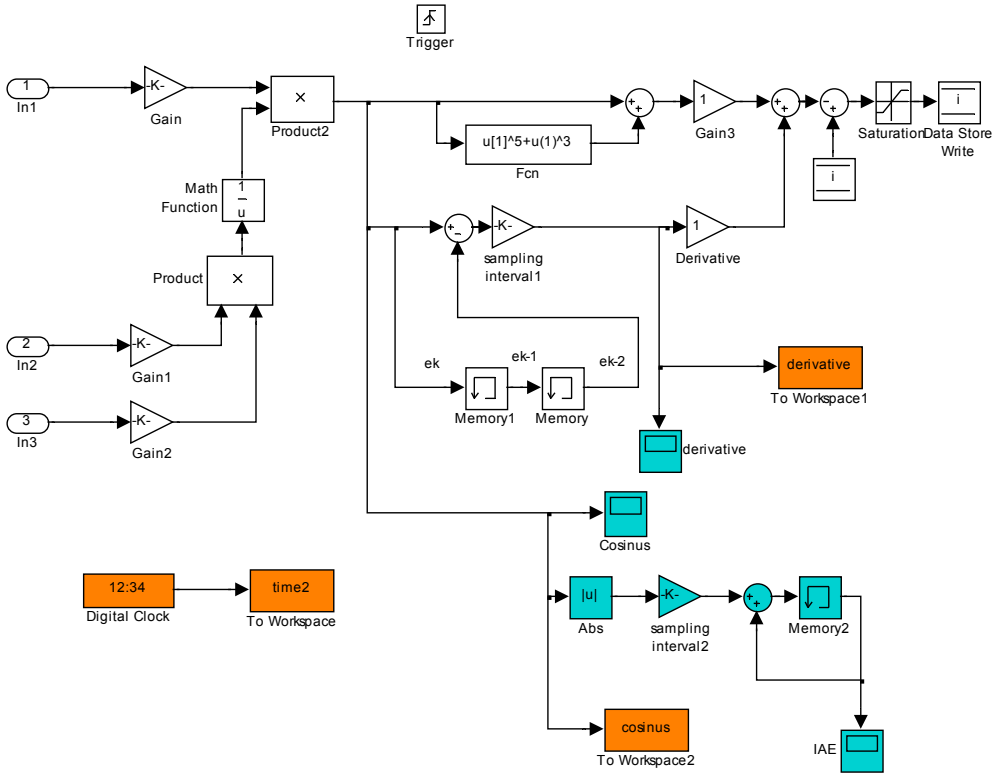

Figure 83 Simulink® subsystem for the PD control of SMA

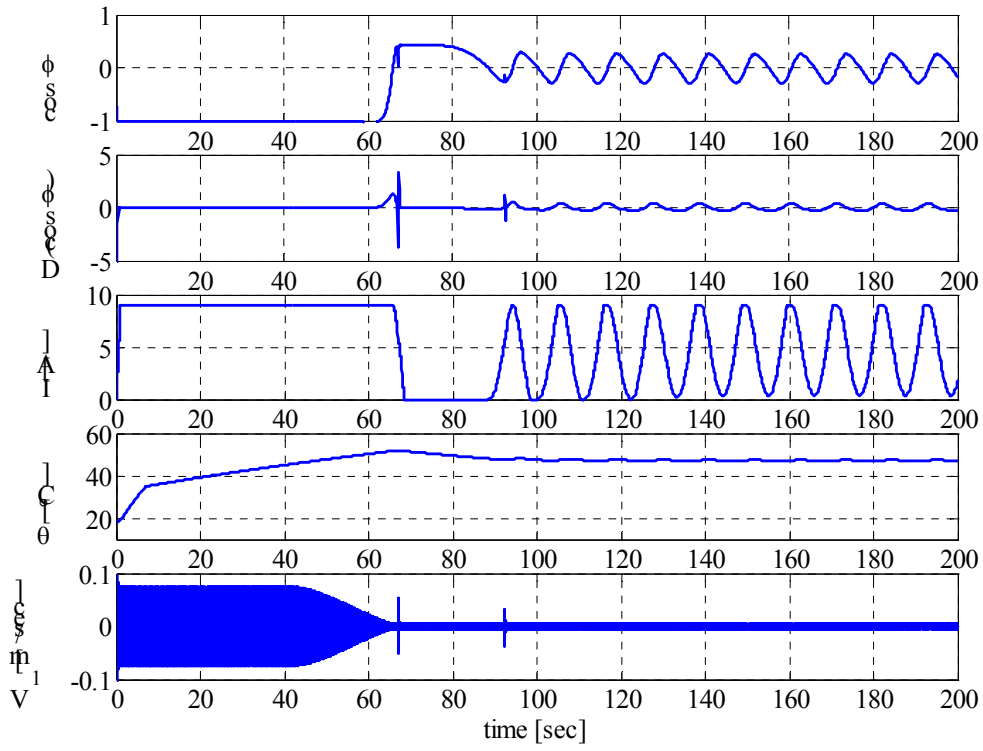

Figure 84 SMA control test: proportional control (*P*=1 and *D*=0); constant excitation at 90Hz

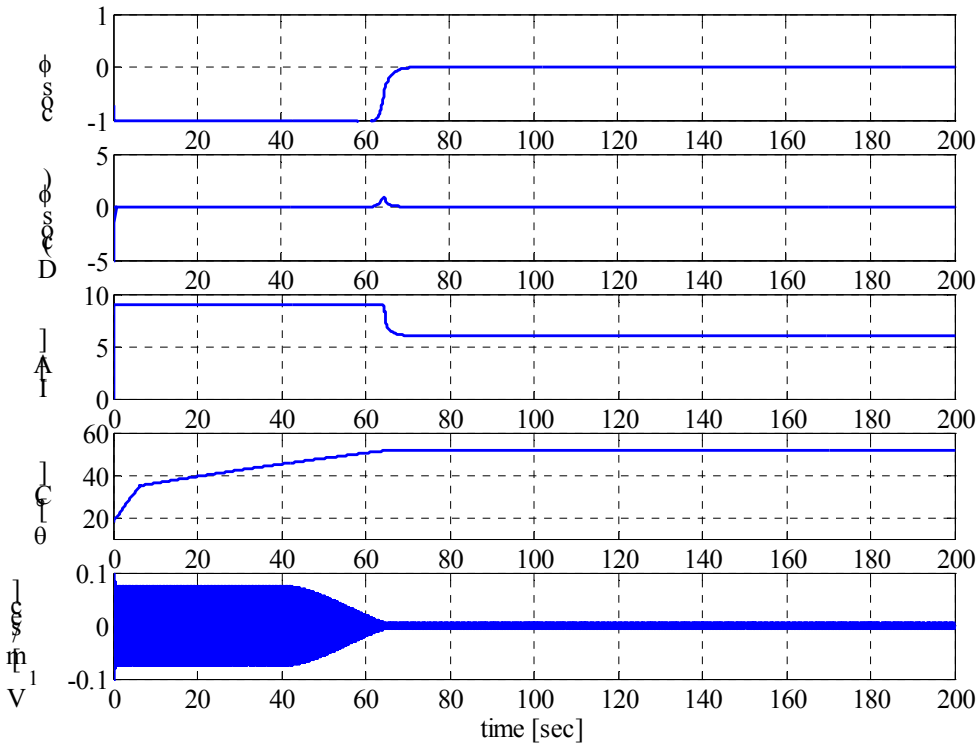

Figure 85 SMA control test: PD control (*P*=1 and *D*=1); constant excitation at 90Hz

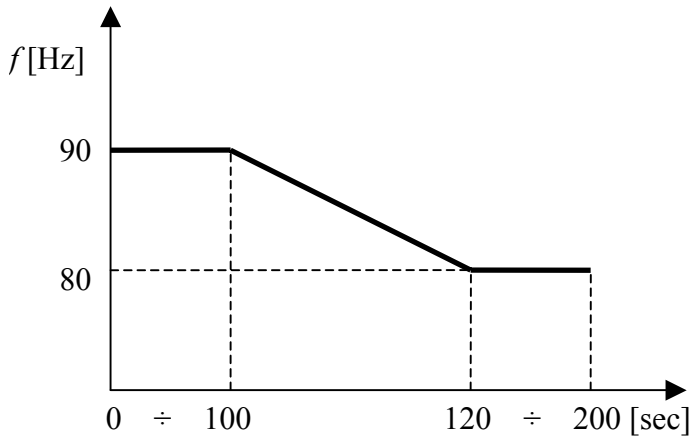

Figure 86 Frequency of the excitation force versus simulation time

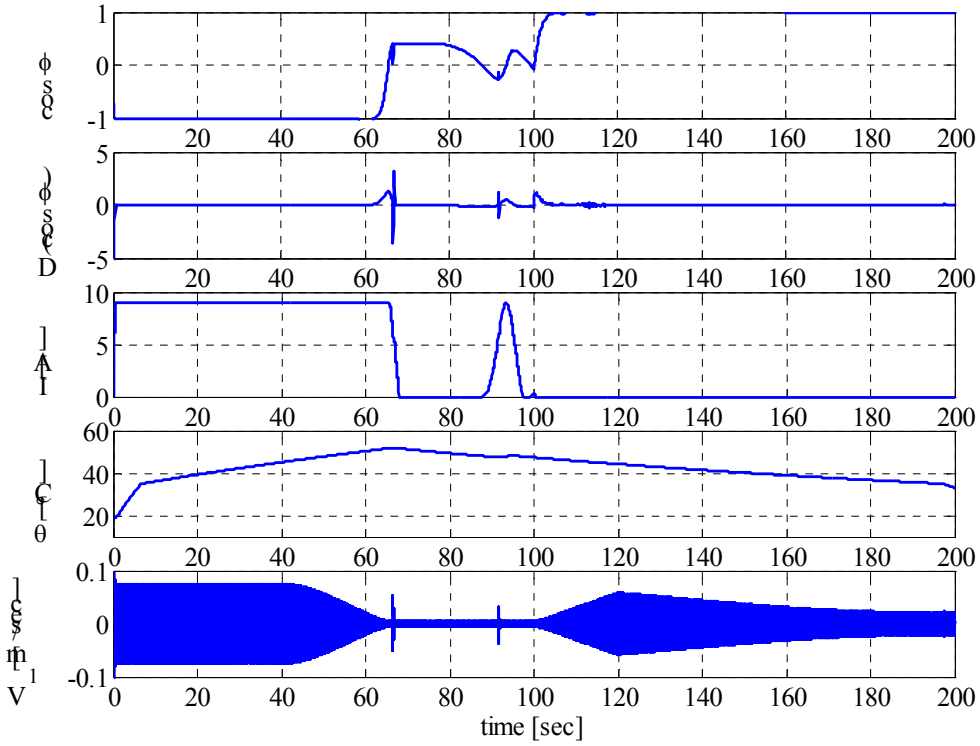

Figure 87 SMA control test: proportional control (*P*=1 and *D*=0); excitation frequency of Figure 86

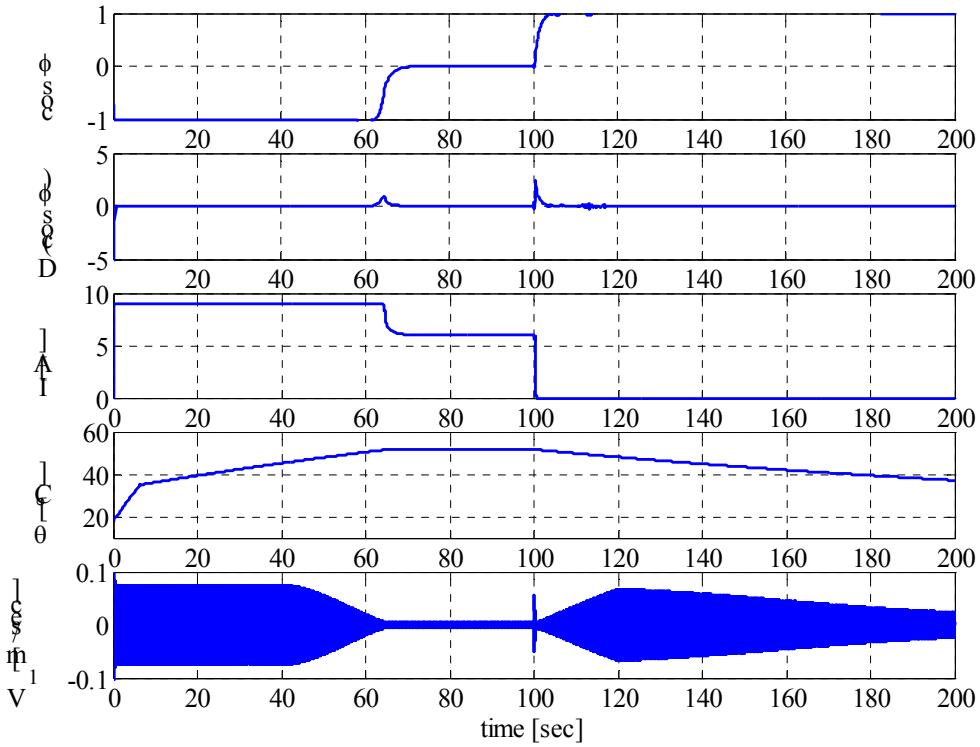

Figure 88 SMA control test: PD control (*P*=1 and *D*=1); excitation frequency of Figure 86

Tables

m_1	m_2	k	η	c_2	f_a	f_r
0.0036 kg	0.0053 kg	1422 N/m	0.0175	0.0481 kg/sec	82.3 Hz	129.5 Hz

Table 27 Settings of the Simulink® model of the TVA system

7. Conclusions and recommendations for future work

In this report the design and test of a SMA TVA has been described. Such a device was made by a simple beam like structure supported in the centre and made by a 2 mm SMA wire. Passing a current through the SMA wire a change in the temperature of the device can be attained. As the Young modulus of SMA varies with temperature, a change in the stiffness of the TVA can be obtained.

After an outline of the mathematical model developed for the design a SMA TVA was built and experimentally characterised. The results show the feasibility of using SMA properties to tune such a device. The device shows a variation of the tuning frequency of about 15%. The main limitations of the SMA absorber are the slow response time so that the complete transformation takes about 120 seconds using a 9A current to heat the SMA wire.

During the experimental tests a strange behaviour has been observed. During cooling of the wire, before reaching the martensitic steady state from the austenitic one, an extra softening of the material has been observed by an extra-reduction in the resonance frequency of the test rig.

Next, tuning of the absorber was considered. First a numerical analysis on an ideal TVA with real-time response showed the effectiveness and robustness of a simple non-linear adaptive system that consider only the phase between two signal collected from the TVA. Various control methods were considered and simulations performed. Then the numerical analysis of the SMA TVA showed the tuning capability of a PD semi-active control.

In future work any effort will be focused on the design of the controller. The empirical controller simulated in this report will be implemented in Real Time Workshop® and tested on the test-rig. Further mathematical analysis could also be carried out in order to apply some classical techniques of the non-linear control.

Appendices

A. Circle fitting - SDOF modal analysis

Part of the experimental analysis concerns identifying the modal properties of the absorber. Here, a single degree of freedom (sdof) approach is used to estimate natural frequency and damping factor, using the "circle fitting" approach. The circle fitting method is a simple and well-known approach to experimental modal analysis [12]. Here we recall the main principles of this methodology in order to shed light on the assumptions and simplifications made.

Firstly it is assumed that the system under test is a sdof. In the vicinity of a resonance the behaviour of most systems is dominated by a single mode. The sdof assumption is that for a small range of frequencies in the vicinity of the natural frequency of mode *r* the receptance α_{ij} (which is the ratio of the displacement of a system measured at the point *i* to the driving force applied on it at the point *j*) of the system is given by [12]

$$\alpha_{ij}(\omega)_{\omega\approx\omega_r} \cong \frac{{}_rA_{jk}}{\omega_r^2 - \omega^2 + i\eta_r\omega_r^2} + {}_rB_{jk} \tag{A1}$$

where the second term, which includes the influence of all the other modes, is approximately constant or independent of frequency ω. When plotted in the complex plane, the locus of the receptance traces out an arc of a circle as frequency increases, with the same properties as the modal circle for the specific mode in question but displaced from the origin of the Argand plane by an amount ${}_rB_{jk}$, determined by the contribution of all the other modes.

Assuming the system has constant structural damping the receptance form of FRF (frequency response function) is considered as it is this parameter that produces an exact circle in a polar plot for the properties of a simple oscillator. However, if it is required to use a model incorporating viscous damping then it is the mobility which should be used. Mobility is the ratio of the velocity of a system to the driving force applied on it.

In the case of a system assumed to have structural damping the receptance of mode *r* is proportional to [12]

$$\alpha_r(\omega) = \frac{1}{\omega_r^2\left[1 - \left(\frac{\omega}{\omega_r}\right)^2 + i\eta_r\right]} \tag{A2}$$

since the only effect of including the modal constant ${}_rA_{jk}$ is to scale the size of the circle and rotate it. Now it may be seen that for any frequency ω we may write the following relation [12]

$$\tan\left(\frac{\gamma}{2}\right)=\frac{1-\left(\omega/\omega_r\right)^2}{\eta_r} \tag{A3}$$

where γ is the angle measured at the circle centre (see Figure 89).

Considering two points a and b on the circle such that $\omega_a>\omega_b$ we can obtain an expression for the loss factor of the mode given by

$$\eta_r=\frac{\omega_a^2-\omega_b^2}{\omega_r^2\left[\tan\left(\gamma_a/2\right)+\tan\left(\gamma_b/2\right)\right]} \tag{A4}$$

If we are concerned with light damping ($\eta_r<0.3$) this can be accurately approximated as

$$\eta_r\cong\frac{2\cdot\left(\omega_a-\omega_b\right)}{\omega_r\left[\tan\left(\gamma_a/2\right)+\tan\left(\gamma_b/2\right)\right]} \tag{A5}$$

If we consider the half power points $\gamma_a=\gamma_b=\pi/2$ we obtain the formula

$$\eta_r=\frac{\omega_2^2-\omega_1^2}{2\omega_r^2}\cong\frac{\omega_2-\omega_1}{\omega_r} \tag{A6}$$

The diameter of the circle expressed by equation A2 is $1/\omega_r^2\eta_r$ and the principal diameter (the one passing through the natural frequency point) is parallel to the imaginary axis. When scaled by the modal constant ${}_rA_{jk}$ the diameter will be

$${}_rD_{jk}=\frac{\left|{}_rA_{jk}\right|}{\omega_r^2\eta_r} \tag{A7}$$

and the whole circle is tilted so that the principal diameter is oriented at an angle $\arg({}_rA_{jk})$ to the negative imaginary axis.

Having described the properties of the FRF circle, the analysis procedure is outlined. Basing the following comments on the case of structural damping, the sequence is:

(i) Select points to be used. The analyst must select some points near the identified maximum in the response modulus. The points chosen should not be influenced by the neighbouring modes and should encompass preferably 270° of the modal circle, although 180° is more usual. In any case not less than six points should be used.

(ii) Fit circle and calculate quality of fit. This step consists simply of finding a circle which gives a best fit in the least squares sense for the points included. At the end of this process, the centre and radius of the circle are estimated as well as a quality

factor (the mean square deviation of the chosen points from the circle). Errors of the order to 1-2% are commonplace.

The Matlab file `FitCircle.m` fits a circle to a set of complex valued data points. It is a least squares fit for the sum of $(d_i^2-R^2)^2$ (note that this is an approximation), where d_i is the distance from the i^{th} data point to the centre of the circle and R is the radius. The coordinates of the centre and the radius are

$$\begin{bmatrix} x_c \\ y_c \end{bmatrix} = \frac{1}{2}\begin{bmatrix} \mu_{x^2} - \mu_x^2 & \mu_{xy} - \mu_x\mu_y \\ \mu_{xy} - \mu_x\mu_y & \mu_{y^2} - \mu_y^2 \end{bmatrix}^{-1}\begin{bmatrix} \mu_{x^3} - \mu_x\mu_{x^2} + \mu_{xy^2} - \mu_x\mu_{y^2} \\ \mu_{x^2y} - \mu_y\mu_{x^2} + \mu_{y^3} - \mu_y\mu_{y^2} \end{bmatrix} \tag{A8}$$

$$R = \sqrt{\left|2\cdot\left(\mu_x x_c + \mu_y y_c\right) - \mu_{x^2} - \mu_{y^2} - x_c^2 - y_c^2\right|} \tag{A9}$$

where μ indicates the mean value.

A quality factor can be defined by

$$\sqrt{\frac{1}{n}\sum_{i=1}^{n}\left(\sqrt{\left(x_i - x_c\right)^2 + \left(y_i - y_c\right)^2} - R\right)^2} \tag{A10}$$

and indicates the root mean square error.

(iii) Locate natural frequency. The natural frequency is located at the frequency where $\mathrm{d}\omega/\mathrm{d}\gamma$ reaches a maximum. Such a procedure has a precision of about 10% of the frequency increments between points.

(iv) Calculate multiple damping estimates and scatter. We can use equation A4 to calculate damping estimates using every possible combination of one point below the resonance with one above resonance. Then we can compute the mean value and the deviation. If the deviation is less than 4-5%, then we have succeeded in making a good analysis. If the scatter is too high we can examine the damping estimates trend (damping carpet plot [12]). If it is random then the scatter is probably due to measurement errors but if it is systematic then it could be caused by various effects such as poor experimental set-up, interference from neighbouring modes, non linear behaviour, etc.

(v) Determine modal constant modulus and argument ($_rA_{jk}$). These can be obtained from the diameter of the circle and from its orientation relative to the real and imaginary axis.

(vi) Construct the theoretically regenerated FRF plot. We can use equation A1 where $_rB_{jk}$ is obtained by measuring the distance from the top of the principal diameter to the origin.

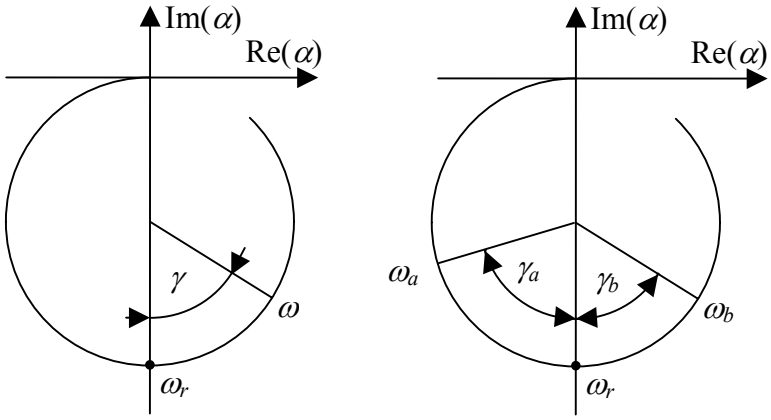

Figure 89 Properties of modal circle

References

1. Brennan, M.J., *Vibration control using a tunable vibration neutralizer.* Proceedings of the Institution of Mechanical Engineers, Journal of Mechanical Engineering Science, 1997. **211**(C): p. 91-108.
2. Long, T., M.J. Brennan, and S.J. Elliott, *Design of smart machinery installations to reduce transmitted vibrations by adaptive modification of internal forces.* Proceedings of the Institution of Mechanical Engineers, Journal of Mechanical Engineering Science, 1998. **212**(I): p. 215-228.
3. Brennan, M.J. *Actuators for active vibration control - Tunable resonant devices*. in *Proceedings of the 4th European Conference on Smart Materials and Structures*. 1998. Harrogate, U.K.
4. Franchek, M.A., M.W. Ryan, and R.J. Bernhard, *Adaptive passive vibration control.* Journal of Sound and Vibration, 1995. **189**(5): p. 565-585.
5. Smith, K.E. *Smart tuned mass dampers*. in *Active Materials and Adaptive Structures: Proceedings of the ADPA/AIAA/ASME/SPIE Conference*. 1991. Alexandria, Virginia.
6. Kidner, M.R.F. and M.J. Brennan, *Improving the performance of a vibration neutralizer by actively removing damping.* Journal of Sound and Vibration, 1999. **221**(4): p. 587-606.
7. Kidner, M.R.F. and M.J. Brennan, *Real-time control of both stiffness and damping in an active vibration neutralizer.* Smart Material and Structures, 2001. **10**: p. 758-769.
8. Kidner, M.R.F. and M.J. Brennan, *Varying the stiffness of a beam-like neutralizer under fuzzy logic control.* Transaction of the ASME, Journal of Vibration and Acoustics, 2002. **124**: p. 90-99.
9. Williams, K.A., G. Chiu, and R. Bernhard, *Adaptive-passive absorber using shape-memory alloys.* Journal of Sound and Vibration, 2002. **249**(5): p. 835-848.
10. Srinivasan, A.V. and D.M. McFarland, *Smart Structures, Analysis and Design*. 2001: Cambridge University Press.
11. Giurgiutiu, V., *Actuators and smart structures*, in *Encyclopedia of Vibration*, S.G. Braun, D.J. Ewins, and S. Rao, Editors. 2001, Academic Press.

12. Ewins, D.J., *Modal testing: theory, practice and application*. 2nd ed. 2000: Research Studies Press Ltd.
13. Hixson, E.L., *Mechanical impedance*, in *Shock and vibration handbook*, C.M. Harris, Editor. Third ed. 1987, McGraw Hill.
14. Hodgson, D.E., M.H. Wu, and R.J. Biermann, *Shape Memory Alloys*. Tenth ed. Metals Handbook. Vol. 2: available also online: http://www.sma-inc.com/SMAPaper.html.
15. Leppäniemi, A., *Shape memory alloys - applications and commercial aspects*. 2000, Tampere University of Technology, Institute of Automation and Control: http://www.ad.tut.fi/aci/courses/76527/Seminars2000/SMA.pdf.
16. Liang, C. and C.A. Rogers, *One dimensional thermomechanical constitutive relations for shape memory materials.* Journal of Intelligent Material Systems and Structures, 1997. **8**: p. 285-302.
17. Liang, C. and C.A. Rogers, *Design of Shape memory alloy springs with applications in vibration control.* Journal of Intelligent Material Systems and Structures, 1997. **8**: p. 314-322.
18. Liang, C. and C.A. Rogers, *Design of Shape memory alloy actuators.* Transaction of the ASME Journal of Mechanical Design, 1992. **114**: p. 223-230.
19. Baz, A., K. Imam, and J. McCoy, *Active vibration control of flexible beams using shape memory actuators.* Journal of Sound and Vibration, 1990. **140**(3): p. 437-456.
20. Brailovski, V., F. Trochu, and A. Leboeuf. *Design of shape memory linear actuators*. in *SMST-97*. 1997. Asilomar, California, USA.
21. *Selected properties of NiTi*, in NiTi Smart Sheet^{SM}. 2002. http://www.sma-inc.com/NiTiProperties.html from Shape Memory Applications, Inc. site.
22. Liang, C. and C.A. Rogers, *Behavior of shape memory alloy reinforced composite plates part I: model formulations and control concepts.* American Institute of Aeronautics and Astronautics, 1989. **89-1389-CP**.
23. Liang, C. and C.A. Rogers, *Behavior of shape memory alloy reinforced composite plates part II: results.* American Institute of Aeronautics and Astronautics, 1989. **89-1331-CP**.
24. Choi, S.B. and J.H. Hwang, *Structural vibration control using shape memory actuators.* Journal of Sound and Vibration, 2000. **231**(4): p. 1168-1174.

25. Song, G., *Robust position regulation of a shape memory alloy wire actuator*. Proceedings of the Institution of Mechanical Engineers, Journal of Mechanical Engineering Science, 2002. **216**(I): p. 301-308.

26. Yang, K. and L.C. Gu, *A novel robot hand with embedded shape memory alloy actuators.* Proceedings of the Institution of Mechanical Engineers, Journal of Mechanical Engineering Science, 2002. **216**(C): p. 737-745.

27. *Measuring Transformation Temperatures in NiTi Alloys*, in NiTi Smart Sheet^{SM}. 2002. http://www.sma-inc.com/ttrmeas.html from Shape Memory Applications, Inc. site.

28. *Nitinol SM495 Wire*, in Material data sheet. 2002. www.nitinol.com from Nitinol Devices & Components site.